UNIVERSITY OF SOUTHAMPTON

ABSTRACT

FACULTY OF NATURAL AND ENVIRONMENTAL SCIENCES

SCHOOL OF CHEMISTRY

Master of Philosophy

Synthesis of transition metal nitrides and silicon based ternary nitrides

by

Syed Imran Ullah Shah

Solution phase ammonolysis and sol-gel techniques that produce polymeric metal-amide precursors are of growing interest in the synthesis of nitride materials, which result from the thermal decomposition of the polymer. They can be used to control composition and to produce a large number of useful morphologies such as nanoparticles, films, monoliths, aerogels, and materials with large surface area such as foams. The synthesis of nitride materials using ammonolysis of metal amides and chlorides has so far largely focused on producing powders for applications such as catalysis, or thin films by chemical vapour deposition and related techniques.

In this thesis, formation of tantalum and molybdenum nitride nanoparticles and metal-silicon nitride based nanocomposites have been synthesised using non-oxide precursors by solution phase ammonolysis and sol-gel methods respectively. For tantalum nitride nanoparticles $Ta(NMe_2)_5$ in THF was ammonolysed with ammonia at -78 °C and the polymeric precursor was pyrolysed at various temperatures under ammonia. Amorphous TaN was obtained at 700 °C and below, while Ta_3N_5 was obtained at 800 °C under ammonia and also by re-annealing the amorphous samples at 800 °C under nitrogen. Molybdenum nitride powders were obtained by solution phase ammonolysis of $MoCl_5$ or $Mo(NMe_2)_4$ and further annealing the polymeric precursors on different temperatures. The chloride precursor resulted in hexagonal MoN_x at 500 °C, or rock salt MoN_x at 700-1000 °C and mixture of both at 600 °C. The amide precursor resulted phase pure hexagonal MoN_x at 600 °C and rock salt mixed with hexagonal at 1000 °C. Samples produced at 600 °C consisted mainly of nanotubes.

Some decomposition to molybdenum metal was found in MoN obtained at 1000 °C from either precursor source.

Co-ammonolysis of $Ta(NMe_2)_5$ or $Mo(NMe_2)_4$ with $Si(NHMe)_4$ was carried out using sol-gel technique. Polymeric metal-silicon amide precursors were annealed at 600 or 1000 °C. The Ta/Si precursor produced amorphous nanocomposites and no phase segregation was observed even after high temperature annealing. With molybdenum the products were nanocomposites of molybdenum nitride particles, including nanotubes, supported on a silicon nitride amorphous matrix.

Contents

Chapter 1 – Introduction

Chapter 2 – Instrumental Techniques

Chapter 3 – Tantalum nitrides from ammonolysis of Ta(NMe$_2$)$_5$

Chapter 4 – Molybdenum nitrides from ammonolysis of MoCl$_5$

Chapter 5 – Molybdenum nitrides from ammonolysis of $Mo(NMe_2)_4$

Chapter 6 – Metal containing silicon nitrides

Chapter 7 – Conclusions

Acknowledgments

Firstly, I would like to thank my supervisor, Dr. Andrew L. Hector and my advisor Professor Dr. Bill Lavason for all their advise and patience during my M.Phil. Special thanks to Hector, who was constant source of warmth, knowledge and friendship.

I thank Pietro Chirico, whose help in the lab during the initial stages of my degree is really appreciated. I also thank Ben Grey, who is always ready to provide any kind of help in a very friendly manner. I would like to say thanks to Dr. Peter Wells for his suggestions to improve the EXAFS fits, Dr. Anton page for TEM tranining, and all of my colleagues who have been working in the Lab 2009 for making such a nice working environment. Next many thanks to all those people who helped me in different ways in accomplishing my degree.

I would like to take this opportunity to say special thanks to my Father, Mr. Syed Lal Badshah who's prayers are always there for every success in my life, and to my sweet Mom, for her loving wishes, and prayers for me. Finally I would like to thank my whole family for their loving wishes.

Abbreviations

TMN	Transition Metal Nitrides
TGA	Thermogravimeteric Analysis
PXD	Powder X-ray Diffraction
IR	Infrared
UV-vis	Ultraviolet Visible
NMR	Nuclear Magnetic Resonance
EM	Electron Microscopy
SEM	Scanning Electron Microscopy
TEM	Transmission Electron Microscopy
EDX	Energy Dispersive X-ray
EXAFS	Extended X-ray Absorption Fine Structure spectroscopy
XANES	X-ray Absorption Near Edge Spectroscopy
CVD	Chemical Vapour Deposition
ALD	Atomic Layer Deposition
THF	Tetrahydrofuran

1. Introduction

Transition metal nitrides (TMNs) and carbides have wide applications in many industrial sectors. TMNs such as TiN, NbN, HfN, and TaN serve as highly corrosion-resistant materials, barrier layers for the semiconductor industry, good electrical conductors and low temperature superconductors as well as hard coatings.[1, 2] Some early transition metal nitrides behave like noble metals (Pt, Pd, Rh and Ru) in the catalysis of some chemical and electrochemical reactions, including oxidation of hydrogen, CO, alcohols and reduction of oxygen.[3] Some of the metal nitrides have also shown hydrogen gas storage capabilities e.g. Li_3N based compostions.[4]

There are numerous reviews on the chemistry of nitride materials including those focused on structure,[5, 6] catalysis,[7] high pressure phases,[8] hard materials,[9] phosphors,[10] s-block nitrides[11] and silicon nitride ceramics.[12]

Application of nitride materials in electronics, opto-electronics, wear resistant coatings, sensors and high temperature ceramics are facilitated by synthesis methods that yield the material in the appropriate form. As a general rule nitrides sinter less readily than oxides due to their high lattice energies, hence nitrides with small particle sizes have long been studied. There is an increasing interest in the size and shape dependent properties of these materials to understand existing properties and develop new ones, e.g. for semiconductors such as GaN, catalytically active compositions like Co_3Mo_3N and hard materials such as TiN.[13]

In this chapter some of the important applications and the synthesis routes for nanocrystalline transition metal nitrides will be discussed.

1.1 Applications

1.1.2 Catalysis

The interest in binary or ternary metal nitrides as catalysts is due to the similarity in activity of the transition metal nitrides to noble metals[14, 15] and their high surface areas which typically have been obtained through ammonolysis of metal oxides by temperature programmed reaction[16-19] and in some cases have higher activity than commercial catalysts.[20] The morphology of the nanocrystalline material could be varied by changing the flow rate and the heating and the cooling rates.[21] In catalysis, porous nitrides not only offer a large accessible surface area with minimum mass transfer issues, but could provide size and shape selectively.[22] The introduction of nitrogen atoms into the early transition metal leads to the increase of the d electron density of the metal at the Fermi level and induces noble metal like properties to the nitrides.[23, 24] Furthermore during the passivation step following nitride preparation and before exposure to air, oxygen is incorporated into the lattice and as a result an acidic nature can appear.[21] Catalytic studies of nitrides obtained through precursor decomposition are few.[25, 26]

Catalysis with metal nitrides has mainly centred around the transition metal nitrides with special emphasis on groups 5 and 6. These nitrides have been particularly successful with reactions in a hydrogen environment like hydrogenation, de-hydrogenation, hydrodenitrogenation, hydrodesulphurisation, hydrogenolysis, ammonia synthesis, amination, hydride activation and also in photocatalysis.[27]

Transition metal nitrides W_2N, Mo_2N, and VN, along with vanadium oxynitride, have been found to be active catalysts for ammonia synthesis.[28-30] N_2 and H_2 are activated on the surface of the nitrides, followed by ammonia synthesis and desorption of NH_3 gas. The phase of the nitrides as well as the acid/base nature of the nitrides becomes important to have facile activation and desorption steps. A ternary nitride Co_3Mo_3N doped with Cs has proven to be more efficient than the commercial Fe/K_2O catalyst in NH_3 synthesis. The effect of doping has not been particularly dependent on the amount of loading and Cs doping on Mo_2N has not been effective.[31] NH_3 synthesis via hydrazine decomposition on Al_2O_3 supported molybdenum nitride shows activities comparable to the traditional Ir/Al_2O_3 catalyst.[32] The catalytic properties of nanocrystalline TiN in hydrogen transfer reactions with complex hydrides like $NaAlH_4$ has also been reported.[33] The reaction between diphenylethyne (DPE) and $NaAlH_4$ is faster in the presence of TiN and decomposes the analate to AlH_3 and NaH. The AlH_3 then reduces the DPE to stilbine forming an unknown intermediate, which then is further reduced in H_2 to reproduce the alanate.

1.1.2.1 Photcatalysis

The photocatalytic properties of nanocrystalline Ta_3N_5 have been recently reported. Because of its absorption in the visible region of the solar spectrum, it is potentially more efficient than the more traditional TiO_2 or oxynitrides based on TiO_2. Zhang and Gao[34] studied the photocatalytic properties of $TiO_{2-x}N_x$ in comparison to Ta_3N_5 of different crystallite sizes in the decomposition of methylene blue and observed that the nanoparticles of Ta_3N_5 showed better activity than large particles and exhibited a much higher photocatalytic activity than $TiO_{2-x}N_x$ of the same size. Yang and co-workers[35] recently reported on the increased efficiency of CNT/Ta_3N_5 monocomposites in photocatalysis compared with Ta_3N_5 nanoparticles. Ta_2O_5 was impregnated into the CNT's and was nitrided in NH_3 to form the composites. The better activity of the nanocomposites may be due to the high conductivity of the nanotubes, which helps in scavenging the photogenerated electrons.

1.1.3 Supercapacitors

Electrochemical capacitors are known as supercapacitors because of their higher power and energy density (20-200 times greater specific capacitance) compared with conventional capacitors.[36] Transition metal nitrides like VN,[37] TiN,[38] WN[39] and MoN_x[40] have been found to be potential replacements for RuO_2 as supercapacitor electrode materials because of their high conductivity, low cost and high chemical resistance. Further, careful surface oxidation would expose the different oxidation states of the metal for Faradaic reactions leaving the conducting properties of the nitrides under the surface intact.[38, 41, 42] A mixture of γ-Mo_2N and Co_3Mo_3N of different Co/(Co+Mo) molar ratios has been synthesised by the reaction between cobalt (III) nitrate and ammonium heptamolybdate. The specific capacitance increased from 30 Fg^{-1} to 109 Fg^{-1} when the Co/(Co+Mo) ratio was increased from 0 to 0.25 after which the capacitance decreased. The voltage stability window at 0.8 V remained the same as pure nitride, but the kinetics of the redox process became faster with a corresponding increase in the current.

1.1.4 Ultrahard materials

Coatings of high hardness and low coefficient of friction are in demand for applications under severe conditions like high vacuum, high temperature, high loads and low temperatures. Diamond, with hardness of 70-100 GPa, has been used for such coatings. But diamond is expensive, is difficult to form as thin smooth coatings, and alloys with carbide-forming metals like iron and steel at high temperature. Nitrides like c-BN, TiAlN, TiZrN or TiCN are good hard coating materials with hardness in the range of 20-30 GPa, which could further be improved by varying structure and composition of the film.[43-48]

Patscheider[46] examined the hardness of $TiN:Si_3N_4$ nanocomposites. In the absence of silicon nitride, the TiN nanocrystals are elongated particles in the range of several hundreds of nanometres with a hardness of approximately 27 GPa. The hardness increases to ~35 GPa with the addition of less than 10 atomic percent of Si_3N_4, increasing the amount of Si_3N_4. There is an increasing coverage of the TiN crystallites by Si_3N_4 which impedes the growth of the TiN crystallites and forces them to renucleate. Due to this disturbed growth, the particle size of the TiN crystallites decreases with the increase in hardness and continues till the size of the TiN particles is small enough to prevent any dislocation activity. Such small crystallites are only deformed upon moving single undeformed TiN nanocrystallites against each other and that requires a much higher energy than dislocation movements, hence this increases the hardness. The nanocomposites at this stage consists of grains of nanocrystalline TiN separated by a few monolayers of Si_3N_4. At higher Si_3N_4 concentration, the grain separation becomes such that the hardness of the material becomes similar to that of Si_3N_4.

1.2 Synthesis Routes to TMNs

The distinguishing factor in nitride synthesis over the oxides is the strong N≡N triple bond that requires twice as much energy as the O=O double bond to dissociate, and sensitivity to oxygen/moisture, especially at high temperature. As a result of this the reports on oxides are many more than those on nitrides. Recent developments in the field include on the synthesis of spinel nitrides (e.g. Si_3N_4), and morphologies like nanorods, microporous and mesoporous nitrides (Si_3N_4, Si-Al-N, Si-B-N), nanocrystals of high surface area (Mo_2N, VN, WN, TiN etc.) and self standing colloids of different band gaps (GaN, AlN, Ga-In-N) to name a few. The TMNs are synthesised using different techniques depending upon the required materials properties for a particular application.

1.2.1 Mechanochemical milling

The TMNs are traditionally synthesised via the direct nitridation of metal in N_2, carried out at high temperatures.[49] These high energy processes give rise to the product with metallic impurities and large particle sizes due to fast sintering of the metal. These problems have been solved to some extent in the mechanochemical milling process. This process has been quite successful in synthesising metal nitrides sometimes at RT and sometimes through post-synthesis annealing.[50, 51] The problem with this method is that long reaction times (several days) and a high pressure of N_2/NH_3. Often products are found to contain Fe impurities that have leached out from the metallic balls due to constant grinding of the hard materials. Furthermore the nanocrystals have defect-rich structures due to the constant beating. Modifications have been made to the process to hasten the reaction and hence reduce cost and improve purity of the product. Some of TMNs have been reported through enhanced mechanochemical milling techniques, such as synthesis of TiN using an electrical discharge,[52] SiN via combustion synthesis,[53] AlN improving pulverisation by using $LiOH.H_2O$,[54] and liquid-solid reaction for synthesis of TiN.[55]

There are also reports on the synthesis of ternary nitrides via ball milling of the ternary carbides in nitrogen or via the ball milling of the second metal with the binary nitride. The advantage of the latter method is that it is independent of the availability of the ternary carbide. Ternary nitrides of Fe_3Mo_3N and Co_3Mo_3N have been synthesised this way.[56]

1.2.2 Gas-Solid Reactions

Nanoscale metal nitrides are often synthesised via the ammonolysis of nanoscale metal particles, metal chlorides, oxides or sulfides. The nature of the precursor dictates the nature of the product. This method involves high temperature reactions, which can result in agglomerated products with very low surface area. Tsai et al[57] synthesised TMN nanoparticles by reducing the metal halides with sodadide, $[K^+(15\text{-crown-}5)_2Na^-]$. The purified metals or bimetallic nanoparticles were then heated under N_2 or NH_3 to obtain the nanocrystalline nitrides. They synthesised γ-Mo_2N (800 °C in N_2), Ta_3N_5 (650 °C in NH_3) and $NbN_{0.95}$ (800 °C in NH_3) along with the ternary nitrides Fe_3Mo_3N (>650 °C, N_2) and some previously unknown phases of Ba-Nb-N, Fe-Nb-N and

Cu-Nb-N. Organic impurities from the alkalides were found, especially when Ba was used as the metal precursor because of its higher reactivity. Li et al.[58] synthesised δ-Mo_2N and γ-Mo_2N by reacting MoO_3 in a N_2/H_2 mixture and NH_3 at 697 and 737 °C respectively. The latter is formed due to a pseudomorphic relationship to the MoO_3 whereas δ-Mo_2N is the thermodynamically more stable phase.

Nitridation of aminomolybdate precursors $(NH_4)_6Mo_7O_{24} \cdot 4H_2O$, $(NH_4)_2MoO_4$ and H_4MoO_3 has also been studied because of their layer structures similar to MoO_3.[59] A molybdenum oxynitride intermediate is formed in NH_3 at lower temperature (325°C). The ammonium paramolybdate and MoO_3 produce oxynitride intermediates when heated in ammonia at 450 and 510 °C, and ultimately produce a mixture of MoN and Mo_2N respectively. High surface area nitrides are produced from the paramolybdate and MoO_3 as they both lead to pseudomorphous products.

Porous crystalline Ta_3N_5 has been synthesised by the ammonolysis of Ta_2O_5 at 850 °C.[60] The surface area increased from 1.8 $m^2\,g^{-1}$ in Ta_2O_5 to 11.4 m^2g^{-1} in Ta_3N_5. This was due to the generation of pores in Ta_3N_5 owing to the void created by the replacement of $3O^{2-}$ ions with 2 N^{3-}. Zhang et al.[34] used Ta_2O_5 to obtain Ta_3N_3 with complete nitridation at lower temperature of 700 °C. Using Ta_2O_5 reduced the reaction temperature of Ta_3N_3 synthesis.

Sulfides have also proved to be good precursors for nitride synthesis and have produced phases which are normally not achieved with the oxide precursor. Ammonolysis of MoS_2 has been shown to produce δ-MoN selectively over γ-Mo_2N.[61] W_5N_6 has been obtained by the ammonolysis of the high surface area WS_2.[61]

1.2.3 Solid state metathesis reaction SSM

Solid state metathesis SSM reactions have been particularly effective in generating TMNs. The method has been claimed as a more energy efficient and cost effective synthesis route compared with the classical methods of nitride synthesis through repeated grinding, heating and cooling steps. The method involves the reaction between metal halides and alkali or alkaline earth metal nitrides as nitrogen sources of which Li_3N, Mg_3N_2, Ca_3N_2 and NaN_3 have been most popular. The method, being a solvent free solid state reaction, involves large activation energies to overcome the diffusion barrier. This initiation is achieved either through igniting the reagents at room temperature, grinding reagents together, heating samples in a furnace or igniting the reagent mixture with a filament. After initiation at room temperature, these reactions often reach temperatures well over 1000 °C in seconds or even less.[62, 63] The reactions are highly exothermic and become self propagating once initiated. The whole process is very brief, with a duration usually of less than 5 Sec, which keeps the nucleation and growth process very short, with a resulting in small crystallites and occasionally some metastable phases.[64, 65] The method is effective in generation of early transition metal mono-nitrides (TiN,[66] ZrN[67]) and partially successful with the group 5 mono-nitrides like TaN and NbN, which are contaminated with the sub-nitrides,[68] with particle sizes in the range of 20-50 nm. Metal nitrides such as Mo_2N, W_2N, Cu_3N (decomposition temperature less than 790°C), main group nitrides like AlN, GaN (decomposition temperature 877 °C), and Zn_3N_2 (decomposition temperature around 500 °C)

1.2.3 Solvothermal synthesis

Solvothermal methods for synthesis of metal nitrides can overcome some of the problems involved in solid state metathesis reactions. The solvothermal method may be seen as a modified SSM reaction where the metathetical reaction is carried out in a solvent at a temperature higher than the boiling point of the solvent.[69] This method has been particularly successful in synthesis of metastable phases. Nanocrystalline GaN has been reported via the reaction between $GaCl_3$ and Li_3N in benzene at 280 °C.[70] The product was mainly hexagonal with some rock salt phase. The formation of the rock salt phase at this low temperature is intriguing as rock salt GaN is normally produced only at high temperature and high pressure. Cu_3N,[71] InN,[72] and BN[73, 74] have also been reported from solvothermal methods. Recently nanoparticles of ZrN, HfN, NbN, Ta_3N_5 and TaN have been formed via solvothermal reactions of early transition metal chlorides and dialkylamides with $LiNH_2$ in mesitylene and benzene.[27] All preparations were carried out in autoclaves. The formation of Ta_3N_5 takes place via stepwise substitution of chloride groups and condensation with the elimination of NH_3. The $TaCl_5$ was found to be a little more soluble in benzene than in mesitylene, but is fully consumed in reactions carried out in either solvent. Reduction of $NbCl_5$ was carried in a similar kind of reaction. Reactions below show the synthesis of Ta_3N_5 and of NbN:

$$\mathrm{TaCl_5} \xrightarrow{\mathrm{5LiNH_2,\ -5LiCl}} \text{“}\mathrm{Ta(NH_2)_5}\text{”} \longrightarrow {}^{1}/_{3}\,\mathrm{Ta_3N_5} + {}^{10}/_{3}\,\mathrm{NH_3}$$

$$\mathrm{NbCl_5} \xrightarrow{\mathrm{5LiNH_2,\ -5LiCl}} \mathrm{NbN} + {}^{10}/_{3}\,\mathrm{NH_3} + {}^{1}/_{3}\,\mathrm{N_2} + \mathrm{5LiCl}$$

Reactions of metal (Zr, Hf or Ta) dialkylamides with $LiNH_2$ led in all cases to crystallization of the MN phase. These reactions suggested that solvothermal reactions are not as clean in mesitylene as they are in benzene. However the main disadvantage of this method is the decomposition of solvent during the nitridation reaction, which can incorporate high level of carbon in the crystal lattice of the final product.

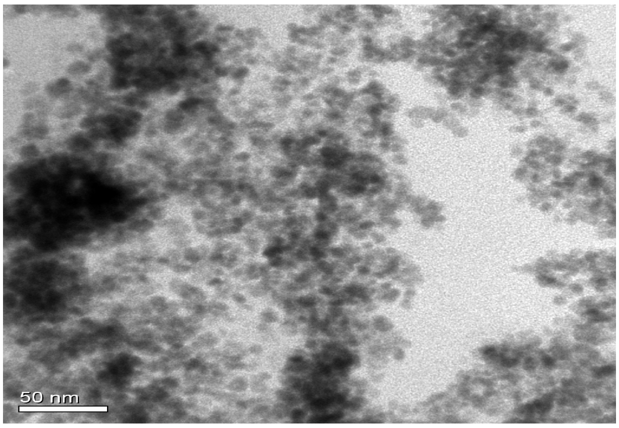

Fig. 1.3 TEM images of TaN produced by solvothermal reaction of $Ta(NMe_2)_5$ with $LiNH_2$

1.2.4 Precursor decomposition

Precursor-based synthesis of metal nitrides has been particularly successful in the synthesis of films via CVD, because of properties like volatility and solubility of precursors in normal organic solvents. Synthesis of colloidal nanocrystalline nitrides via precursor decomposition has also been gaining momentum over the last decade due to the new requirements of the optoelectronic industry that the feature size be reduced from 130 nm in 2002 to 22 nm in 2016.[75] Film development methods based on CVD may also not be able to provide acceptable film coverage in etched trenches and other such reduced features. This prompts different deposition methods like spin coating.[76, 77]

The precursor decomposition methods can be divided into two broad categories. One is the use of metal inorganic precursors involving M-N-H atoms and the other is metal organic precursors containing M-N-R linkages, both of which lead to MN particles. The advantage of the former is that it can produce pure metal nitrides with little or no C contamination. The disadvantage is that the decomposition of these precursors happens at a higher temperature and the lack of organic groups renders the precursors insoluble in all organic solvents preventing the possibility of any reaction in the solution phase. Metal-organic precursors, on the other hand, are soluble in organic solvents and have the potential of producing a colloidal dispersion of nitrides. Ideally the precursor has clusters or a molecular structure similar to that found in the desired final product.

Brown and Maya[78] used the inorganic route to synthesise ZrN, TiN and NbN. They treated metal dialkylamides with NH_3 to obtain a precipitate. The precipitate was then pyrolysed to obtain pure nitrides in the +3 oxidation state. Baxter et. al[79] reacted transition metal dialkylamides or hexamethyldisilyl amides with condensed NH_3 in THF, which resulted in a hydrocarbon insoluble product that showed a remarkable reduction in the carbon content compared to the starting material. The method can be looked upon as an extrapolation of the sol-gel method, except that the end product is a precipitate. The reactions proceed via transamination of the dialkyl amide. The precipitate was then pyrolysed under He to temperatures of 650-800 °C to obtain nanocrystalline (~30 nm or less) metal nitrides for the early transition metals and lanthanides. The late transition metals like Fe, Co, Cu produced the metals after heating. Reactions with mixed metal amides either produced a solid solution (Nb: Ta) or a mixture of the two nitrides (Ti:V).

Kaskel et. al.[80] synthesised TiN nanocrystals by heating different $TiCl_4$ complexes with ligands like aliphatic amines, ethers and bipyridines in NH_3 to temperatures between 700 and 1000 °C, depending on the nature of the precursor. This method is an easy and simple way of producing TiN nanocrystals of different morphologies and high surface area (>200 m^2/g) with very little impurity.

ZrN has also been reported by using tris(hexamethyldisilylamido)zirconium.[31] The precursor was pyrolysed under NH_3 or vacuum to obtain pure crystalline ZrN at 1075 °C. Advantages of this method are that the precursor is soluble in organic solvents and therefore has the potential for applications producing films and coatings.

Wolczanski et al.[81] used a single source metallorganic precursor designed to have the correct ratio of atoms needed to form TaN, (Fig. 1.4). They synthesised the precursor

[(^{t}BuCH$_2$)$_2$TaN]$_5$ in three different ways, via reactions of (^{t}BuCH$_2$)$_3$Ta=CH^{t}Bu with NH$_3$, (^{t}BuCH$_2$)$_2$Ta(NMe$_2$)$_5$ with NH$_3$, and (Me$_2$N)$_3$-Ta=N^{t}Bu with NH$_3$.

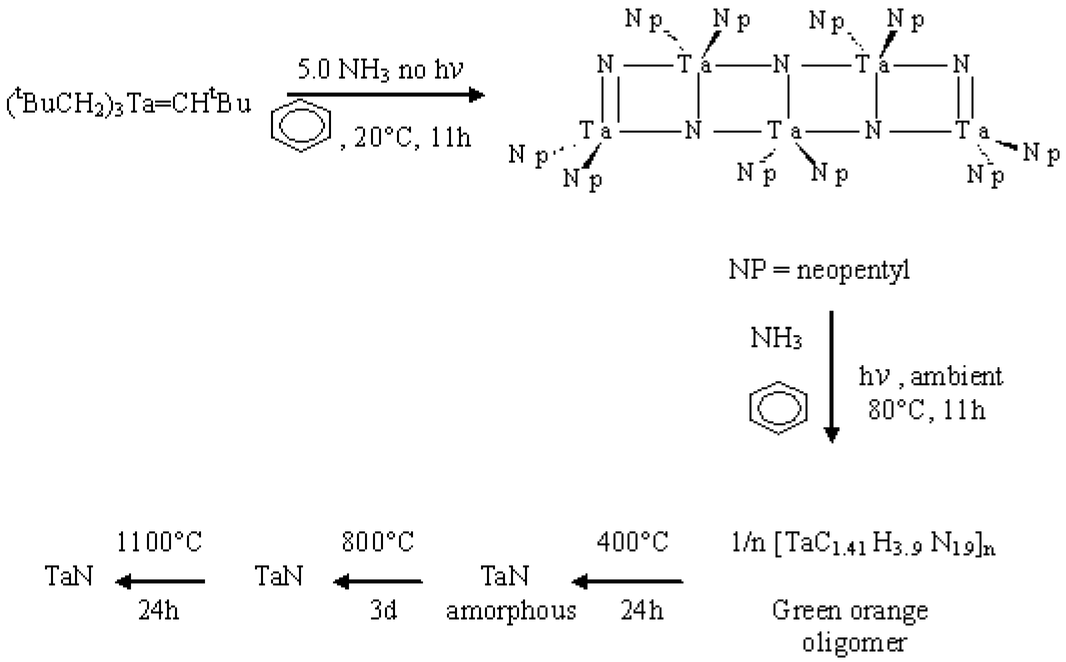

Fig. 1.4 Precursor methods for preparation of cubic TaN

Heating the precursor to 400 °C and 800 °C produced amorphous and nanocrystalline TaN respectively. Formation of the kinetically driven cubic phase in preference to the thermodynamically stable hexagonal phase was related to the structural similarities of the precursor and cubic TaN. Both the precursor and cubic TaN have corner-sharing structures whereas the hexagonal phase has TaN$_3$ and TaN$_6$ units, which makes its synthesis infeasible at this temperature.

Nano-crystals of δ–MoN and γ-Mo$_2$N have been reported[82] by heating two different Mo precursors, nitridotris(neopentyl)molybdenum(V) and its oxo-bridging bis(imido) derivative, in NH$_3$ to 700 °C. The C content was reduced from 2 to <0.1% by varying the temperature ramp rate between 100-200 °C/min. Nitrogen deficient Mo$_2$N was obtained when NH$_3$ was replaced by N$_2$ between 500 and 700 °C, but the carbon contents were higher than the ammonolysed product suggesting that the hydrocarbon removal was not complete at 500 °C in NH$_3$.

1.2.5 Non-oxide sol-gel method

The sol-gel method is well known for producing solids of different morphologies. Though the method has traditionally been used for the synthesis of oxides, it has now been successfully extrapolated to nitrides and chalcogenides, especially for formation of highly porous materials. The interesting morphologies produced by sol-gel chemistry (Fig. 1.5) have largely contributed towards applications in catalysis and ceramic materials.[83] Sol-gel processing takes place through a series of steps: controlled hydrolysis and condensation, gelation, ageing and drying.[84, 85] It is based on the formation of a stable suspension of colloidal particles (amorphous or crystalline) or polymer in a liquid, a sol.[86] This is subsequently linked up to immobilise the liquid phase in a porous, three dimensional solid network, this is referred to as a gel.[87, 88] The rate of condensation is controlled by various parameters, such as the properties of the starting material, e.g. diffusivities, reactivities, etc., their concentrations, reaction temperatures, solvent, and possible additives.[89]

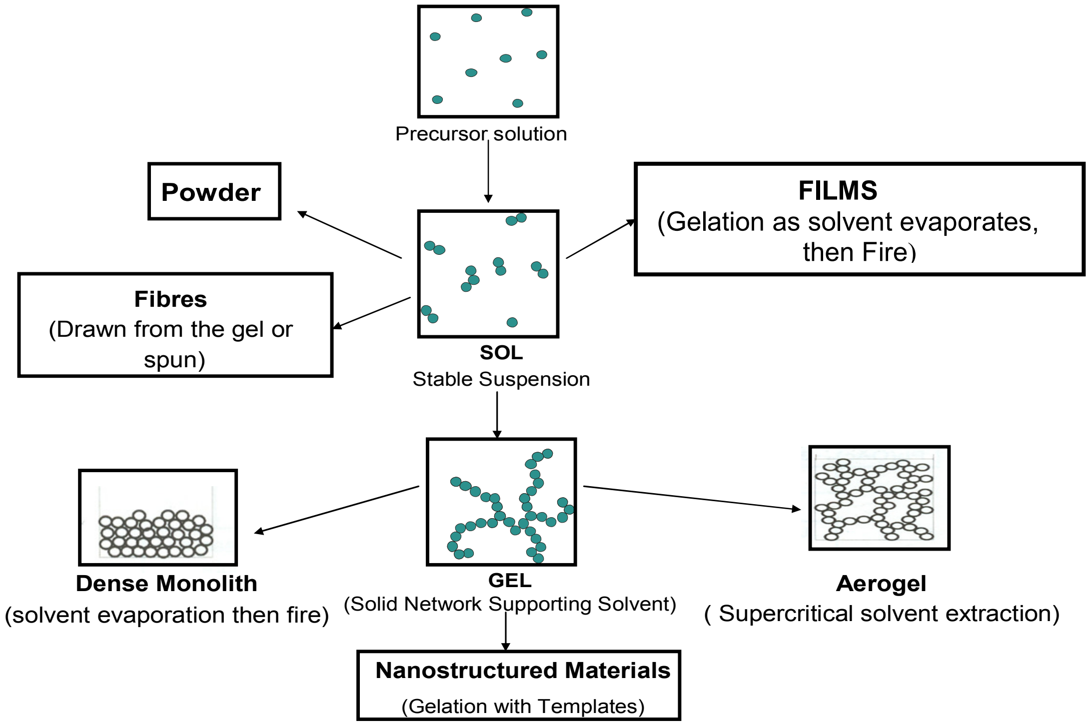

Fig. 1.5 Processing route to materials using sol-gel methods

Non-oxide routes have largely developed around silicon nitride. Kaskel[90] and co-workers have demonstrated the possibility to engineer the pore size of amorphous silicon nitride from a microporous framework. The NH and NH_2 groups, especially around the inner surface of the solid, have been functionalised to introduce other metals into the framework and in the process have produced nanocomposites of metal nitrides and silicon nitride. Such materials find use as hard materials and also as gas filters.[91]
Jansen et. al.[92] introduced transition metals into the silicon nitride framework. Three metal dialkyl amides, $Ti(NMe_2)_4$, $Ta(NMe_2)_5$ and $Zr(NMe_2)_4$ were chosen as they had similar ammonolysis rates to $Si(NHMe)_4$ which was considered essential to having a homogeneous distribution of metal and Si in the gel. The reaction can produce tertiary silicon nitrides by dissolving the two amides in a common solvent at low temperature and ammonolysing the solution to create a polymetallosilazane precipitate.

The aim of these reactions is described below:

$$M^1\text{-NRR'} + NH_3 \longrightarrow M^1\text{-NH}_2 + \text{HNRR'} \qquad \text{(Ammonolysis)}$$

$$M^1\text{-NH}_2 + M^2\text{-NRR'} \longrightarrow M^1\text{-NH-}M^2 + \text{HNRR'} \qquad \text{(Condensation)}$$

Scheme above describing co-ammonolysis of alkylamides. Note that well balanced reactivities of M^1 and M^2 will lead to a statistical mixture of M^1-NH-M^2, M^1-NH-M^1 and M-NH-M^2 linkages.

Heating the dried gels to 1000 °C in NH_3 produced composites of nanocrystalline metal nitrides in an amorphous Si/M/N matrix. The aim of this study was to synthesise a material with improved fracture strength and resistance to oxidation and thermal shock by incorporating transition metals into Si_3N_4. Cheng et al[93] have similarly developed nanocomposites of TiN nanocrystals in an amorphous mesoporous Si/Ti/N framework using the bis(dimethylamino)silylamino-μ-bis[(dimethyl-amino)silylimino] titanium as a precursor. Those composites are of interest as hard materials because of the combination of a nanocrystallites and an amorphous phase.
High surface area silicon aluminium nitride based xerogels have also been reported.[94] A solution of $[EtAl(\mu\text{-NHEt})(\mu\text{-NEt})_2Si(NHEt)]_2$ in pentane was placed in a 100 ml autoclave and ammonia was condensed on to it. The mixture was heated to 413 K

(P = 170 bar) for 12 hrs. The resulting solid had a high surface area (795 m^2g^{-1}) and was mesoporous. Cheng et al[95] produced mesoporous Si-Al-N xerogels by ammonolysis of the alanate $(C_4H_8O)Al[HNSi(NMe_2)_3]_3$ in the presence of triflic acid as a catalyst. The inorganic gel so formed was dried and pyrolysed in NH_3 to 200, 600 and 1000 °C. This procedure did not increase the basicity as intended but did provide an easy way of incorporating another element into silicon nitride.

1.2.5.1 Advantages and limitations of sol-gel processes for nitrides

Sol-gel reactions are low temperature processes and therefore a large degree of control over morphology and composition can be achieved. These processes can produce highly porous nanocrystalline materials or dense ceramic bodies. Pore size can be tailored by the modification of reagents or the control of initial nucleation and/or condensation. The casting of complex shapes can be achieved without the need for melting or machining due to synthesis via a gel. Amorphous materials can be produced if the synthesis is carried out place below the materials crystallisation temperature.

There are a number of challenges to be met in order to make sol-gel processing as useful in nitride synthesis as it is with oxides. The obvious precursors are amides, and these are often expensive, difficult to synthesise and very oxygen/moisture sensitive. Reactions with ammonia often also occur very rapidly and lead to precipitation. The control measures to control hydrolysis and condensation in oxide sol-gel chemistry are not obviously applicable to the amide-based equivalent, though some controlled preparations do exist.[96] Reactions of chlorides or amides with ammonia offer an interesting way to control synthesis of metal nitride powders and potentially to target high surface area or new compositions. These have been explored only superficially to date.

1. 3 Objectives

Solution phase ammonolysis for precursor synthesis presents itself as an effective technique for the synthesis of nitride nanoparticles based on molecular precursor decomposition. This technique could access a variety of morphologies and particle sizes which would be of great interest for their use in catalysis. The use of an oxygen-free precursor source avoids contamination by oxygen and the reactions are carried out at relatively low temperature and short time scale to produce the metal nitrides, saving energy and reaction time.

This thesis describes the use of solution phase ammonolysis to synthesise polymeric precursors which are decomposed by heating under ammonia to a give amorphous or crystalline products.

The incorporation of transition metals into silicon nitride using a sol-gel approach has previously been used to produce metal/silicon nitride nano-composites aiming for use as hard materials, with improved resistance to oxidation or thermal shock.[91, 92] Both binary nitrides with small particle sizes and well controlled compositions, and silicon nitride with incorporated metal atoms or supported metal nitride nanoparticles, could be of interest for catalysis. Hence this work has concentrated on tantalum and molybdenum nitrides, and the incorporation of these metals in to silicon nitride.

1.4 References

1. K. S. Weil, Y. J. Kim and P. N. Kumta, *Mater. Lett.*, 1999, **39**, 292.
2. L. E. Toth, *Refrectory Materials, Transition Metal Carbides and Nitrides*, 1971, **7**, 12.
3. J. B. Christian, S. P. E. Smith, M.S.Hittingham and H. D. Abruna, *Electrochem. Comm.*, 2007, **9**, 2128.
4. Y. H. Hu and E. Ruckenstein, *Industrial Eng. Chem. Res.*, 2007, **47**, 48.
5. S. T. Oyama, *The Chemistry of Transition Metal Carbides and Nitrides*, Blackie, Glasgow, 1996

6. D. H. Gregory, *J. Chem. Soc., Dalton Trans.*, 1999, 259.
7. J. S. J. Hargreaves and D. Mckay, *Catalysis*, 2006, **19**, 85.
8. E. Horvath-Berdon, R. Riedel, A. Zerr, P. F. McMillan, G. Auffermann, Y. Prots, W. Bronger, R. Kniep and P. Kroll, *Chem. Soc. Rev.*, 2006, **35**, 987.
9. *Handbook of Ceramic Hard Materials*, R. Riedel(Ed.), Wiley, 2000.
10. R.-J. Xie and N. Hirosaki, *Sci. Technol. Adv. Mater*, 2007, **8**, 588.
11. D. H. Gregory, *Coord. Chem. Rev.*, 2001, **215**, 301.
12. F. L. Riley, *J. Amer. Ceram.*, 2000, **83**, 245.
13. B. Mazumder and A. L. Hector, *J. Mater. Chem.*, 2009, **19**, 4673.
14. R. B. Levy and M. Boudart, *Science*, 1973, **181**, 547.
15. A. H. Cowley, R. A. Jones, C. M. Nunn and D. L. Westmoreland, *J. Mater. Chem.*, 1990, **2**, 221.
16. M. Nagai, Y. Goto, A. Miyata, M. Kiyoshi, K. Hada, K. Oshikawa and S. Omi, *J. Catal.* , 1998, **182**, 292.
17. L. Volpe and M. Boudart, *J. Solid State Chem.*, 1985, **59**, 348.
18. L. Volpe and M. Boudart, *J. Solid State Chem.*, 1985, **59**, 332.
19. G. J. Choi, R. L. Curl and L. T. Thompson, *J. Catal.*, 1995, **146**, 218.
20. C. W. Colling and L. T. Thompson, *J. Catal.*, 1996, **146**, 193.
21. J. Trawczynski, *Catal. Today*, 2001, **35**, 343.
22. B. Mazumder and A. L. Hector, *Top. Catal.*, 2009, **52**, 1472.
23. S. T. Oyama, *Solid State Chem.*, 1992, **96**, 442.
24. L. Ramqvist, *J. Appl. Phys.*, 1971, **42**, 2113.

25. S. Wang, X. Wang, Z. Zhang and Y. Qian, *J. Mater. Sci.*, 2003, **38**, 3473.
26. R. N. Panda and S. Kaskel, *J. Mater. Sci.*, 2006, **41**, 2465.
27. B. Mazumder, P. Chirico and A. L. Hector, *Inorg. Chem.*, 2008, **47**, 9684.
28. S. T. Oyama, *Catalysis*, 1992, **133**, 358.
29. M. R. Hillis, C. Kemball and M. W. Roberts, *Trans. Faraday Soc.*, 1996, **62**, 3570.
30. R. Kojima and K.-I. Aika, *Appl. Catal. A: Gen.,*, 2001, **215**, 149.
31. C. K. Narula and L. F. Allard, *J. Mater. Chem.*, 1998, **8**, 1881.
32. M. G. Barker, M. G. Francesconi, P. M. O'Meara and F. C. Baker., *J. Alloys Compd.*, 2001, **317-318**, 186.
33. S. Kaskel, K. Schlichte and T. Kratzke, *J. Mol. Catal. A: Chem.*, 2004, **208**, 291.
34. Q. Zhang and L. Gao, *Langmuir*, 2004, **20**, 9821.
35. B. Fu, L. Gao and S. Yang, *J. Amer. Ceram. Soc.*, 2007, **90**, 1309.
36. T.-C. Liu, W. G. Pell, B. E. Conway and S. L. Roberson, *J. Electrochem. Soc.*, 1998, **145**, 1882.
37. D. Choi, E. Blomgren and P. N. Kumta, *Adv. Mater.*, 2006, **18**, 1178.
38. D. Choi, G. E. Blomgren and P. N. Kumta, *J. Electrochem. Soc.*, 2006, **153**, A2298.
39. D. Choi and P. N. Kumta, *J. Amer. Chem. Soc.*, 2007, **90**, 3113.
40. C. Z. Deng, R. A. J. Pynenberg and K. C. Tsai, *J. Electrochem. Soc.*, 1998, **145**, L61.
41. D. Choi, G. E. Blomgren and P. N. Kumta, *Adv. Mater.*, 2006, **18**, 1178.
42. C. Z. Deng, R. A. J. Pynenberg and K. C. Tsai, *J. Electrochem. Soc.*, 1998, **153**, L61.
43. S. H. Jhi, J. Ihm, S. G. Louie and M. L. Cohen, *Nature (London)*, 1999, **399**, 132.
44. A. J. Perry, *J. Vac. Sci. Tech.*, 1988, **A 6**, 2140.
45. I. Pollini, A. Mosser and J. C. Parlebas, *Phys. Rep.*, 2001, **355**, 1.
46. J. Patschieder, *Mater. Res. Bull.*, 2003, **28**, 180.
47. H. Hochst, R. D. Bringans, P. Steiner and T. Wolf, *Phys. Rev.* , 1982, **B 25**, 7183.
48. D. J. Kim, Y. B. jung, M. B. Lee, Y. H. Lee, J. H. Lee and J. H. Lee, *Thin Solid Films*, 2000, **372**, 276.
49. G. Selvasuray and L. Sheet, *Mater. Sci. Technol.*, 1994, **9**, 463.
50. A. Calka, *Appl. Phys. Lett.*, 1991, **59**, 1568.
51. J. M. Criado, M. D. Alcala and C. Real, *Solid State Ionics.*, 1997, **101**, 1387.

52. A. Mosbah, A. Calka and D. Wexler, *J. Alloys Cmpd.*, 2006, **424**, 279.
53. A. B. Jin, Y. Yang, Y. X. Chen, Z. M. Lin and J. T. Li, *J. Amer. Ceram. Soc.*, 2006, **89**, 1099.
54. Y. Kameshima, M. Irie, A. Yasumori and K. Okada, *Solid State Ionics*, 2004, **172**, 185.
55. F. Zhang, W. A. Kaczmarek, L. Lu and M. O. Lai, *J. Alloys Cmpd.*, 2000, **307**, 249.
56. C. J. H. Jacobsen, J. J. Zhu, H. Lindelov and J. Z. Jiang, *J. Mater. Chem.*, 2002, **12**, 3113.
57. X. Z. Chen, J. L. Dye, H. A. Eick, S. H. Elder and K.-L. Tsai, *Chem. Mater.*, 1997, **9**, 1172.
58. S. Li, W. B. Kim and J. S. Lee, *Chem. Mater.*, 1998, **10**, 1853.
59. C. H. Jaggers, J. N. Michaels and A. M. Stacy, *Chem. Mater.*, 1999, **9**, 150.
60. D. Lu, G. Hitoki, E. Katou, J. N. Kondo, M. Hara and K. Domen, *Chem. Mater.*, 2004, **16**, 1603.
61. R. Marchand, F. Tessier and F. J. Disalvo, *J. Mater. Chem.*, 1999, **9**, 297.
62. P. R. Bonneau, R. F. Jarvis and R. B. Kaner, *Nature*, 1991, **349**, 510.
63. I. P. Parkin, *Chem. Soc. Rev.*, 1996, 199.
64. J. C. Fitzmaurice and I. P. Parkin, *Polyhedron*, 1993, **12**, 1295.
65. R. E. Treece, E. G. Gillan and R. B. Kaner, *Comments Inorg. Chem.*, 1995, **16**, 313.
66. U. A. Joshi, S. H. Chung and J. S. Lee, *J. Solid State Chem.*, 2005, **178**, 755.
67. J. C. Fitzmaurice, A. L. Hector and I. P. Parkin, *J. Chem. Soc. Dalton. Trans.*, 1993, 2435.
68. A. L. Hector and I. P. Parkin, *Chem. Mater.*, 1995, **7**, 1728.
69. G. Demazeau, *J. Mater. Sci.*, 2008, **43**, 2104.
70. Y. Xie, Y. Qian, W. Wang, S. Zhang and Y. Zhang, *Science*, 1996, **272**, 1976.
71. J. Choi and E. G. Gillan, *Inorg. Chem.*, 2005, **29**, 1610.
72. R. A. Janes, M. A. Low and R. B. Kaner, *Inorg. Chem.*, 2003, **42**, 2714.
73. X. Hao, M. Yu, D. Cui, X. Xu, Q. Wang and M. Jiang, *J. Cryst. Growth*, 2002, **241**, 124.
74. L. Chen, Y. Gu, Z. Li, Y. Qian, Z. Yang and J. Ma, *J. Cryst. Growth*, 2005, **273**, 646.

75. *International Technology Roadmap for Semiconductors*, , 2002 Update, Semiconductor Industry Association, 2002.
76. S. J. Martin, J. P. Godschlax, M. E. Mills, E. O. Shaffer and P. H. Townsend, *Adv. Mater.*, 2000, **12**, 1769.
77. K. Mosig, T. Jacobs, K. Brennan, M. Rasco, J. Wolf and R. Augur, *Microelectron. Eng.*, 2002, **64**, 11.
78. G. M. Brown and L. Maya, *J. Amer. Ceram. Soc.*, 1998, **71**, 78.
79. D. V. Baxter, M. H. Chisholm, G. J. Gama, V. F. Distasi, A. L. Hector and I. P. Parkin, *Chem. Mater.*, 1996, **8**, 1222.
80. S. Kaskel, K. Sclichte and G. Chaplais, *J. Mater. Chem.*, 2003, **13**, 1496.
81. M. M. B. Holl, P. T. Wolczanski and G. D. V. Duyne, *J. Amer. Chem. Soc.*, 1990, **112**, 7989.
82. N. A. K. Hansen and W. A. Herrmann, *Chem. Mater.*, 1998, **10**, 1677.
83. A. L. Hector, *Chem. Soc. Rev.*, 2007, **36**, 1745.
84. H. J. Schmidt, *J. Non-Cryst. Solids*, 1988, **100**, 51.
85. D. R. Ulrich, *J. Non-Cryst. Solids*, 1988, **100**, 174.
86. B. E. Yoldas, *Bull. Amer. Ceram. Soc.*, 1975, **54**, 286.
87. U. Schuber and N. Husing, *Synthesis of Inorganic Material*, 2nd edition, WILEY-VCH verlag GmbH & Co. KGaA, Weinheim 2004.
88. L. L. Hench and J. K. West, *Chem. Rev.*, 1990, **90**, 30.
89. A. Hannemann, J. C. Schon and M. Jansen, *J. Mater. Chem.*, 2005, **15**, 1167.
90. S. Kaskel, K. Schlichte and B. Zibrowius, *Phys. Chem. Chem. Phys.*, 2002, **4**, 1675.
91. F. Cheng, B. Toury, F. Lefebvre and J. S. Bradley, *Chem. Comm.*, 2003, 242.
92. J. Loffelholz, J. Engering and M. Jansen, *Z. Anorg. Allg. Chem.*, 2000, **626**, 963.
93. F. Cheng, S. M. Kelly, S. Clark, N. A. Young, S. J. Archibald and J. S. Bradley, *Chem. Mater.*, 2005, **17**, 5594.
94. S. Kaskel, G. Chplais and K. Schlichte, *J. Mater. Chem.*, 2005, **17**, 181.
95. F. Cheng, S. M. Kelly, F. Lefebvre, S. Clark, R. Supplit and J. S. Bradley, *J. Mater. Chem.*, 2005, **15**, 772.
96. A. W. Jackson and A. L. Hector, *J. Mater. Chem.*, 2007, **17**, 1016.

2. Instrumental techniques

This chapter describes the main techniques used to characterise the composition, morphology and structure of compounds made in this project.

2. 1 Thermogravimeteric analysis

Themogravimetric analysis (TGA) is a thermal analysis technique in which the change in sample mass can be followed over a period of time during heating under an inert or reactive gas. It was used herein to determine the thermal stability of the material and the fraction of the volatile components. TGA was performed using a Mettler Toledo TGA/ SDTA851e, (Fig. 2.1).

Due to the high air sensitivity of the amide precursors and nitride products, the equipment was mounted inside a glovebox filled with nitrogen. Hence the risk of partial oxidation of the sample during handling, which would result in inaccuracies during analysis, was minimised.

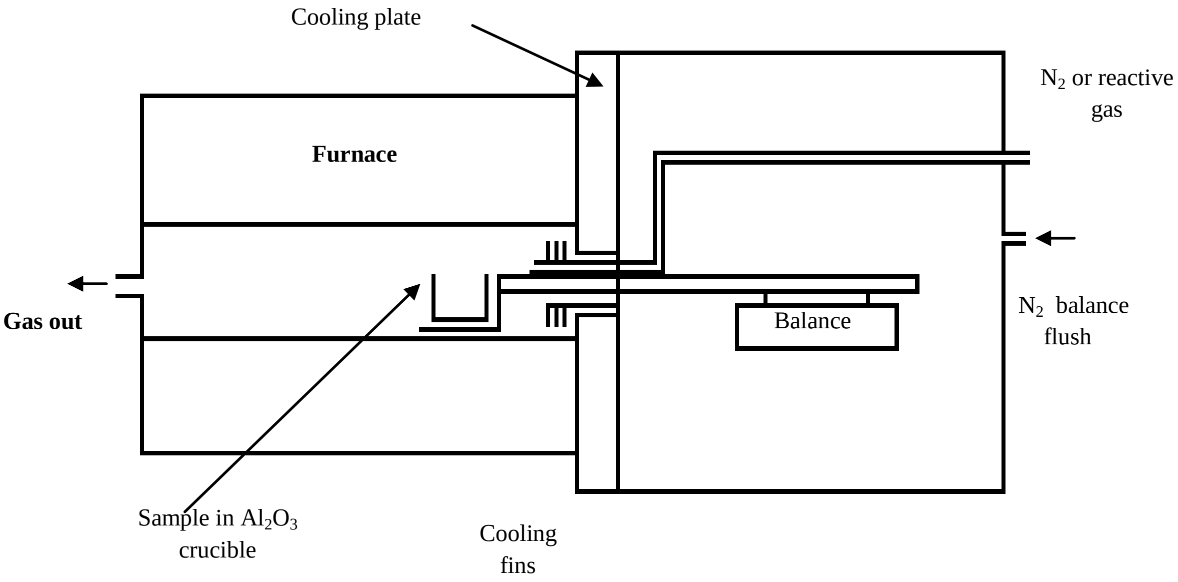

Fig. 2.1 A schematic diagram of the Mettler Toledo TGA851e

Pre- programmed heating regimes were adopted for the TGA samples heated under a flow of very high purity nitrogen (Air Products BiP grade). The sample (between 10–30 mg) was loaded in a dry alumina crucible (vol: 150 μL) and then placed onto the balance arm within the analyser. It was held at 25 °C for 10 minutes before gradually heating to 800 °C at a heating rate of 10 °/min under a flow of gas (50 mL/min) for the whole procedure. At 800 °C the sample was then held for 20 or 60 minutes before allowing it to cool back to 25 °C. The balance assembly measures the initial sample mass and then continuously monitors any change in mass as a function of temperature and time throughout the procedure.

2.2 Microanalysis

Combustion microanalysis was carried out on precursor materials and annealed nitrides. Information of the quantities of carbon, hydrogen, nitrogen and chlorine were collected. This information can be used as a guide to sample stoichiometry compared to calculated percentage composition based on ideal materials. Around 5–15 mg of sample was sealed inside the glovebox and sent to MEDAC Ltd., Egham, Surrey, who handled samples in the glovebox. Different precursors as well as the annealed products were analysed to compare the C, H and N concentration.

2.3 Powder X-ray diffraction (PXD)

Powder X-ray diffraction (PXD) is a versatile, non-destructive technique that reveals detailed information about chemical composition and crystallographic structure. For the samples to be susceptible to this technique they must possess a crystalline structure. The sample can then reflect incident X-ray photons in a manner which is unique to the atomic arrangement within the material allowing it to be indexed against known reflections and consequently identified.

The process of X-ray generation involves electrons being excited off of a cathode and accelerated through a strong electrical potential, usually in the region of 30-40 kV. The electrons collide with a metal plate, usually copper due to its high thermal conductivity and ability to produce strong K_{α} and K_{β} X-ray fluorescence. This is the radiation used to interact with the powdered target sample.

The radiation possesses a mixture of different wavelengths and to simplify the crystallographic data it is monochromated. The monochromator is a single crystal, which is mounted in a given orientation to diffract X-ray photons of specific wavelengths only. This not only simplifies the data analysis, as only one series of reflections is produced, but also removes radiation that degrades the sample without contributing useful information.

The monochromated beam is then collimated to a single direction, by using either mirrors or a physical barrier, before if is allowed to strike the sample. Upon the radiation impacting the analyte, constructive interference is observed (Fig. 2.2) according to Bragg's law:

$$n\lambda = 2d\sin\theta$$

where λ is the X-ray wavelength

n is an integer (1, 2, 3, ..)

d is the inter-planar separation in the crystalline material

θ is the angle between the planes and the incident/scattered photo paths

The angle of diffraction, usually measured as 2θ, is related to the inter-planar spacing d, and hence to the size and shape of a particular unit cell. The intensities of the diffracted waves will depend on the type and arrangement of atoms in the crystal structure.

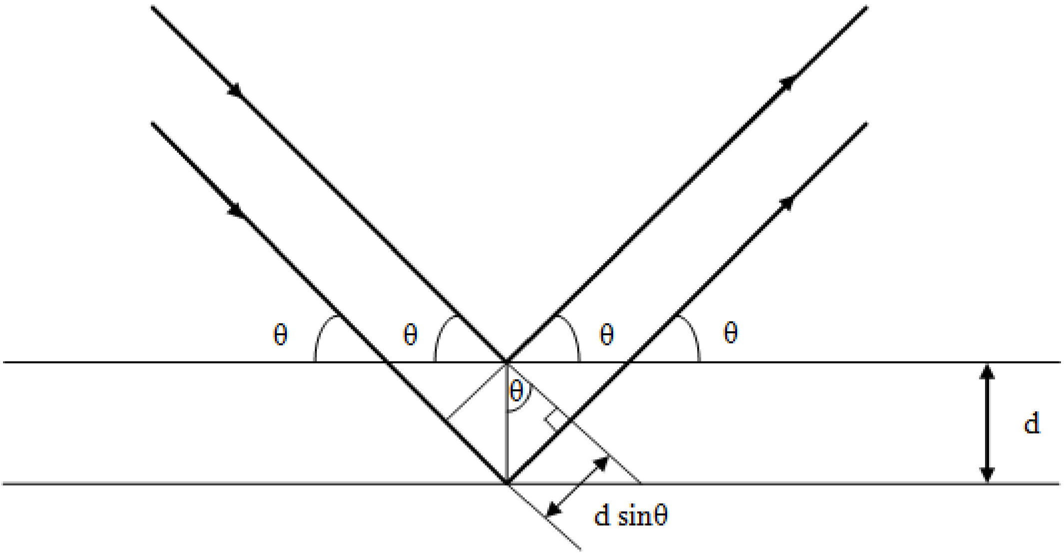

Figure 2.2 Schematic representation of scattering from parallel planes

2.3.1 PXD Instrumentation

Powder X-ray diffraction (PXD) data collection for this study was carried out using a Siemens D5000 diffractometer, in Bragg-Brentano geometery, commonly used for the study of inorganic solids since it minimises absorption by high atomic number elements. In order to keep a fixed relationship between the incident angle θ and the diffraction angle 2θ during the experiment, the sample is rotated a constant angular velocity whereas the detector is rotated at double this velocity.

X-rays of wavelength, 1.5406 Å (copper $K_{\alpha 1}$) are selected using a germanium single crystal monochromator. The monochromated beam is collimated by aperture slits and directed onto the sample. The diffracted beam passes through a second set of slits before reaching a NaI scintillating detector (Fig.2.3).

The data collected was analysed using the Diffrac Evaluation program (E.V.A.).[1] and the phases present were identified by comparison with the JCPDS[2] database.

Structural analysis was performed using General Structure Analysis Suite (GSAS).[3]

Samples were prepared inside a nitrogen filled glovebox and the powder was mounted in an air sensitive sample holder sealed with a plastic window in order to avoid any oxidation. The sample holder was attached to the diffractometer and data collected over a typical range of 20-80° 2θ.

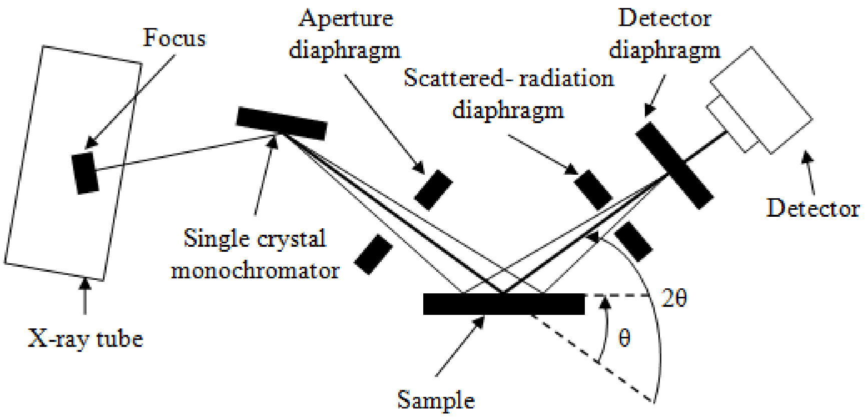

Fig. 2.3 Schematic representation of the D5000 diffractometer

2.3.2 The Rietveld method

Powder diffraction data often contains many overlapping peaks and structure factor extraction from the pattern is often difficult and sometimes impossible. In order to increase the amount of the information that could be extracted from powder data, H.M. Rietveld realised that although many reflections did overlap and thus could not be modelled as single entities, the total intensity and the peak shape of a cluster of reflections could be determined by using simple peak shape parameters.[4,5]

Many parameters can be varied while performing a powder data refinement using the Rietveld method. The typical procedure for the refinement of a structural model with X-ray powder diffraction data involves:

- Determination of an approximate model of the structure (e.g. using the ICSD database)
- Refinement of scale factor and an appropriate background
- Refinement of the lattice parameters and zero point
- Refinement of the atom positions in the structure
- Refinement of the isotropic thermal parameters
- Full refinement of peak shape parameters, in addition to any asymmetry or preferred orientation parameters which might be necessary.

Structures were refined to convergence, and all parameters (profile and structural) were refined simultaneously where possible to obtain correct estimated standard deviations on the refined values. The refinement is a least squares best fit process which aims to minimise the function M.

$$M = \sum_i w_i \, (y_i^{obs} - y_i^{calc})^2 \qquad \text{eq 2.3.1}$$

where w_i a weighting factor given by $1/y_i^{obs}$

y_i^{obs} is the observed intensity

y_i^{calc} is the calculated intensity

The calculated profile, y_i^{calc}, is determined from the structural model adding together the calculated contributions from neighbouring Bragg reflections (k) and the background b_i

$$y_i^{calc} = s \sum_i L_k \; |F_k|^2 \; \Phi(2\theta_i - 2\theta_k) \; P_k A + y_{bi} \qquad \text{eq. 2.3.2}$$

where s is the scale factor

L_k contains Lorentz, polarisation and multiplicity factors

Φ is the reflection profile function

F_k is the structure factor for the k^{th} Bragg reflection

P_k is the preferred orientation function

A is an absorption factor

y_{bi} is the background intensity at the i^{th} step

A comparison of intensities is performed at every point, consequently it is essential from to accurately describe the peak shape for the construction of the calculated profile. The peak shape obtained using the D5000 diffractometer is pseudo-Voigt constructed from Lorentzian and Gaussian contributions.

The Gaussian (G) and Lorentzian (L) contributions to the peak shape are described by the equations:

$$G = \frac{(4\ln 2)^{1/2}}{H_k\sqrt{\pi}}\exp\left[\frac{-4\ln 2(2\theta_i - 2\theta_k)^2}{H_k^2}\right] \qquad \text{eq. 2.3.3}$$

and

$$\boldsymbol{L = \frac{2}{\pi H_k}\,{}^{1}\Big/\left[1 + 4\,\frac{(2\theta_i - 2\theta_k)^2}{H_k^2}\right]} \qquad \textbf{eq. 2.3.4}$$

where $2\theta_k$ is the calculated position for the kth Bragg reflections corrected for the counter zero point and H_k is the full-width-at-half-maximum (FWHM) of the kth Bragg reflection. In order to make a quantitative assessment of the agreement between the observed and calculated profile a number of reliability factors are defined.

$$R_{profile} = R_p = 100\left[\frac{\sum_i |y_i^{obs} - y_i^{calc}|}{\sum_i y_i^{obs}}\right] \qquad \text{eq. 2.3.5}$$

$$R_{expected} = R_{exp} = 100\left[\frac{(N - P + C)^2}{\sum_i w_i\,(y_i^{obs})^2}\right]^{\frac{1}{2}} \qquad \text{eq. 2.3.6}$$

where

R_{exp} is defined from the statistics of the refinement

N is the number of observations

P is the number of refineable parameters

C is the number of constraints

From a mathematical view point, $R_{weighted\ profile}$ (R_{wp}) is the most significant of the R factors. This is so because the numerator is the residual being minimised. For identical reasoning it is the factor that best reflects the progress of a refinement and is given by:

$$R_{wp} = 100\left[\frac{\sum_i w_i\,(y_i^{obs} - y_i^{calc})^2}{\sum_i w_i\,(y_i^{obs})^2}\right]^{\frac{1}{2}} \qquad \text{eq. 2.3.7}$$

Another parameter minimised during the refinement is chi-squared defined by:

$$\chi^2 = \left[\frac{R_{wp}}{R_{exp}}\right]^2 \qquad \text{eq. 2.3.8}$$

For a good fit, the R_{wp} should approach the statistically expected R_{exp}. The goodness of fit can also be observed by examining a plot of the profile fit. The difference between calculated and observed patterns should be as flat as possible for a good fit.

2.3.3 Particle size estimation from GSAS Refinement

Particle size can be related to the observed peak shape in a diffraction pattern. Information on particle size can be extrapolated from the complex expressions derived to model the Gaussian and Lorentzian parts of the peak shape.

For PXD the particle size broadening can be obtained from the expression:

$$\frac{\Delta d}{d^2} = \frac{\Delta 2\theta \cot\theta}{d} = \text{constant} \qquad \text{eq. 2.3.9}$$

From Bragg`s law this becomes:

$$\frac{\Delta d}{d^2} = \frac{2\Delta 2\theta \cot\theta \sin\theta}{\lambda} \qquad \text{eq. 2.3.10}$$

The broadening is then:

$$\Delta 2\theta = \frac{\lambda \Delta d/d}{2\cos\theta} \qquad \text{eq. 2.3.11}$$

For PXD the Lorentzian coefficient, γ, of the peak shape is composed of two functions, X and Y (denoted LX and LY in the GSAS program) in the expression:

$$\gamma = \frac{X + X_s \cos\Phi}{\cos\theta} + (Y + Y_e \cos\Phi)\tan\theta \qquad \text{eq. 2.3.12}$$

where X_s and Y_e are anisotropic coefficients. The first term in the expression for the Lorentzian broadening, X, is of this form where:

$$X = \frac{\Delta d}{d^2} \qquad \text{eq. 2.3.13}$$

Rearranging this expression and converting from centideg to radians gives the particle size, p:

$$p = \frac{1800K\lambda}{\pi X} \qquad \text{eq. 2.3.14}$$

where K is the Scherrer constant, λ is the X-ray wavelength (1.540 Å) and X is the value of the L_x Lorentzian component extracted from the GSAS refinement.

The equation 2.3.14 has been used to calculate the particle size of all materials prepared in this work. Most of the products obtained at lower temperatures were found to be of low crystallinity. To obtain good resolution of peaks the patterns were collected overnight to obtain a good signal to noise ratio. The diffractometer peak shape was refined using α-quartz (SiO_2) as a standard. This material was selected because of its availability in pure and highly crystalline form, and also because its crystal structure is well characterised. The standard pattern was used to fix the Gaussian (mainly diffractometer-related) peak shape component, and only L_x (particle size) and L_y (strain) were refined for samples.

2.4 Infrared spectroscopy

Infrared spectroscopy is a straightforward method for identification of chemical bonds (functional groups) within molecules. It is concerned with changes in the dipole moment that are produced from vibration or rotation. The absorption of IR radiation depends on increasing the energy of vibration or rotation associated with a covalent bond. This increase results in a change in the dipole moment of the molecule or solid. Nearly all materials containing covalent bonds will show absorption in the IR. The only exceptions are homonuclear diatomic molecules because no mode of vibration or rotation produces a change in the electric dipole of the molecules. Generally, the absorption of IR photons may be due to either a change in the bond length (stretching) or alteration of the bond angles (bending). The former is usually denoted by the symbolism ν and the later as δ. Stretching can involve symmetric and asymmetric stretching modes.

IR experiments are typically based on passing IR radiation through a thin sample of compound and measuring which energies of the applied IR radiation are transmitted by the sample. IR spectra can be recorded for solids, liquids and gases using different sample arrangements. The absorption by a specific group occurs in a characteristic region of the spectrum. These absorptions appear as a series of peaks and are referenced by simply comparing them with tables of known compounds.[6] Similar frequencies occur in different molecules, therefore a vibration is considered as indicating the atoms involved and the strength of bond holding them together.

Infrared spectroscopy was performed using a PerkinElmer Spectrum One FT-IR spectrometer in conjunction with PerkinElmer’s analytical software Spectrum v3.05.

Solid samples were prepared by incorporating them into a pressed pellet of cesium iodide or potassium bromide for analysis. Due to the sensitivity of the precursor, the samples had to be prepared inside a nitrogen filled glovebox. A weighed portion of sample, approximately 0.2 mg, was mixed with 20 mg, of highly purified CsI or KBr using a pestle and mortar. The sample and CsI or KBr were well ground to reduce the particle size; otherwise the large particles would scatter the infrared beam causing a sloping profile in the baseline of the spectrum. CsI or KBr does not absorb in the region studied so will not interfere with the spectrum. The mixture was placed in an evacuable die and subjected to a pressure of 10 MPa for two minutes. The amide precursor samples, due to higher air sensitivity, were sealed between two CsI plates using a sample holder for air sensitive materials, while the nitride samples obtained at higher temperature were run quickly after taking out of the glove box, using a standard holder.

2.5 Ultraviolet-Visible spectroscopy

Transitons of electrons between valence energy levels are associated with energy changes in the range ~ 10^4 to 10^5 cm^{-1}. These energies span the near IR through the visible to UV, and are often associated with colour. Various types of electronic transition occur, the inner electron shells are localized on the individual atoms. The outermost shells may overlap to form delocalized bands of energy levels.

The appearance of a typical UV-visible absorption spectrum of a solid semiconductor is different to those observed for molecules. Above a certain energy or frequency known as the absorption edge, intense absorption occurs. To access frequencies above the absorption edge, reflectance techniques must be used. Broad absorption peaks or bands may also be observed at frequencies below that of the absorption cut-off.

Tantalum nitride samples obtained at 800 °C were analysed in diffuse reflectance geometry to measure their semi-conducting behaviour. A pure sample of Ta_3N_5 was used, treating as non-air sensitive material.

2. 6 Nuclear magnetic resonance spectroscopy

Nuclear magnetic resonance (NMR) spectroscopy depends on the spin quantum number, I, of a nucleus. Nuclei of certain isotopes have angular momentum. The total angular momentum depends on the spin quantum number I with value range from 0, $^1/_2$, 1, $^3/_2$,…. depending on the particular nucleus. If I=0, the nucleus does not have a spin and hence can not be observed by this method. Nuclei of I>0 have characteristic magnetic moments. When a magnetic nucleus is placed in an external uniform magnetic field, a discrete set of (2I+1) orientations will be adopted. For example, in nuclei with $I=^1/_2$ one of two possible orientations is assumed that correspond to energy level $\pm \mu H$ in applied magnetic field, where H is the strength of the external magnetic field and μ is the magnetic moment of the spinning nucleus. NMR spectroscopy utilises the magnetic spin energy of atomic nuclei of I= ½ such as ^1H, ^{13}C, ^{19}F, ^{31}P and ^{29}Si. A transition between these two energy levels is possible and may be effected by the absorption or emission of a discrete amount of energy such that $E= h\upsilon= 2\ \mu H$, where υ is the frequency of the electromagnetic radiation absorbed or emitted.

The difference in energy between these two states is given by:

$$\Delta E = \frac{\gamma h H}{2\pi}$$

where γ is the gyromagnetic ratio of nucleus under study.

The frequency of radiation that corresponds to this energy is called the resonance frequency.

2.6.1 Chemical shift

Each nucleus in a compound is surrounded by a cloud of electrons which are in constant motion. When a magnetic field H is applied to a sample these electrons are caused to circulate to oppose the field. This effect will result in shielding the nucleus from the external field value and the effective magnetic field H_{eff} experienced by nuclei will not be the same.

$$H_{eff} = H\ (1-\sigma)$$

Where σ is the shielding constant.

This shielding constant will vary as the local environment changes, especially with the electron density around the nucleus under study. This will affect the energy and hence the frequency required to be applied to cause a transition and therefore the resonance frequency characterises the surrounding environment of the nucleus.

The chemical shift (δ) is the ratio of the change of field necessary to achieve resonance to the field strength of the standard. It is usually expressed in ppm.

$$\delta = \frac{H_{sample} - H_{eff}}{H_{ref}}$$

If the degree of shielding of the nucleus under study increases, H_{eff} and hence the resonance frequency decrease. Consequently, the peak will be shifted to lower ppm value. For example the proton NMR signal of HI is at lower δ than that of HF since the F is more electronegative so will withdraw more electron density from the H compared with I. The shielding of the nucleus is influenced by the type of atoms surrounding it, so the chemical shift of nucleus under study can be used to determine the type of chemical environnment.

NMR spectra were collected using a Bruker AV300 equipped with an autosampler. The samples (~ 10 mg) were dissolved in deuterated benzene.

2.7 Electron microscopy

Electron microscopy (EM) uses electrons to create an image of the sample. Smaller objects and details can be detected compared with a light microscope since the wave length of the electrons is much shorter than that of visible light photons. Furthermore it has much higher magnification that reaches up to two million times which can be used to examine metals and crystalline structures and the characteristic morphologies of the various surfaces.

There are different types of electron microscope. Scanning electron microscopy (SEM) and transmission electron microscopy (TEM) have been utilised throughout the study for this thesis. These two types are similar in that both of them employ a beam of electrons which are directed to the specimen. Therefore certain characters in both instruments such as the electron gun, condenser lenses and vacuum system are similar.

2.8 Scanning electron microscopy

SEM is used to study the surface or near surface morphology of the solid material. The thermoionic gun, as shown in Fig.2.4, is the most widespread system for generating electrons. The filament, acts as a cathode, it is heated and the electrons emitted from it are accelerated by a positive potential applied down the gun column toward the anode and a beam of electrons is generated. A negative potential is applied to the ‘Wehnelt Cap’ so that any emitted electron from the filament is repelled by that cap toward the horizontal centre. The electrons are collected in the space between filament tip and Wehnelt Cap, called a space charge. Those electrons at the bottom of the space charge nearest to the anode can exit the gun area through a small hole moving down the column be used in imaging.

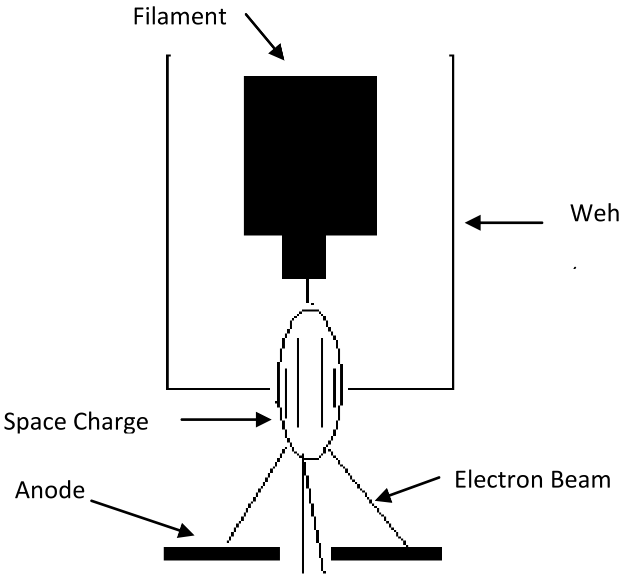

Fig.2.4 The electron gun

Once the stream of electrons departs the gun, it is passed through the first condenser lens that is used to form the beam and limit the amount of current in the beam. The beam is constricted by a condenser aperture which is used to eliminate the high-angle electrons from the beam. The second condenser lens forms the electrons into a thin, coherent beam and the objective lens focuses the scanning beam onto the desired part of specimen to be analysed, (Fig.2.5).

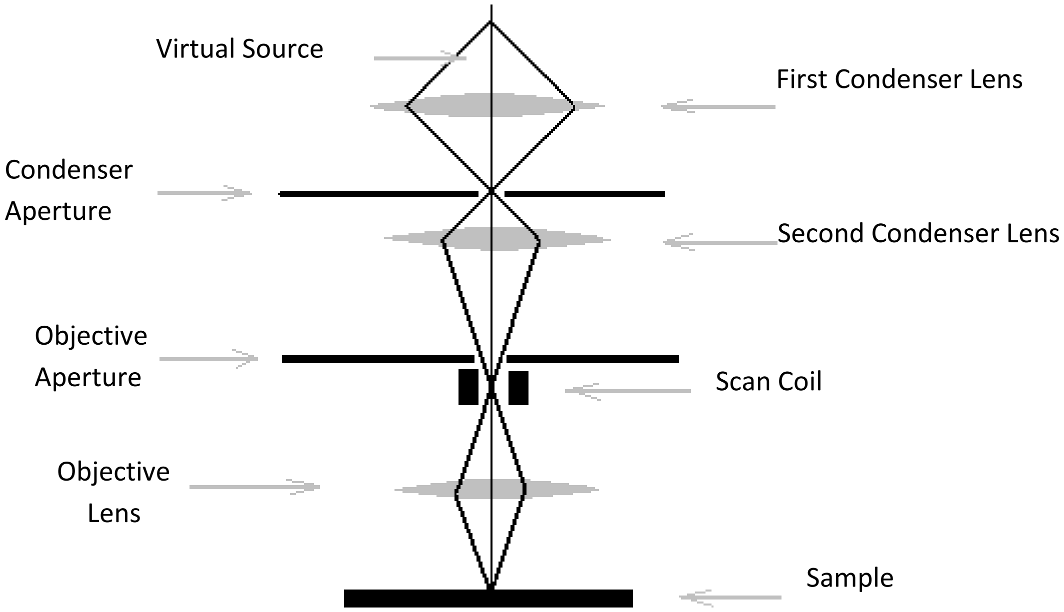

Fig. 2.5 A schematic representation of the SEM focussing process

Scanning electron microscopy was carried out using a JEOL JSM-5910 microscope to give surface morphologies of nitride powders produced. Samples were prepared inside the glovebox and mounted onto aluminium stubs using conductive carbon pads. The samples of tantalum nitrides were coated with gold while the samples of molybdenum nitrides were used without coatings as they are electrically conductive.

2.9 Transmission electron microscopy

In TEM transmission electron microscopy, a thin specimen is irradiated with an electron beam of uniform current density. Electrons are emitted from the electron gun and illuminate the specimen through a two or three stage condenser lens system. The objective lens provides the formation of either an image or a diffraction pattern of the specimen. The electron intensity distribution behind the specimen is magnified with a three or four stage lens system and viewed on a fluorescent screen. The image can be recorded digitally by a CCD camera.

TEM was carried out using on Hitachi H7000 with accelerating voltage of 75 kV at the Biomedical Imaging Unit, Southampton General Hospital. Samples were prepared by ultrasound dispersal using dry toluene as the solvent and were deposited on carbon coated Cu grids. The technique was used to obtain images of the morphology of the nanostructured particles and nanotubes, and approximate particle sizes.

2.10 Energy dispersive X-ray analysis

Energy dispersive X-ray (EDX) analysis was used in conjunction with SEM to semi-quantitatively analyse the solid material. Its capabilities are due to the principle that each element of the periodic table has a unique electronic structure and thus, a unique X-ray emission spectrum when excited by high energy electrons.

The detector used in EDX was a lithium drifted silicon detector operated at liquid nitrogen temperatures. When X-ray photons strike the detector, photoelectrons are generated within the body of the Si and as the photoelectrons travel through the Si, they generate electron-hole pairs which are attracted to opposite ends of the detector with the aid of a strong electric field. The size of the current pulse thus generated depends on the number of electron-hole pairs created, which in turn depends on the energy of the incoming X-ray photon. Thus an X-ray spectrum can be acquired giving information on the elemental composition of the material under examination.

In case of tantalum nitride gold coating prior to analysis was carried out to enhance the surface conductivity, for molybdenum nitride, the samples, which are inherently conductive, did not require either gold or carbon coating. Hence accurate elemental analysis could be performed, without corruption of the materials due to any additional conductive coating. The SiLi detector was protected by a boron nitride window so N was difficult to detect and any nitrogen contained within the samples was rendered invisible.

2.11 Extended X-ray Absorption Fine Structure (EXAFS) Spectroscopy

X-ray absorption spectroscopy has become a very powerful technique for the determination of local structure in a variety of different materials. It provides information on the number and the type of neighbouring atoms and their distances from the absorbing atom. Materials can be studied as crystalline solids, amorphous solids, solutions or gases. However, as XAS gives equal weighting to all absorbing atoms in a sample, the local structure information derived is an average over all the environments experienced by the excited atom. Another disadvantage of EXAFS is that it is a relatively weak effect that requires high signal to noise ratio. Using conventional X-ray sources, data collection times are typically 1 to 2 weeks[7] but using a synchrotron radiation source, data can be routinely collected in minutes or even seconds. Synchrotron radiation has a range of wavelengths from microwaves to hard X-rays, hence can provide the spectral range necessary to collect a spectrum, and is very intense.

2.11.1 EXAFS theory

On increasing the X-ray photon energy through the absorption edge of an element, a sharp increase in absorption is observed as the energy becomes sufficient to eject electrons from the core electronic states. Hence these absorption edges are characteristic of the atom types present in the sample. A typical X-ray absorption edge will contain two regions (Fig. 2.6), the region around the edge known as X-ray absorption near edge structure (XANES) and a post edge (EXAFS) region that has two distinct features known as the near edge X-ray absorption fine structure (NEXAFS) and extended X-ray absorption fine structure (EXAFS). The XANES region contains sharp spikes and bound valence levels. It yields a great deal of information about the local environment of the atom, but analysis is complex and it is less frequently used. The oscillatory nature of the post-edge region is related to the geometry and symmetry of the first co-ordination sphere around the atom being analysed, because the photoelectron ejected has a low kinetic energy and is therefore strongly scattered by the first shell of neighbouring atoms.

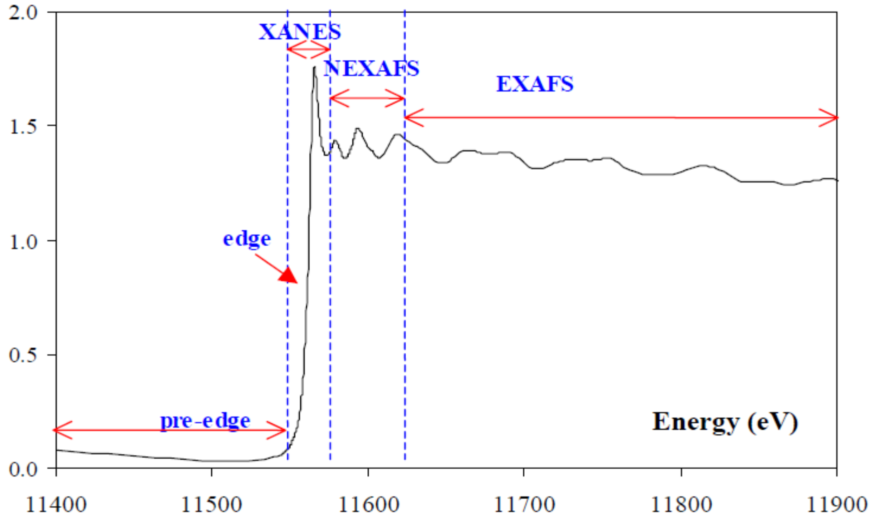

Fig.2.6 A typical X-ray absorption spectrum, showing the different regions used in spectroscopy

Basic theory of EXAFS was formulated by stern, Lytle and Sayers, which led to a short range single electron, single scattering theory.[8] There have been refinements and improvements to the original theory and for particle EXAFS analysis the theory is described by Poltorak and Boronin.[9]

The oscillations observed in the EXAFS region are due to constructive and destructive interference between the outgoing photoelectron and its backscattered component. The ejected photoelectron can be represented as an outgoing spherical wave originating from the X-ray absorbing atom. This backscattered electron wave may travel back through, and therefore interfere with, the excited absorbing atom (Fig. 2.7) resulting in a sinusoidal variation of the absorption coefficient, μ:

$$\mu(E)_x = [\mu(E)_s + \mu(E)_m + \mu(E)_0 + \mu(E)_{EXAFS}]_x$$

The total absorbance $\mu(E)_x$ depends on $\mu(E)_s$, the sloping spectrometer baseline, $\mu(E)_m$ the absorption due to the matrix in which the absorbing atom is embedded, $\mu(E)_0$, the absorption that would be observed for a free atom, and $\mu(E)_{EXAFS}$, the modulation in the absorption about $\mu(E)_0$. To be able to examine the EXAFS oscillation only, it is therefore necessary to isolate the EXAFS intensity $\chi(E)$ by subtraction of the background components and normalise it with respect to the free atom absorption:

$$\chi(E) = \mu(E)_{EXAFS}/ \mu(E)_0 = [\mu(E)/ \mu(E)_0]^{-1}$$

The frequency of the oscillations gives the distance (~ 1.5%) between the emitting atom and its neighbours, whilst the magnitude gives the co-ordination number (~ 1.5%).

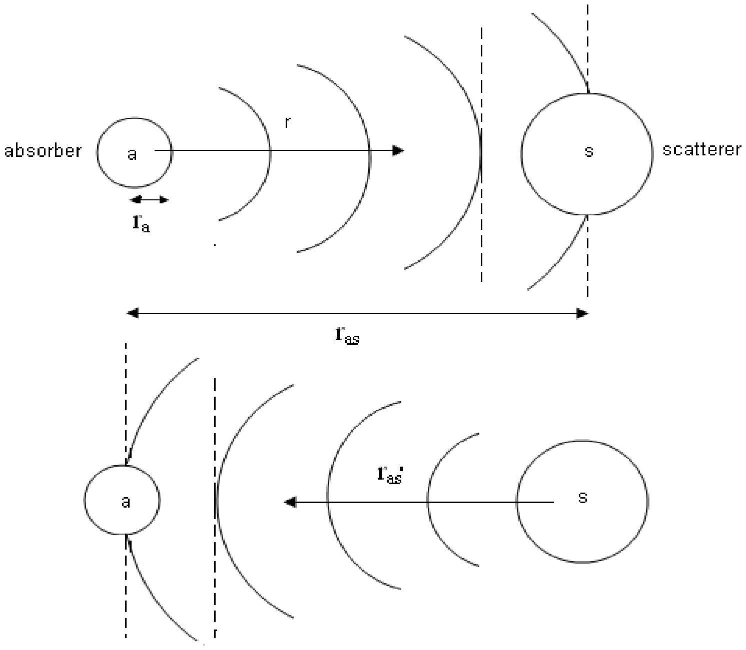

Fig. 2.7 Representation of outgoing and backscattered electron wave

Multiple scattering occurs when the emitted photoelectron encounters more than one backscattering atom before returning to the absorber. If one atom is behind another, relative to the absorbing atom, this will give a significant contribution to the EXAFS. The first neighbour in the system will have a focusing effect on the photoelectron, forward scattering it with increased intensity and a change of phase. This will result in the second backscattering shell giving a greatly enhanced signal. Multiple scattering pathways are included in an extended description of the curved wave theory,[10] while a further simplification of the theory obtained by an approximation to the wavefunction has enabled multiple scattering calculations to be included in EXAFS analysis.[11] Multiple scattering calculations are likely to be required if two different backscattering shells are bonded to each other with a bond angle of > 120°. As the bond angle increases, the effects of multiple scattering become more pronounced.

2.11.2 EXAFS experimental details

B18 is a general purpose XAS beamline on Diamond, located on a bending magnet radiation source. It was designed as a core XAS beamline to complement the more specialized activities undertaken at the other XAS beamlines at Diamond. It consists of a flat, cylindrically bent mirror collimator, a double crystal monochromator and a double bent cylinder focussing mirror. The water cooled monochromator has vacuum interchangeable Si(III) and Si(3II) cut crystals, and can access an energy range of 2 to 35 keV, covering the K-edges from P to I and L_{III} edges from Y to U, The beam is typically focussed to a ca 0.2 × 0.2 mm spot.

In this work, samples were prepared by grinding the sample with dry boron nitride and pressing into disks. These were mounted under nitrogen into an aluminium sample holder sealed with kapton tape. In order to minimise sample in homogeneity effects, the X-ray beam was defocused to a ca. 1 × 1 mm spot. Typically 2 × 20 min scans were collected across the Ta L_{III} edge region with pre and post-sample intensities monitored with ion chambers.

2.11.3 Background subtraction

The raw data was imported into the programme ATHENA. Its primary function is to convert raw data into the commonly accepted form of the absorption coefficient as a function of energy, $\mu(E)$, and to perform the background subtraction and normalisation steps prior to analysis; these last two processes are intrinsically linked in the programme.

The first step is the pre-edge background subtraction. The pre-edge line is a linear regression and corrects for the steady decrease in $\mu(E)$ as E increases – once the pre-edge extrapolation has been subtracted from $\mu(E)$, the pre-edge region of the spectrum should follow the $y = 0$ axis. This line is chosen by placing markers in appropriate positions on the spectrum, and is rather subjective as it is appraised visually. The post-edge line is a polynomial regression, typically quadratic. It corrects for very low-frequency sinusoidal variations in the data after the absorption edge, as well as providing the upper limit when calculating the edge jump. This should be chosen so that it passes through the middle of the EXAFS oscillations. After background subtraction the EXAFS is then k weighted to a power 1, 2, or 3 (i.e. k^1, k^2, k^3), so that the higher k values can be used for analysis. The shape of the EXAFS curve gives information on the nature of the backscattering atoms. The Fourier transform of k weighted EXAFS data is then calculated, to yield a spectrum of radial atom distance versus intensity. After obtaining the Fourier transform, the back transform between the window limits in r space (containing structural information) may be compared to the EXAFS.

2.11.4 Model fitting

The prepared EXAFS data can be analysed by the refinement of a theoretical structural model using the program ARTEMIS. It uses the FEFF multiple-scattering path calculations to generate the model, which, for a known crystalline system, can be generated from crystallographic data (such as a cif file) via another program, ATOMS; this is built into ARTEMIS. The crystal structure is converted to a form that can be read by FEFF, which in turn generates a detailed cluster model, giving a series of paths with precise information on the coordination number, path length and species involved.

These estimated paths are then used to construct an appropriate structural model that fits the experimental data well. ARTEMIS (via the IFEFFIT codes) does this by evaluating various parameters of the XAFS equation for each path, namely the coordination number, N, the amplitude reduction factor, S_0^2, the edge energy, E_0, the change in predicted scattering path length, ΔR, and the mean-squared relative displacement of the atoms, σ^2, which is also known as the Debye-Waller factor. Some of these parameters must be fixed to reasonable values during the fit; others should be left free in order to be refined by the fitting algorithm. Part of the challenge of EXAFS analysis is to know which parameters will provide the desired information on the system under study, and to choose appropriate values for the parameters that are fixed.

2.13 References

1. E.V.A., Bruker Advanced X-Ray Solution, GMBH Karlsruhe, 2004.
2. International Centre for Diffraction Data, 12 Campus Bompus Boulevard, Newton Square, Pennsylvania 19073, USA.
3. A. C. Larson and R. B. Von-Dreele, GSAS manual, LANSCE MS-H805, Los Alamos National Laboratory, Los Alamos NM, NM 8754, 2000.
4. H. M. Rietveld, *Acta Cryst*., 1967, **22**, 151.
5. H. M. Rietveld, *J. Appl. Cryst*., 1969, **2**, 65.
6. K. Nakamoto, Infrared and Raman Spectra of Inorganic Compounds, Theory and Applications in Inorganic Chemistry, Wiley-Interscience, 1997.
7. R. W. Joyner, Characterisation of Catalysts, Eds. J. M. Thomas and R. M. Lambert, Wiley, 1980, 237.
8. O. M. Corker and V. S. Boronin, Russian *J. Phys. Chem*, **40**, 1436.
9. G. Rayner, PhD Thesis, University of Southampton, 2002.
10. J. M. Corker, J. Evans and W. Levason, J. Chem. Soc., Chem. Commun., 1989, 181.
11. S. J. Gurman, N. Binsted and I. Ross, *J. Phys. Chem*., 1986, **19**, 1845.

3. Tantalum nitrides from ammonolysis of $Ta(NMe_2)_5$

3.1 Introduction

Ta_3N_5 has a band gap of 2.08 eV and is a useful red pigment, making it suitable for photovoltaic cells and other optoelectronic devices.[1] Ta_3N_5 is an active photocatalyst in the visible region of the electromagnetic spectrum, including a quantum efficiency of ca. 10% for overall water splitting, and has a good hydrolytic stability.[2, 3] It has also been investigated for use as a capacitor dielectric.[4] TaN thin films are considered attractive for use in embedded thin film resistors integrated into printed writing boards due to the durability, corrosion resistivity, and reliability of these films.[5-7] TaN is a potential material for application in high-temperature ceramic pressure sensors because of its good piezo-resistive properties.[8] It has also been found to be a histocompatible material for artificial heart valves.[9]

Several phases of TaN have been reported, typically obtained by tantalum nitridation in ammonia or nitrogen at high temperatures.[10, 11] Thin films of tantalum nitrides are often produced by CVD. The tantalum nitride system exhibits a remarkable richness with regard to the array of equilibrium and metastable phases that can form, with widely varying structural properties, depending on the preparation conditions.[12]

The synthesis and structure of seven different phases of tantalum nitrides have been reported by Terao[13] using X-ray diffraction and electron diffraction. His work reports transformation in the sequence $Ta_3N_5 \longrightarrow Ta_4N_5 \longrightarrow Ta_5N_6 \longrightarrow TaN \longrightarrow Ta_2N$ by heating thin films of Ta_3N_5 in vacuum, the N content decreases at relatively high temperatures in the range 600-1100°C. However they report that some of them still offer some ambiguous points as to their compositions and structures.

Lei and co-workers[14] studied the high pressure behaviour of Ta_2N in a diamond anvil cell using an in situ energy-dispersive synchrotron radiation technique. Ta_2N is stable with no structural transformation even if very high pressure is applied. The result was compared with other nitrides and the bulk modulus of Ta_2N is the highest for a nitride material. The high pressure investigation of hexagonal **ε**-TaN shows structural disordering in the **ε**-TaN structure at high pressure.[15] Kroll[16] has predicted novel polymorphs of Ta_3N_5 and WN_2 on the basis of quantum-chemical and thermochemical calculations. The *Cmcm* ground-state structure is the most stable modification of Ta_3N_5

up to 9 GPa. The transition to a new high pressure Ta_3N_5-II form, is predicted to be a possible using a diamond anvil cell at about 19 GPa.

Ta_3N_5 produced[17] by solvothermal reaction between $TaCl_5$ and $LiNH_2$ in mesitylene at up to 500 °C was amorphous and required further annealing to obtain crystalline Ta_3N_5. The product required washing with THF for several times to remove the LiCl by-product. Use of commercial $LiNH_2$ yielded Ta_3N_5 contaminated with $LiTaO_3$. Using high purity $LiNH_2$ produced Ta_3N_5 with large amounts of carbon contamination and Li was also detected. EDX analysis showed traces of Cl. Reactions of $TaCl_5$ with $LiNH_2$ in benzene resulted in nanocrystalline Ta_3N_5 at 500 or 550 °C, amorphous material was obtained at 450 °C.[18] Solvent decomposition led the carbon contamination with highly nitrogen deficient product. Cl and H were also found in small amounts. The reactions are given below:

$$3\,TaCl_5 + 15\,LiNH_2 \longrightarrow Ta_3N_5 + 15\,LiCl + 10\,NH_3$$

$$6\,TaCl_5 + 5\,Mg_3N_2 \longrightarrow 6\,TaN + 15\,MgCl_2 + 2\,N_2$$

Hector and co-workers[19] have demonstrated the synthesis of nanocrystalline Ta_3N_5 by ammonolysis of Ta_2O_5 at high temperature. Oxide impurity ions were found in the lattice even after extended heating periods under dry NH_3. The presence of oxide affected the optical band gap and lattice parameters of Ta_3N_5.

Reacting $TaCl_5$ with Li_3N or Mg_3N_2 has also produced tantalum nitrides by SSM reaction.[20, 21] Reactions were highly exothermic and were electrically or thermally initiated up to 900 °C. The final product was composed of agglomerated TaN crystals. Shi *et al.*[22] introduced NH_4Cl and Na, as a source of NH_3 and as a reducing agent, respectively, to lower the reaction temperature to 650 °C, which facilitated the controlled growth of TaN nanocrystals. Parkin and Rowley[23] reported the synthesis of Ta_3N_5 through SSM, using $LiNMe_2$ as a milder nitriding agent. The reaction was carried out at 300 °C, which produced an amorphous material. Annealing at 700 °C under NH_3 yielded Ta_3N_5 with unidentified impurities.

When $TaCl_5$ is reacted with NH_3 to produce Ta_3N_5 via CVD[24], corrosive HCl is produced during the reaction, which prevents its use for optoelectronic devices. Ta_3N_5 thin films produced using $Ta(NMe_2)_5/NH_3$ at lower temperature have been reported.[25, 26] Thin films of Ta_3N_5 have also been reported[27] by atomic layer deposition (ALD) using

$TaCl_5$ with NH_3 in an alternate surface reaction, while using Zn as an additional reducing agent TaN films were obtained.

In the present work a stepwise study of the decomposition of a polymeric precursor results in the formation of Ta_3N_5 or TaN. This structural behaviour has been measured through PXD and XAS data for samples obtained by the pyrolysis of a tantalum amide polymer in ammonia and for samples that have then been annealed in a thermogravimetric analyser under a nitrogen atmosphere at 800 °C for 20 or 60 minutes.

3.2 Experimental Section

3.2.1 *Ammonolysis of $Ta(NMe_2)_5$*

The reaction was carried out using a Schlenk line. ~20 ml of liquid ammonia was distilled into a solution of 2 g pentakis(dimethylamido)tantalum(V) in THF (20 ml) under nitrogen at -78 °C with continuous stirring. The reaction mixture was left to come to room temperature as the excess ammonia evaporated. The yellow precipitate of tantalum amide polymer ~1.2 g was then filtered and dried under vacuum.

3.2.2 *Pyrolysis of polymeric tantalum amide precursor*

The polymer was then transferred to a ceramic crucible (boat shape) inside a silica tube, which was loaded inside the glove box. The silica tube was provided with an arrangement of taps to allow flushing of the hoses before the sample was exposed to the gas flow. The sample tube was then heated under flowing ammonia to 500, 600, 700, and 800 °C separately for the duration of 2 hrs each. A column of molecular sieves (synthetic zeolite) was used to dry the ammonia.

3.2.3 *Measurements*

TGA was carried out in Mettler Toledo TGA/SDTA85le instrument under flowing BiP nitrogen with flow rate of 50 ml/min and temperature ramp rate of 10 °C/min. The temperature was raised from 25 to 800 °C increasing rate of 10 °C/min and was held at maximum temperature for 20 or 60 minutes. PXD patterns were collected with a Siemens D5000 using a sample holder for air sensitive material. TEM was performed on a Hitachi H7000 with an accelerating voltage of 75 kV. Samples were made by ultrasound dispersal using dry toluene as the solvent and were deposited on carbon coated Cu grids. A Jeol JSM5910 with an accelerating voltage of 10kV was used for the SEM. Samples were coated with gold. Samples were sent for combustion micro analysis for C, H and N to Medac Ltd. Infrared spectroscopy was performed using CsI disks on a Perkin Elmer Spectrum One FT-IR spectrometer. Perkin Elmer UV/Vis/NIR spectrometer was used to obtain UV-visible spectrum spectrum. The PXD data was refined using GSAS[28] and standard patterns were obtained from the inorganic crystal structure database (ICSD). Crystallite sizes were obtained using the method described in the GSAS manual.[29]

3.3 Results and Discussion

3.3.1 Analysis of polymer precursor

The FTIR spectra for the polymeric precursor (Fig.3.1) shows a broad peak at 3215 cm^{-1} which demonstrates the presence of ν (NH).[30] Low intensity peaks in the range of 3030-2760 cm^{-1} are attributed to ν (CH). The absorption peak at ca. 1609 cm^{-1} is consistent with δ (NH_2),[30, 31] and the peak at ca. 1263 cm^{-1} may be ν (CN). The strong band at 640 cm^{-1} is assigned to ν (M-N).[30]

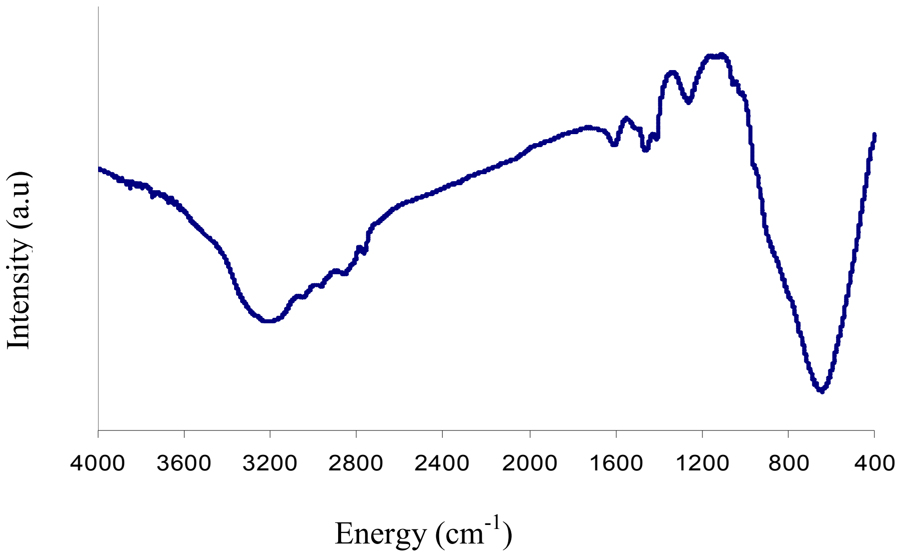

Fig. 3.1 IR-Spectrum of the polymeric tantalum amide precursor

The TGA trace of the polymeric precursor (Fig. 3.2) obtained through the ammonolysis of metal amides shows mass loss in two steps. Previous studies using TGA-MS[30] showed that loss of amine and ammonia due to further condensation reactions is observed at lower temperatures, whereas above 700 °C loss of N_2 due to reduction of the metal often occurs as well as ammonia loss due to further condensation as the diffusion barrier is overcome.

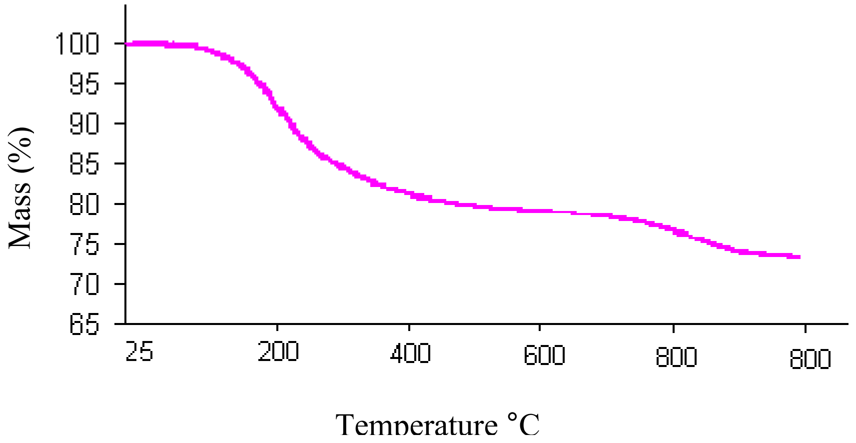

Fig. 3.2 TGA curve obtained by heating the polymeric tantalum amide precursor under nitrogen

3.3.2 Analysis of pyrolysed TaN_x samples

PXD studies were carried out in a step wise manner. In the first step patterns (Fig. 3.3) were collected for the samples obtained initially from the solution phase ammonolysis of $Ta(NMe_2)_5$ and further annealing the polymeric precursor at various temperatures under ammonia for 2 hrs. Patterns from samples heated at 700 °C and below showed amorphous humps resembling hexagonal TaN, the breadth of which decreased with increasing temperature. Phase pure orthorhombic Ta_3N_5 was obtained when the precursor was annealed at 800 °C under ammonia.

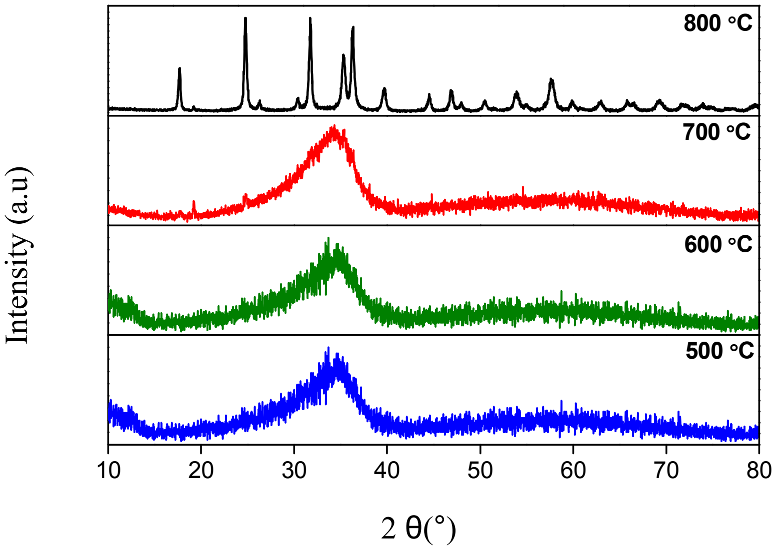

Fig. 3.3 The PXD patterns obtained for polymeric tantalum amide samples heated under ammonia at various temperatures. Peaks observed at 800 °C match those expected for orthorhombic Ta_3N_5. The broad humps at 700 °C are in similar postions to the main peaks of hexagonal TaN.

In the second step PXD patterns were collected (Fig. 3.4) for the samples obtained as above, then reannealed under nitrogen to 800 °C in the TGA and held at final temperature for 20 minutes. All the amorphous samples which were initially obtained at lower temperature were found to have started crystallizing to Ta_3N_5 structure. The broad amorphous peaks in the pattern are still observed for the samples initially obtained at 500 and 600 °C. This suggests that not all the material was transformed to crystalline product. No broad peaks were found in the pattern for the sample initially obtained at 700 °C, but the pattern still showed some noise at lower 2 theta angles. No change in the pattern was found for the sample initially obtained at 800 °C.

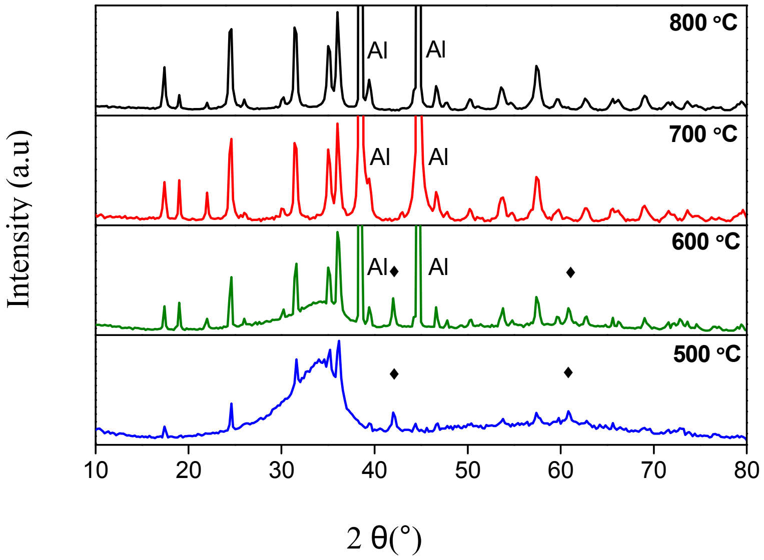

Fig. 3.4 The PXD patterns obtained after heating samples in ammonia at the temperature shown, then under N_2 in the thermogravimetric analyser furnace 800°C for 20 minutes. (◆) represent the peak positions corresponding to cubic TaN.

In a third step, samples which were initially obtained by annealing the polymeric precursor at 500-800 °C were re-annealed in the thermogravimeteric analyser under N_2, this time the samples were held at 800 °C for 60 minutes. The PXD patterns (Fig. 3.5) obtained at this stage showed no broad peaks or noise, suggesting that all the amorphous TaN_x samples were transformed to fully crystallised Ta_3N_5, with some cubic TaN appearing due to loss of N_2 at 800 °C. The sample initially obtained at 800 °C was still not affected and remained the phase pure Ta_3N_5, even though some N_2 loss was observed in the elemental analysis. Re-annealing the samples in the TGA also surprisingly lowered the carbon contents in the final product.

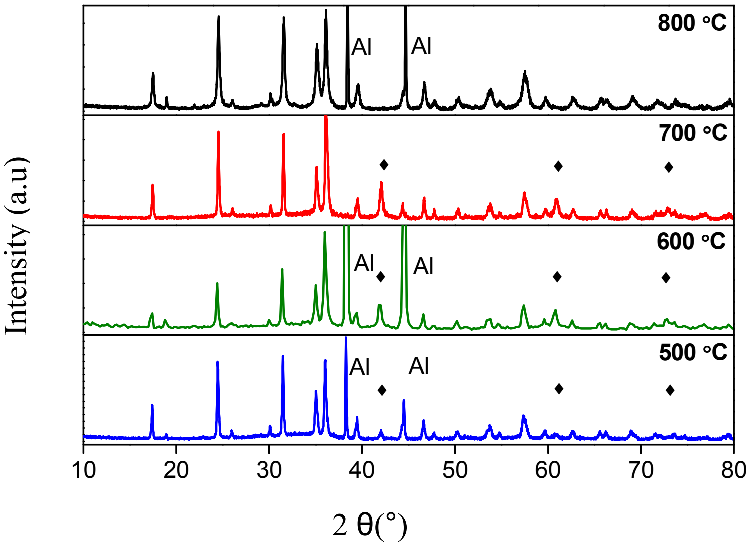

Fig. 3.5 The PXD pattern obtained after reannealing the samples in the TGA at 800 °C for 60 minutes under nitrogen flow of 50 ml/min and with a temperature ramp rate of 10 °C/min. (◆) represent the peak positions corresponding to cubic TaN.

Refining the PXD data for the of the phase pure Ta_3N_5 revealed a good fit to the known orthorhombic Ta_3N_5 structure[32,18] in space group *Cmcm* with the lattice parameters around a= 3.90Å b= 10.20Å and c= 10.28 Å (Fig. 3.6). The patterns obtained after reannealing the tantalum nitride samples obtained at various temperatures were refined using two phases for Ta_3N_5 and rock salt-type TaN (Fig. 3.7).

3.3.3 Discussion of the crystallisation studies

The PXD data show that annealing the polymeric tantalum amide precursor at 800 °C produces phase pure Ta_3N_5, while at 700 °C and below the amorphous material was obtained but can be transformed to crystallized Ta_3N_5 if reannealed under nitrogen. Further annealing the amorphous samples at 800 °C under nitrogen for longer time periods leads to more TaN with Ta_3N_5 lattice. The results from shorter annealing times suggest that the amorphous phase is well organised for formation of Ta_3N_5 but that less nitrogen is available for inclusion in the fully crystallized product. If the original ammonolysis temperature was higher then the product contained more nitrogen.

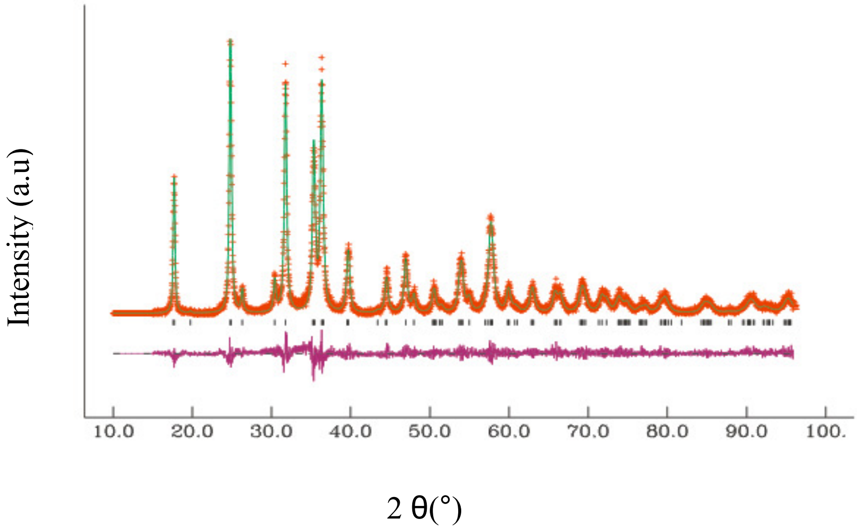

Fig. 3.6 Fit to the PXD data for the phase pure Ta_3N_5 obtained by pyrolysis of polymeric tantalum precursor at 800 °C in ammonia for 2 hrs. Crosses mark the data points, upper continuous line the calculated profile and lower continuous line the difference, tick marks are the allowed reflection positions of orthorhombic Ta_3N_5.

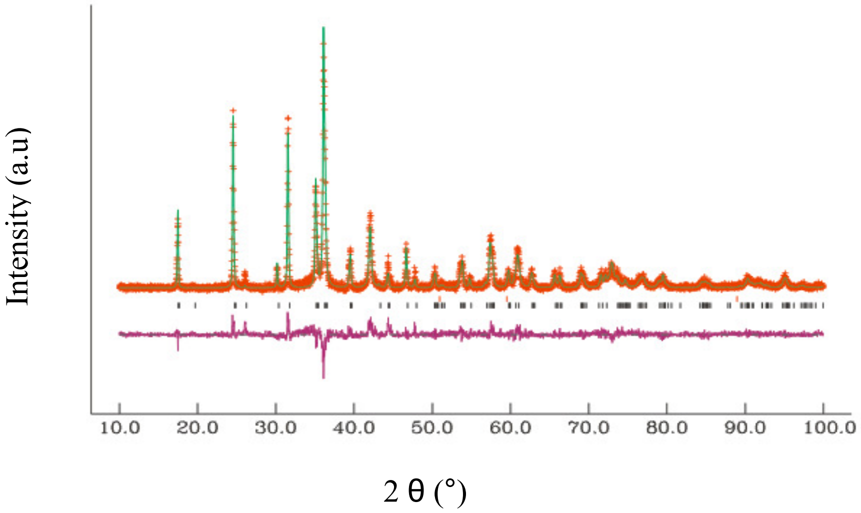

Fig. 3.7 Fit to the crystalline Ta_3N_5 and TaN dual phase sample obtained after reannealing amorphous TaN (initially obtained at 700 °C under ammonia) at 800 °C under N_2 for 1 hr in the TGA. Crosses mark the data points, upper continuous line the calculated profile and lower continuous line the difference. Lower tick marks are the positions of orthorhombic Ta_3N_5 reflections while the upper tick marks are the positions for cubic TaN.

Table 3.1 Lattice parameters of Ta_3N_5 after refining with GSAS and the crystallite size calculated from the GSAS L_x parameter using the Scherrer equation.[29] The sample temperature column shows the temperatures at which the samples were initially ammonolysed.

Sample temperature °C	a (Å)	b(Å)	c(Å)	Particle Size(nm)	Rwp/Rp%
Refined parameters for Ta_3N_5 obtained at 800 °C under ammonia					
800	3.896(33)	10.216(11)	10.284(9)	101	16.52/11.62
Refined parameters after 1hr annealing at 800 °C under nitrogen					
800	3.895(6)	10.180(19)	10.268(17)	61	18.86/13.82
700	3.896(28)	10.200(9)	10.272(8)	---	18.51/14.21
600	3.893(5)	10.202(14)	10.269(13)	42	18.74/14.61
500	3.896(4)	10.193(13)	10.272(11)	54	24.00/18.11

All three axes (a, b and c) were found to be close to the literature values[33], however the b axis shows slight variation in its behaviour, the reason might be the change in composition. It has been previously reported, [6] that the b-axis is more sensitive to composition and non-stoichiometry.

The changes after re-annealing at 800 °C under N_2 could be demonstrated as below:

$$\text{TaN}_x \text{ (amorphous)} \xrightarrow{800\ °\text{C},\ N_2} Ta_3N_5 + \text{TaN (cubic)} + N_2\uparrow$$

Formation of cubic TaN during conversion of amorphous TaN to Ta_3N_5 through further annealing could be avoided at this temperature by processing it under NH_3 atmosphere, as NH_3 has predominant nitriding character over its reducing character[34] and Ta_3N_5 is found to be stable even at 1000 °C in NH_3. Particle size of the samples after reannealing for one hour at higher temperature in the TGA had values in the range of ~ 40 to 65 nm, similar to that of Ta_3N_5 crystallised in ammonia at 800 °C.

Though carbon contamination in transition metal nitrides is an important consideration because it degrades electrical and optical properties and often causes adhesion problems,[35] the introduction of C can also increase hardness.[36, 37] Elemental analysis of a Ta_3N_5 sample obtained at 800 °C showed no carbon contamination. Small amounts of carbon were found in amorphous TaN obtained at 700 °C and below. It shows an average of 0.84%, while reannealing these samples for one hour under N_2 reduces the carbon to an average of 0.59% in the crystalline product. Nitrogen contents in the TaN system vary widely depending upon the experimental conditions. Analysis of the samples showed considerable differences and nitrogen rich compositions which might be the result of the large amount of ammonia reacted in the nitridation of the tantalum polymer, and could also be the larger amount reacted during solvolysis step. The nitrogen contents of Ta_3N_5 samples obtained were found 11.51% which is very close to theoretical value of 11.4% and were reduced to 10.72% after re-annealing the same sample at 800 °C for one hour under N_2, as the N_2 leaves the system at relatively high temperature.[13] All the other amorphous samples after reannealing had close to theoretical values for the nitrogen contents.

Table 3.2 The elemental analysis of the samples obtained by ammonolysis at different temperatures with and reannealing in the TGA under N_2 for one hour at 800 °C.

	Sample temp °C	Elemental Analysis before TGA (%)		Elemental Analysis after TGA (%)	
S/No	TaN_x	C	N	C	N
1	800	<0.10	11.51	<0.10	10.72
2	700	0.83	13.54	0.54	11.14
3	600	0.80	12.89	0.67	11.31
4	500	0..91	12.32	0.57	10.81

H <0.10 % throughout

The IR spectra obtained for the crystallised sample of Ta_3N_5 obtained at 800 °C is similar to that previously reported,[17] consisting of a series of shapes peaks between 400 and 1450 cm^{-1}. The spectrum for the samples obtained at 500 and 600 °C of amorphous TaN show the strong absorption peaks of ν (C≡N) at 2005 cm^{-1} due to pyrolysis of amide groups while a low intensity absorption peak is observed at 1997 cm^{-1} in the sample obtained at 700 °C. No such peak was observed in the sample heated at 800 °C or in the amorphous samples after re-annealing at 800 °C in the TGA. A broad absorption band at 3200 cm^{-1} could be attributed to ν (NH).[30] Spectra obtained for the samples after re-annealing the amorphous samples in the TGA were similar to the Ta_3N_5 spectra.

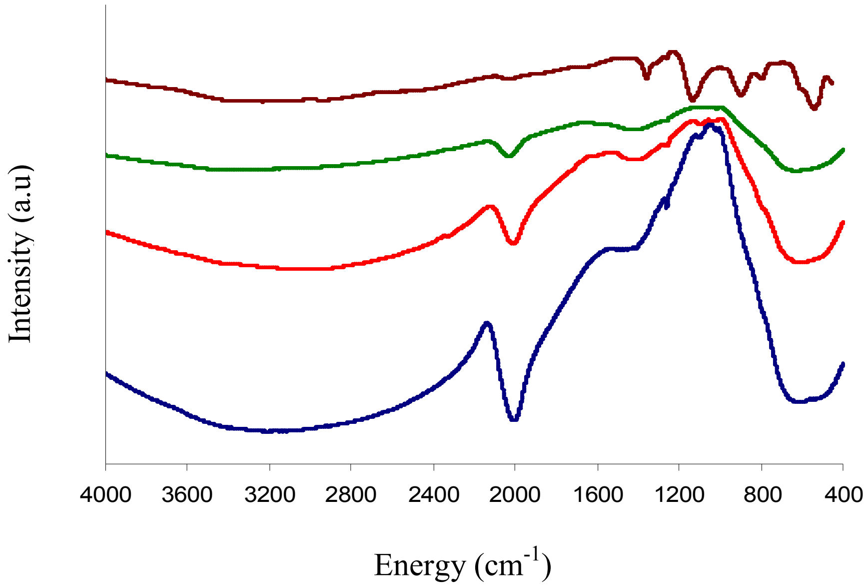

Fig. 3.10 IR spectra of Ta_xN_y samples heated in ammonia to 500 (bottom), 600, 700 and 800 °C (top)

TGA of the ammonolysed samples show very little mass loss at lower temperatures, which means that most of the amide precursor has been decomposed at all these annealing temperatures. The sample initially obtained at 500 °C shows some mass loss at 300 to 500 °C due to decomposition of NH_x groups and some NH_3 and N_2 loss. All the samples show mass loss at ~ 750 °C and at the holding temperature of 800 °C, which is attributed to N_2 removal and some carbon loss (presumably as hydrocarbon or amine), which was also observed in the elemental analysis.

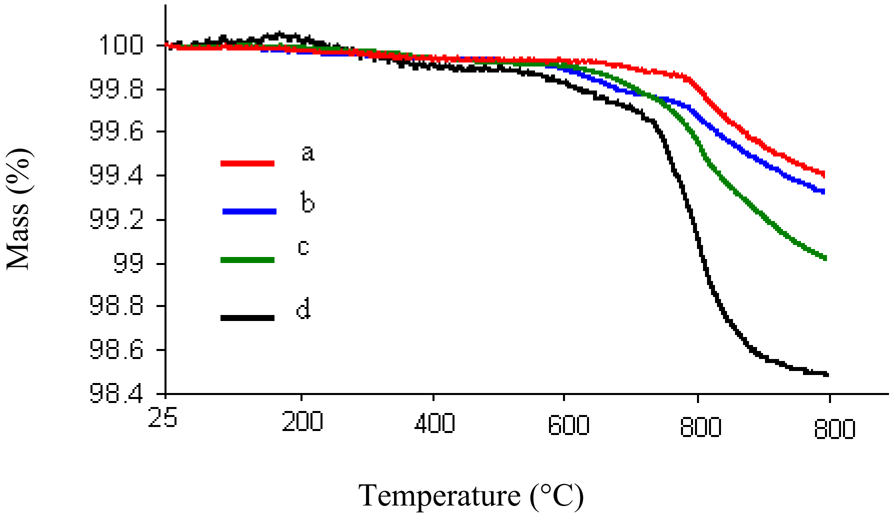

Fig. 3.10 TGA curves obtained for the samples heated in ammonia at 800 °C (a), 700 °C (b), 600 °C (c), 500 °C (d)

Figure 3.11 shows the UV-visible spectrum of the maroon Ta_3N_5 obtained at 800 °C, the absorption edge for Ta_3N_5 has been located at ~ 600 nm, as been reported for the red colour Ta_3N_5 films.[38] The measured band gap of 2.07 eV is similar to the literature value of 2.08 eV[1] for Ta_3N_5 obtained by heating Ta_2O_5 in ammonia.

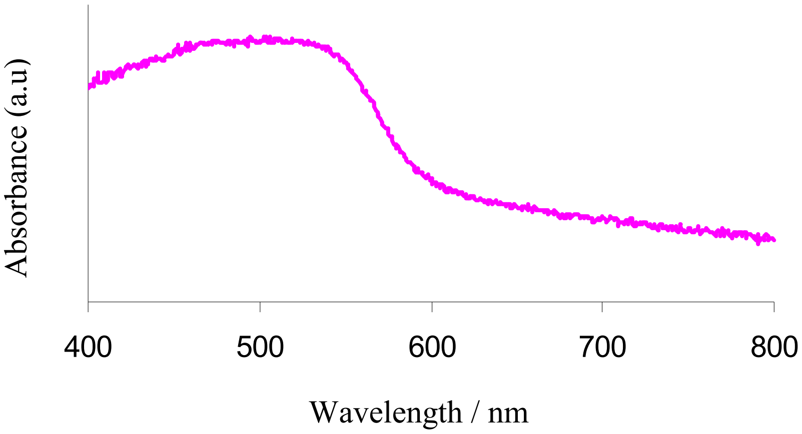

Fig. 3.11 UV-visible spectra for the Ta_3N_5 sample obtained at 800 °C

The EXAFS and FT-EXAFS data was refined using the iFEFFit software package. The background was subtracted with Athena and EXAFS was analysed with Artemis. The structure calculations were based on cif files obtained from ICSD.

Phase pure Ta_3N_5 was obtained at 800 °C and was fitted to the literature (crystallographic) structure. Ta_3N_5 contains two Ta sites with distorted octahedral TaN_6 environments, hence the first shell would be expected to contain 6 similar Ta-N distances. These were refined as a single average distance. Two Ta shells at larger distances were also refined with fixed coordination numbers. This refinement was used to obtain an amplitude reduction factor of 0.72 and this value was applied when fitting the EXAFS data for the amorphous phases.

The Fourier transformed EXAFS of the amorphous phases showed two shells at positions consistent with Ta-N and edge linked Ta-N-Ta. These were fitted using a variety of models based on rocksalt and hexagonal TaN without achieving good fits. The fits shown in Fig. 3. 11 use two shells from the Ta_3N_5 structure. The first shell has Ta-N distances consistent with octahedral Ta(V) and the coordination numbers are consistent with this at 500 and 600 °C. A drop in coordination number is observed at 700 °C, just before the structure reorganises with crystallisation. The Ta neighbours are found consistently at 3.2 Å, but the coordination numbers vary erratically and have large errors, they are considered to be of low reliability. The Debye-Weller factors and reliability factors have sensible values throughout.

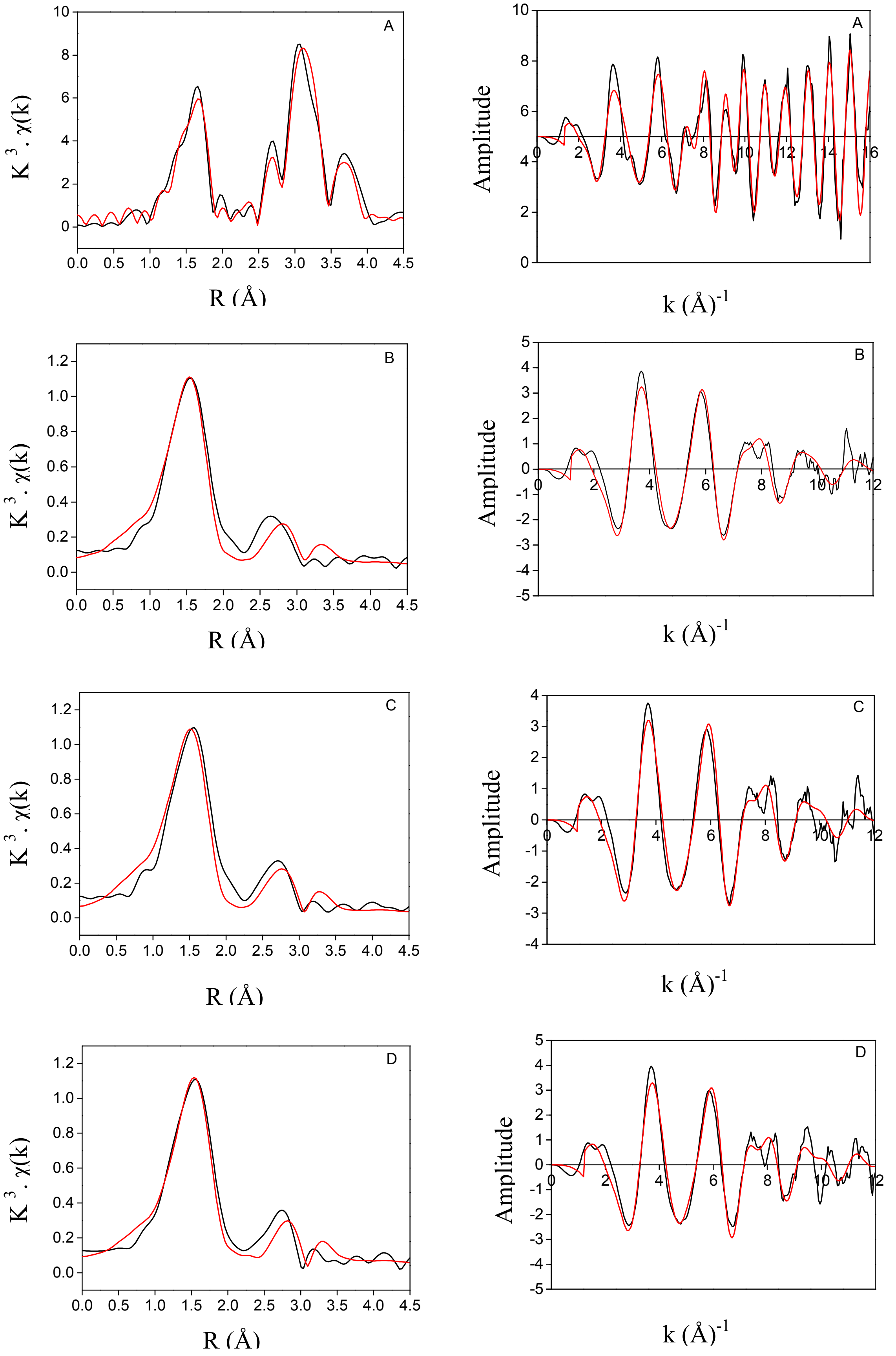

Fig. 3.11 Ta L_{III}-edge EXAFS and Fourier transformed EXAFS spectra of tantalum nitride samples heated in ammonia at 800 (A), 700(B), 600(C), and 500(D) °C.

Table 3.3 Analysis of tantalum L_{III}-edge EXAFS of tantalum nitrides using a structure model based on Ta_3N_5.

Temperature	**500 °C**	**600 °C**	**700 °C**	**800 °C**	
N Shell					
r/ Å	2.030(14)	2.024(7)	2.04(11)	2.026(97)	
ss/ Å	0.0114(3)	0.0115 (21)	0.0108(22)	0.0067(12)	
N	6.42(8)	6.4(6)	3.16(4)	6	
Ta shell (s)				Ta2	Ta1
r/ Å	3.19((14)	3.19(22)	3.21(31)	3.26(44)	3.76(10)
ss/ Å	0.0186(3)	0.0205(61)	0.0228(7)	0.0042(3)	0.0063(19)
N	8.488(43)	2.5(10)	5.6(24)	6	6
Red χ^2	926	437	933	61	
R	6.5	4.4	5.2	4.6	
E_0	5.73(11.7)	5.0(0)	5.4(9)	6.5(12)	

TEM images showed a homogeneous distribution of isotropic particles of ~15 to 50 nm in size. These particles were composed of agglomerates of small particles. Most of the particles were found to be spherical in shape.

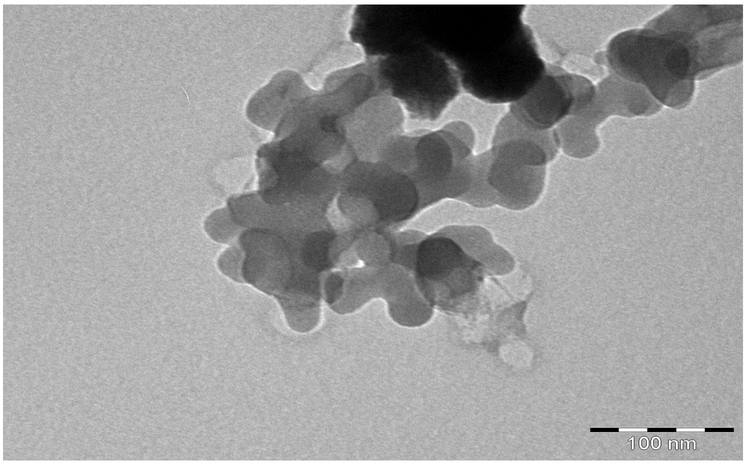

Fig. 3.12 TEM image of a TaN sample produced by ammonolysis at 500 °C

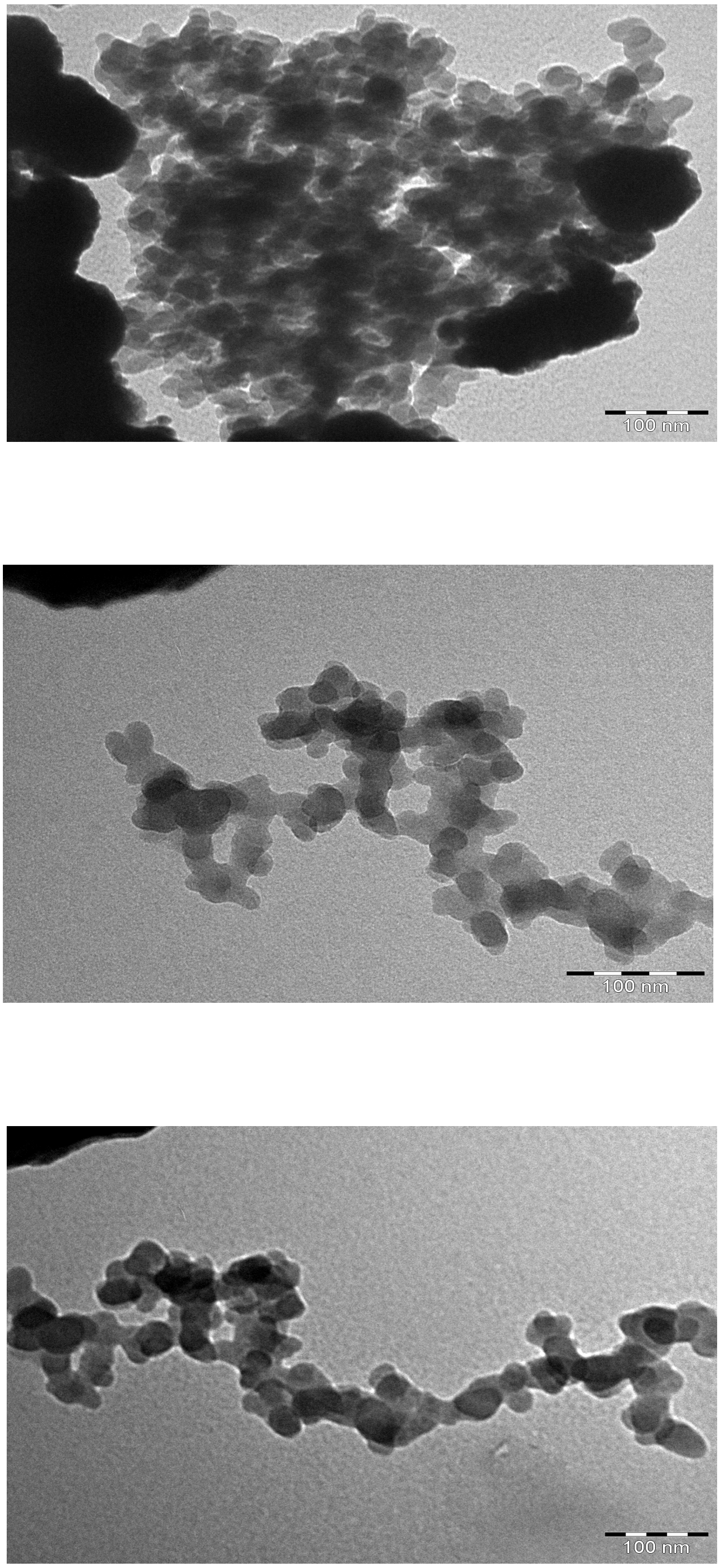

Fig. 3.13 TEM images of TaN samples produced by ammonolysis at 600 °C (top), 700 and 800 °C (bottom)

3.4 Conclusions

Solution phase ammonolysis of $Ta(NMe_2)_5$ followed by heating in ammonia results in amorphous samples of TaN at 500, 600 and 700 °C and crystalline Ta_3N_5 at 800 °C. Amorphous TaN obtained at 700 °C and below was found to be transformed to Ta_3N_5 with some cubic TaN when re-annealed at 800 °C under nitrogen in the TGA furnace. The sample of Ta_3N_5 obtained by ammonolysis at 800 °C was found to be stable even after re-annealing at 800 °C for 1 hour under nitrogen. All the Ta_3N_5 samples obtained from re-annealing amorphous TaN showed N_2 contents close to that of Ta_3N_5. Crystal parameters were also found to be consistent with the reported values[33] with a slight variation in the b axes length. Samples were nanocrystalline but heavily aggregated.

3.5 References

1. C. M. Fang, E. Orhan, G. A. De-Wijs, H. T. Hintzen, R. A. De-Groot, R. Marchand, J. Y. Saillard and G. J. De-With, *J. Mater. Chem.*, 2001, **11**, 1248.
2. G. Hitoki, A. Ishikawa, T. Takata, J. N. Kondo, H. Hobayashi and K. Domen, *Chem. Lett.*, 2003, **7**, 736.
3. M. Hara, G. Hitoki, T. Takata, N. J. Kondo, H. Kobayashi and K. Domen, *Catal. Today*, 2003, **78**, 555.
4. K. J. Lee and H. S. Yang, Japanese Patent 2001237399, 2001.
5. I.-S. Park, S.-Y. Park, G.-H. Jeong, S.-M. Na and S.-J. Suh, *Thin Solid Films*, 2008, **516**, 5409.
6. T. Akashi, H. Takemri, T. Tomobe and S. Koizumi, *Jpn. Soc. Precis. Eng.*, 2002, **66**, 1052.
7. C. Michaluk, *J. Electron. Mater.*, 2002, **31**, 2.
8. I. Ayerdi, E. Castano, A. Garcia-Alonso and J. Gracia, *Sensors Actuators*, 1997, **60**, 72.
9. Y. X. Leng, H. Sun, P. Yang, J. Y. Chen, J. Wang, G. J. Wan, N. Huang, X. B. Tian, L. P. Wang and P. K. Chu, *Thin Solid Films*, 2001, **398-399**, 471.
10. A. Arranz and C. Palacio, *Appl. Phys.* , 2005, **81**, 1405.
11. M. Stavrev, D. Fischer, C. Wenzel, K. Drescher and N. Mattern, *Thin Solid Films*, 1997, **307**, 79.
12. C.Stampfl and A. J. Freeman, *Phys. Rev. B*, 2005, **71**, 024111.
13. N.Terao, *Jap. J. Appl. Phys.* , 1971, **10**, 248.
14. W. Lei, D. Liu, X. Li, J. Zhang, Q. Zhou, J. Hu, Q. Cui and G. Zou, *J. Phy: Condens. Matter.*, 2007, **19**, 425233.
15. P. F. McMillan, O. Shebanova, D. Daisenberger, R. Q. Cabrera, E. Bailey, A. L. Hector, V. Lees, D. Machon, A. Sella and M. Wilson, *Phase Trans.*, 2007, **80**, 1003
16. P. Kroll, T. Schröter and M. Peters, *Angew. Chem. Int. Ed.*, 2005, **44**, 4249.
17. B. Mazumder and A. L. Hector, *J. Mater. Chem.*, 2008, **18**, 1392.
18. B. Mazumder, P. Chirico and A. L. Hector, *Inorg. Chem.*, 2008, **47**, 9684.
19. S. J. Henderson and A. L. Hector, *J. Solid State Chem.*, 2006, **179**, 3518.
20. A. L. Hector and I. P. Parkin, *Chem. Mater.*, 1995, **7**, 1728.

21. J. C. Fitzmaurice, A. L. Hector and I. P. Parkin, *J. Chem. Soc., Dalton Trans.*, 1993, 2435.

22. L. Shi, Z. Yang., L. Chen and Y. Qian, *Solid State Commun.*, 2005, **133**, 117.

23. I. P. Parkin and A. T. Rowley, *J. Mater. Chem.*, 1995, **5**, 909.

24. K. Hieber, *Thin Solid Films*, 1974, **24**, 157.

25. M. D. Hoffman, *Polyhedron*, 1994, **13**, 1169.

26. R. Fix, G. R. Gordon and M. D. Hoffman, *Chem. Mater.*, 1993, **5**, 614.

27. M. Ritala, P. Kalsi, D. Riihela, K. Kukli, M. Leskela and J. Jokinen, *Chem. Mater.*, 1999, **11**, 1712.

28. R. B. Von-Dreele and A. C. Larson, Generallized structure analysis system, Los Alamos National Laboratory, NM87545, USA, December 2002 release.

29. R. B. Von-Dreele and A. C. Larson, GSAS Manual, LANSCE MS-H805, Los Alamos National Laboratory, Los Alamos NM, NM 87545, 2000.

30. M. H. Chisholm, D. V. Baxter, G. J. Gama, V. F. DiStasi, A. L. Hector and I. P. Parkin, *Chem. Mater.*, 1996, **8**, 1222.

31. K. Nakamoto, *Infrared and Raman Spectra of Inorganic and Organic Coumpunds* 3rd ed.; J. Wiley: New York, 1978.

32. N. E. Brese, M. O. Keeffe, P. Rauch and F. J. DiSalvo, *Acta Crystallogr.* , 1991, **47**, 2291.

33. B. Fu and L. Gao, *J. Amer. Ceram. Soc.*, 2005, **88**, 3519.

34. Q. Zhang and L. Gao, *Langmuir*, 2004, **20**, 9821

35. D. M. Hoffman, *Polyhedron*, 1994, **13**, 1169

36. B. Mazumder and A. L. Hector, *Top. Catal.*, 2009, **52**, 1472.

37. H. J. Holleck, *Vac. Sci. Technol.*, 1986, **A 4**, 1384.

38. X. Feng, T. J. LaTempa, I. J. Basham, K. G. Mor, O. K. Varghese and C. A. Grimes, *Nano Lett.*, 2010, **10**, 948.

4. Molybdenum nitrides from ammonolysis of $MoCl_5$

4.1 Introduction

Interest in molybdenum nitride stems from applications in catalysis,[1] its magnetic behaviour,[2] superconductivity[3, 4] potential use as diffusion barrier films microelectronic devices,[5] and its excellent corrosion resistance including to boiling sulfuric acid.[6] Hard wear-resistance coatings,[7, 8] potentially useful on machine tools, have been formed from molybdenum nitride. The major interest has been in its unique heterogeneous catalytic properties (similar to group VIII metals) in many hydrogen involving reactions. Molybdenum nitrides exhibit good catalytic activities for hydrodesulfurization (HDS)[9-13] and hydrodenitrogenation (HDN)[14-17]reactions, carbon monoxide hydrogenation, ammonia synthesis, and ethane hydrogenolysis[18] and might offer a cost-effective alternative to existing catalysts.[17]

Molybdenum forms a variety of nitrogen-containing compounds MoN_x with x ranging from 0 to at least 1. Within the Mo-N system, known phases include the stoichiometric hexagonal compound δ-MoN and non-stoichiometric cubic phases γ-MoN_x ($x \sim 0.5$) and γ-Mo_2N.[19-22] Phase diagram studies of the Mo-N system show only the hexagonal δ-MoN exists at the stoichiometric composition.[23] A cubic high-temperature modification γ-MoN_x of NaCl-type structure is present at lower N concentration ($x = 0.61$ to 0.75).[24,25]

MoN was first synthesised in 1930 by nitridation of molybdenum powder in an ammonia atmosphere at 700-1000 K.[26] Molybdenum nitride samples of hexagonal and cubic structure were prepared at pressures up to 7 GPa and temperatures up to 2300 K using molybdenum powder and 25 μm thick molybdenum foil.[27] The starting material was put into a BN (hexagonal structure) container with a graphite heater, and the reaction carried out in a pyrophylite cylinder with tantalum AC contacts on the top and bottom of the cylinder. Surface analysis of the samples showed boron and carbon from the reaction container. These impurities could influence the electrical properties of the sample.

Thin films of molybdenum nitride have been reported via CVD by ammonia nitridation of $MoCl_5$ and $Mo(CO)_6$ diluted in N_2 or Ar using a cold-wall, vertical pancake-style reactor. NH_3 nitridation of $MoCl_5$ produced thin films of mixed phase δ-MoN and γ-Mo_2N, with δ-MoN more favoured at high temperature and high flow of NH_3.[28] The MoN films were only obtained using $Mo(CO)_6$ below 500 and above 700 °C, while mixtures of Mo_2N and MoN were obtained through both the precursors at all other temperatures except Mo_2N at 400-450 °C through $MoCl_5$. The MoN obtained through $Mo(CO)_6$ contained a high level of carbon. Plasma-assisted CVD molybdenum nitride at high temperature from $MoCl_5$ and NH_3 has also been reported.[29] Other molybdenum nitride film preparation methods include the direct nitridation of molybdenum layers with NH_3[30] and techniques such as molecular beam epitaxy,[31, 32] ALD[33, 34] and reactive sputter deposition.[35]

Recently Hector and co-workers[36] reported nanoparticles of molybdenum nitrides via solvothermal synthesis using $MoCl_5$ with $LiNH_2$ or NH_3 as the nitriding source. Amorphous molybdenum nitride was obtained after 24 hours heating at 450 °C, while rock salt cubic MoN was obtained after 24 hours heating at 550 °C. Benzene was used as a solvent. Lattice parameters were a = 4.106(4) Å using $LiNH_2$ or a = 4.095(8) Å with NH_3. The products so obtained have significant carbon content due to solvent decomposition.

Wang[29] and co-workers used a flow of NH_3/N_2 mixture over $MoCl_5$ powder in an alumina boat with a silica tube to produce molybdenum nitrides. With pure NH_3 as the nitriding source, as amorphous MoN_{1-x} and NH_4Cl was obtained mixture at 400 °C with poorly crystallized product up to 500 °C, the hexagonal δ-MoN was obtained up to 600 °C. A mixture of δ-MoN and γ-Mo_2N was obtained up to 700 °C and cubic γ-Mo_2N at 800 °C. Low concentrations of ammonia favoured the formation of γ-Mo_2N at low temperature. The product obtained at 600 °C contained 2-7 wt% oxygen. The same authors used a solvothermal route with ammonia or hydrazine as solvent with $MoCl_5$ to obtain γ-Mo_2N.[29] The $MoCl_5$ was contained in a gold tube placed in the reaction the vessel of nickel-based alloy which was able to withstand 500 MPa. The solvent was introduced and the vessel was heated in the furnace. Since the reaction was carried out in a closed reaction vessel, the NH_4Cl by-product was systematically found mixed with the nitride phases.

Lenguer[37] used the same precursor in a related study. $MoCl_5$ was heated under flow of ammonia in a mullite tube at temperatures of 770-1060 K. WC-type δ-MoN with lattice parameters of a = 0.2851 (2) nm and c = 0.2782(3) nm was obtained. At 950 K, a mixture of δ-MoN and γ-Mo_2N_{1-x} was obtained, with the γ-phase content increasing with temperature. Lattice parameters of γ-Mo_2N_{1-x} were to be found temperature dependent and decreased from a = 0.4188(1) nm at 970 K to a = 0.4170(1) nm at 1060 K, whereas the δ-MoN were not changed. At 1060 K δ3-Mo_2N was observed with lattice parameters of a = 0.5740(2) nm and c = 0.5624(3) nm, which are significantly larger than the doubled cell parameters of the WC-type MoN. Spherical particles were observed due to melting of $MoCl_5$ before the reaction to δ-MoN was complete, which also causes agglomeration of the product particles and enlarges the particle size.

In the current study we reacted $MoCl_5$ with ammonia in solution and then heated in ammonia, to maximise chloride removal and minimise opportunities for particle growth. $MoCl_5$ was dissolved in hexane and sodium dried liquid ammonia was condensed in to the solution at -78 °C. Solution phase ammonolysis produced a black powder, which was then dried under vacuum to remove solvent and collected in the glove box. The ammonolysed precursor was then heated in a tube furnace under a flow of NH_3 for further nitridation at various temperatures. Solution phase ammonolysis prevents the melting of $MoCl_5$ during the reaction if heated directly[37] and careful handling can prevent hydrolysis, which would result in oxygen contamination of the final product.[29]

4.2 Experimental Section

4.2.1 Ammonolysis of $MoCl_5$

Ammonolysis of $MoCl_5$ was carried out using a Schlenk line. $MoCl_5$ (2g) was dissolved in dry n-hexane (20 ml) and was stirred for 2 hrs to ensure dissolution. 20 ml liquid NH_3 (dried over sodium) was condensed into the $MoCl_5$ solution at -78 °C with continuous stirring. A bright yellow precipitate appeared as ammonia started condensing into the solution. The mixture was left to warm to room temperature under N_2 as the excess ammonia evaporated. The yellow precipitate turned dark brown and finally to a fluffy black powder while evaporating the NH_3. The black precipitate of molybdenum amide polymer ~2.5 g was then filtered, dried under vacuum and transferred to the glove box.

The likely reaction is given below:

$$MoCl_5 + NH_3 \xrightarrow[-78\ °C]{n\text{-hexane}} Mo(NH_2)_x(NH)_y(Cl)_z + (5-z)NH_4Cl$$

4.2.2 Pyrolysis of the molybdenum chloroamide precursor

1 g of the black molybdenum chloroamide polymer was transferred to a ceramic boat inside a silica tube, which was loaded inside the glove box. The silica tube was provided with an arrangement of taps to allow flushing of the hoses before the samples were exposed to the gas flow (Fig.4.1). Samples were then heated under flowing ammonia to 500, 600, 700, 800, 900, or 1000 °C for 2 hrs. Polymer samples were also heated at 500 °C for longer durations of 12, 24 or 48 hrs. A column of molecular sieves was used to dry the ammonia. An average of 0.35 g of molybdenum nitride was obtained after annealing 1g of the polymer. The ammonium chloride formed during ammonolysis sublimes out at 340 to 360 °C during annealing and sublimes on the inner cold walls of the furnace tube. Contamination of the MoN_x product with ammonium chloride was prevented by placing a roll of aluminium foil inside the furnace tube such that the ammonium chloride condensation occurs on it. It is then removed before taking out the boat containing the nitride sample. The pyrolysis could be described as:

$$Mo(NH_2)_x(NH)_y(Cl)_z \xrightarrow[NH_3]{\triangle} MoN_a + zNH_4Cl + b\ NH_3 + cN_2$$

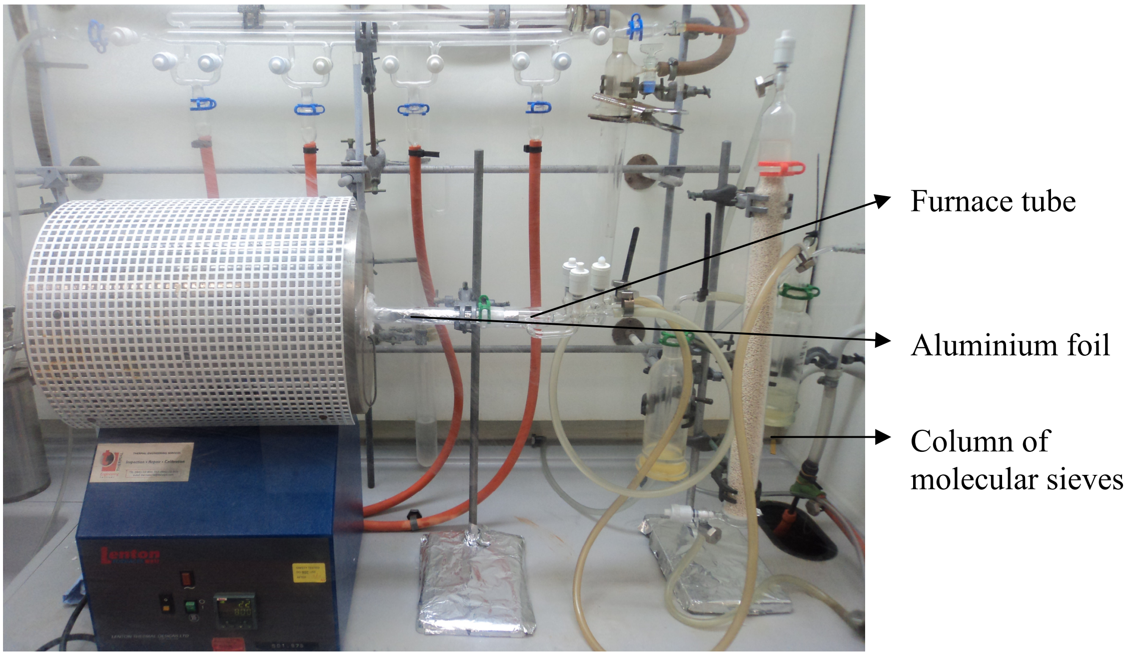

Fig. 4.1 Arrangement of the apparatus used for the pyrolysis of the polymeric molybdenum chloroamide precursors

4.2.3 Measurements

PXD patterns were collected with a Siemens D5000 diffractometer using a sample holder for air sensitive materials. TGA was carried out using a Mettler Toledo TGA/SDTA85le under flowing BiP nitrogen with flow rate of 50 ml/min and temperature ramp rate of 10 °C/min. The temperature was raised from 25 to 800 °C and was held at maximum temperature for 20 minutes. TEM was performed on a Hitachi H7000 with accelerating voltage of 75 kV. Samples were made by ultrasound dispersal using dry toluene as the solvent and were deposited on carbon coated Cu grid. Infrared spectroscopy was performed on CsI disks using a Perkin Elmer Spectrum One FT-IR spectrometer. The PXD data was refined using GSAS[38] with standard parameters from ICSD. Crystallite sizes were obtained using the method described in the GSAS manual.[39] Samples were sent for C, H and N analysis to Medac Ltd.

4.3 Results and discussions

4.3.1 Analysis of the polymeric molybdenum chloroamide precursor

Elemental analysis of the polymeric precursor of molybdenum amide showed high levels of chlorine, hydrogen and nitrogen as about 70% of the precursor is composed of NH_4Cl.

Table. 4.1 Elemental analysis of polymeric precursor

Elemental Analysis				
Elements	C	H	N	Cl
Mass%	0.91	5.35	21.67	41.27

The IR spectrum (Fig. 4.2) shows strong absorptions at 3150 cm^{-1} (ν (NH)),[40] 3048 and 2826 cm^{-1} (ν (C-H)), 1407 and 1298 cm^{-1} (ν (C-N)), 1599 cm^{-1} (δ (NH_2)).[40, 41] The spectrum is consistent with a mixture of the molybdenum chloroamide polymer and NH_4Cl.

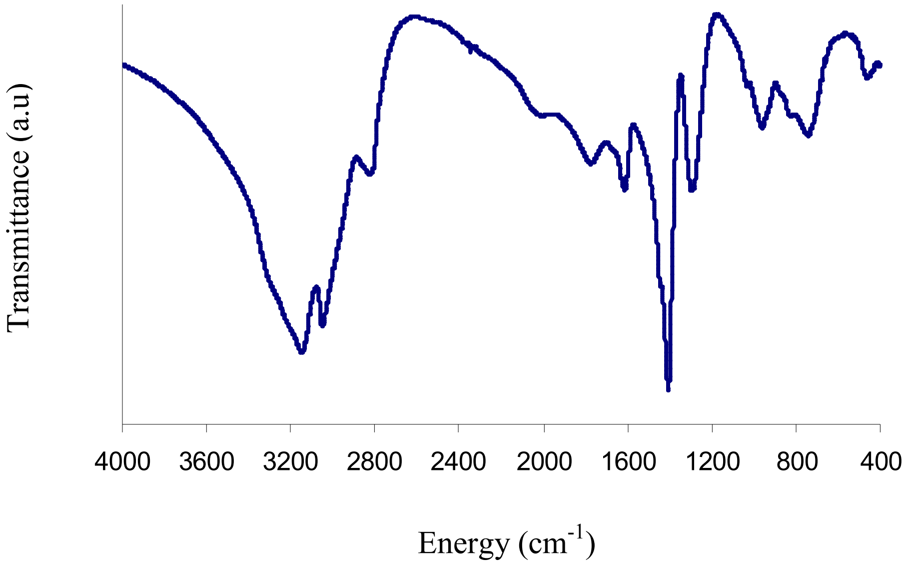

Fig. 4.2 IR spectrum for the polymeric precursor

TGA of the polymeric precursor (Fig. 4.3) shows two step mass losses. The total mass loss is 74% of the precursor mixture when heated to 800 °C under nitrogen. The major mass loss is observed at 200 to 400 °C, which corresponds to the loss of NH_4Cl. Further mass losses are due to loss of NH_3 and further NH_4Cl as the condensation reactions proceed, and of N_2 loss due to molybdenum reduction above 700 °C.[40]

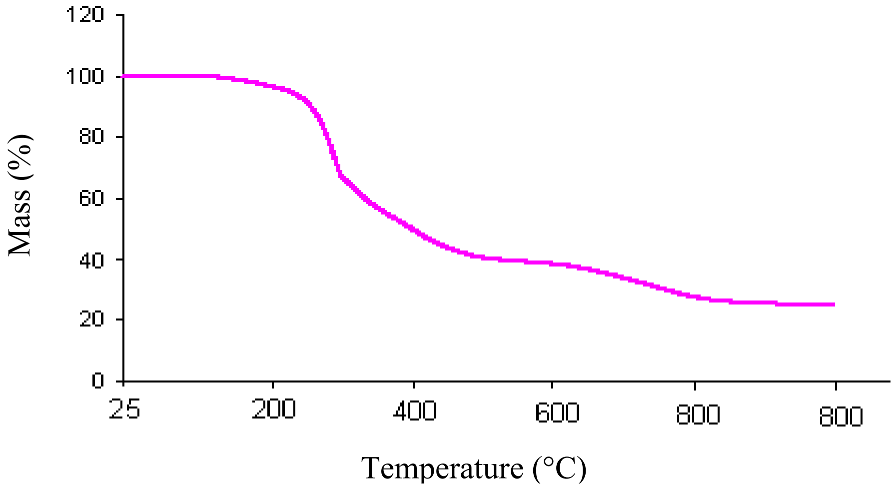

Fig. 4.3 TGA curve for the polymeric molybdenum chloroamide precursor

4.3.2 Analysis of pyrolysed molybdenum nitride samples

PXD (Fig.4.4 and 4.5) showed that samples of rock salt (cubic) and hexagonal MoN_x were prepared by solution phase ammonolysis of $MoCl_5$ followed by annealing the samples at various temperatures for two hours under ammonia. The precursor obtained by ammonolysis was used directly for annealing and was not preheated for the removal of NH_4Cl as in related work.[29] No peaks for ammonium chloride were found in the PXD patterns. Phase pure cubic MoN_x was obtained in the higher temperature range of 700 to 1000 °C, while mixtures of cubic and hexagonal MoN_x were obtained at 600 °C. Phase pure hexagonal MoN_x was obtained at 500 °C for 12, 24 and 48 hrs, while amorphous material with broad humps in the PXD pattern that resemble hexagonal MoN_x was obtained when heating the polymer at 500 °C for 2 hrs. Reflections at 40 and 41° 2θ in the samples heated at 900 and 1000 °C correspond to molybdenum metal,[42] due to N_2 loss at higher temperature, which is also observed in the TGA.

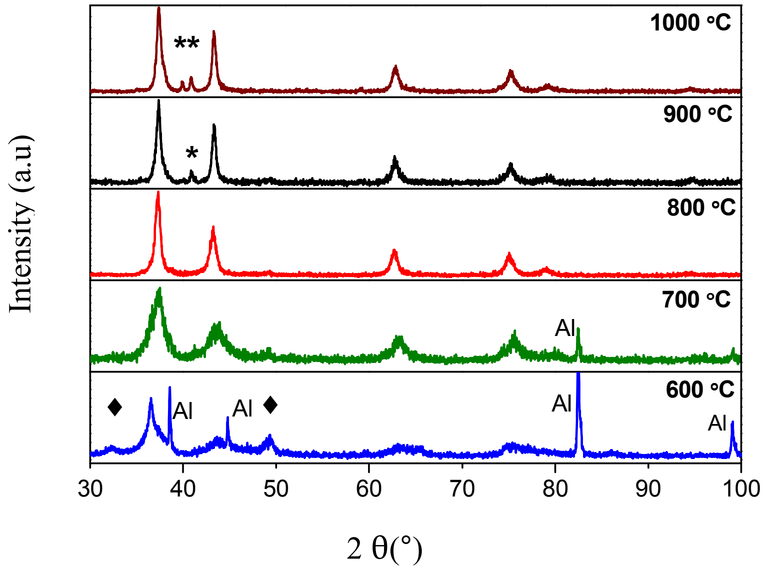

Fig.4.4 PXD patterns obtained for samples annealed at the temperatures given in the figure. (♦) symbols indicate the hexagonal MoN_x reflections, (Al) represents aluminium peaks resulting from the sample holder and (*) shows the reflections for Mo metal. Remaining peaks are due to cubic (rocksalt) MoN_x.

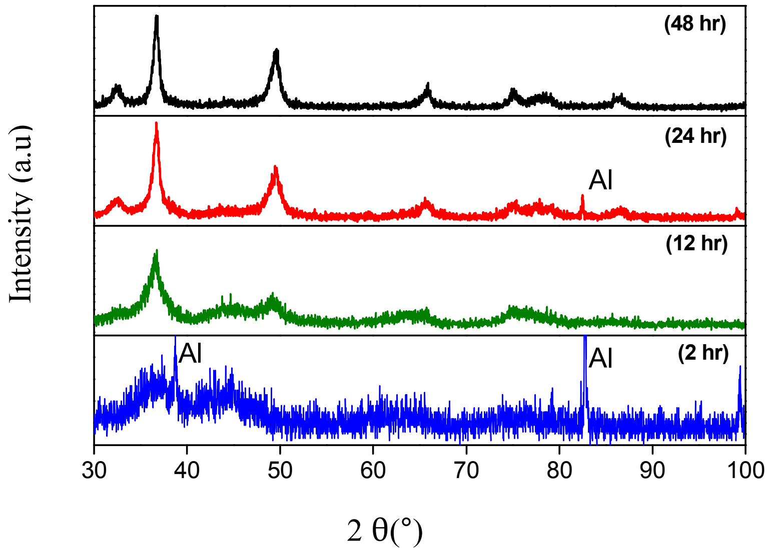

Fig.4.5 PXD patterns for hexagonal MoN_x samples heated at 500 °C for the durations shown in the figure. (Al) represent the aluminium peaks resulting from the sample holder.

Rietveld refinements were carried out on all phases that produced peaks well enough defined to do so. Fig.4.6 and 4.7 show two examples of phase fit and table 4.2 lists the refined lattice parameters.

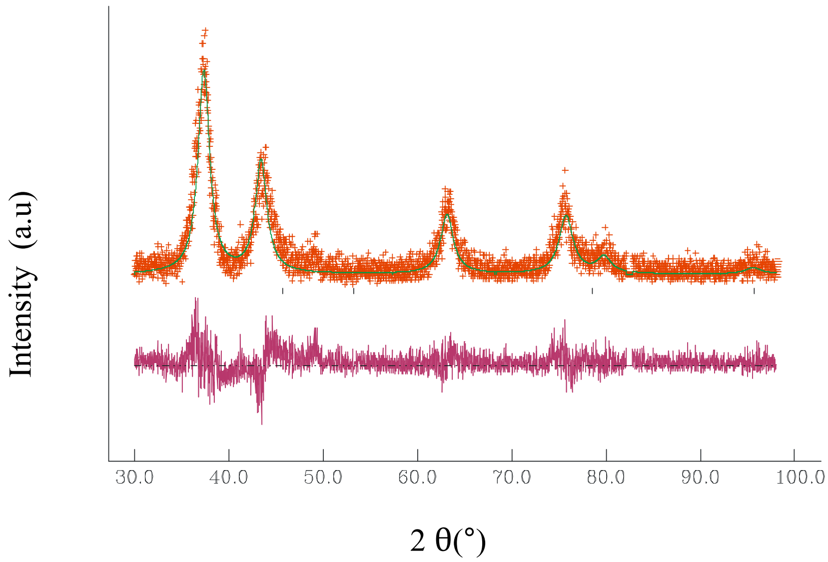

Fig. 4.6 Fit to the crystalline cubic MoN obtained after annealing the polymer at 800 °C. Crosses marks the data points, upper continuous line the calculated profile and lower continuous line the difference, tick marks are the positions of standard reflection positions for cubic MoN.

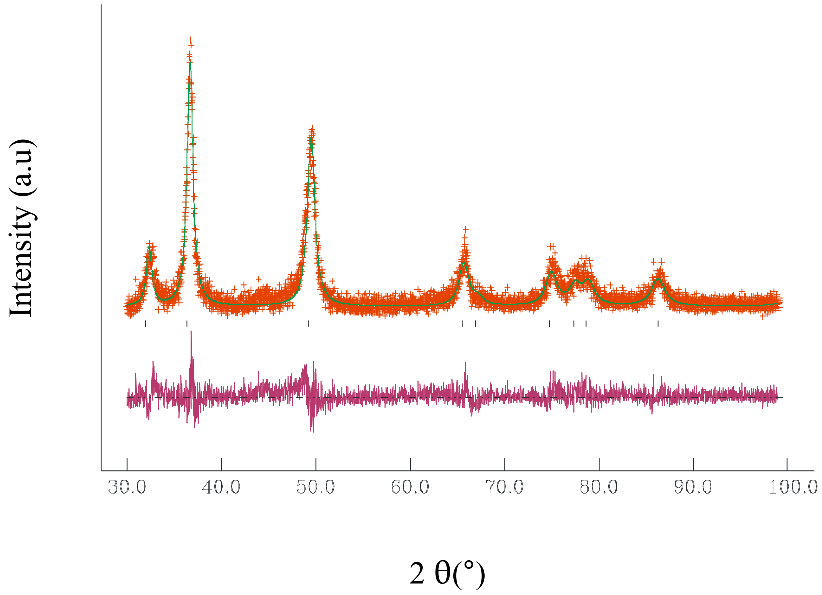

Fig. 4.7 Fit to the hexagonal MoN obtained after annealing the polymer at 500 °C for 48 hr. Crosses mark the data points, upper continuous line the calculated profile and lower continuous line the difference, tick marks are the positions of standard reflection positions for hexagonal MoN.

Table 4.2 Lattice parameters of cubic and hexagonal molybdenum nitride samples

Sample temperature °C	Heating Time	a (Å)	b(Å)	c(Å)	Particle size	Rwp/Rp%
1000	2hr	4.1962(8)			22	25.72/19.01
900	2hr	4.2014(10)			16	24.80/20.83
800	2hr	4.2045(8)			20	23.52/17.07
700	2hr	4.1551(24)			22	33.60/22.52
500	48hr	2.8530(9)	2.8530(9)	2.7955(11)	32	24.15/18.68
500	24hr	2.8536(14)	2.8536(14)	2.7974(16)	10	24.19/18.39

Lattice parameters of cubic MoN vary from 4.16 Å[21] to 4.22 Å.[27] The sample obtained at 1000 °C showed a slight reduction in its lattice parameter compared with 800 or 900 °C, it could be due to N deficient as it was heated at a higher temperature. The lattice parameter for the sample obtained at 700 °C is much lower. Refined lattice parameters for the hexagonal phase obtained at 500 °C annealed for 24 and 48 hrs are close to those given in the literature[25, 37] for hexagonal (WC-type) MoN of a = 2.8 and c=2.7Å.[25, 37]

Carbon contamination in transition metal nitrides is an important consideration because it degrades electrical and optical properties and often causes adhesion problems[43]. Elemental analysis of all the nitride samples after ammonolysis of the polymeric precursors at different temperatures (Table 4.3) showed them to be carbon free. Small quantities of chlorine were observed in the samples obtained at 500 °C, even those heated for longer periods, however EDX analysis showed no contamination by chlorine in the samples obtained at 600 °C and above. The samples obtained at 500 °C were found to be nitrogen rich, while the samples of rock salt MoN obtained at 700 °C and above were nitrogen deficient. Rock salt MoN has previously been found to have a tendency to be N deficient.[36]

Table 4.3 Elemental analysis of MoN samples obtained at various temperatures

Sample temperature °C	%N	%Cl	Elemental Composition
500	13.82	2.42	$MoN_{1.13}Cl_{0.08}$
500 (12 hr)	12.78	2.87	$MoN_{1.02}Cl_{0.08}$
500 (24 hr)	13.21	1.17	$MoN_{1.06}Cl_{0.03}$
500 (48 hr)	13.52	1.72	$MoN_{1.08}Cl_{0.05}$
600	12.71	0	MoN
700	9.93	0	$MoN_{0.71}$
800	9.01	0	$MoN_{0.64}$
900	8.67	0	$MoN_{0.62}$
1000	8.74	0	$MoN_{0.62}$

%C and %H <0.10 throughout. Stoichiometric MoN contains 12.73 %N.

The IR spectrum (Fig.4.8 and 4.9) show the low intensity absorption peaks at 3430-3450 cm^{-1} which corresponds to residual ν (NH).[40] weak peaks at 1580- 1610 cm^{-1} in the samples annealed at 600 to 1000 °C, and in the samples annealed at 500 °C for shorter times, could be attributed to δ (NH_2).[40, 41] No such a peak was observed in the samples obtained at 500 °C for 24 and 48 hrs. The broad absorption band observed in all samples at ~ 1000 cm^{-1} is attributed to ν (M-N). A series of sharp peaks is also observed in the samples heated at 500 °C for the shorter time periods, showing the structure development is incomplete.

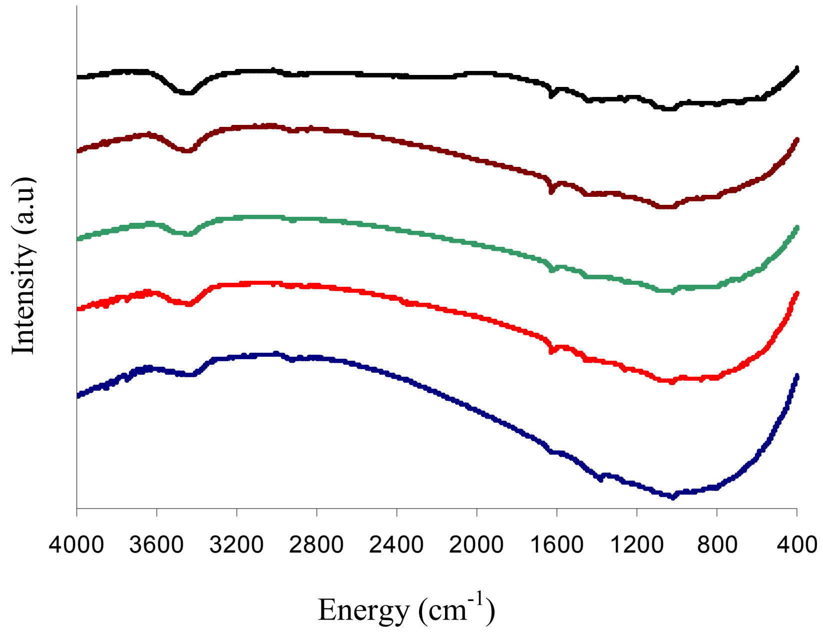

Fig. 4.8 IR spectrum for the MoN$_x$ samples at various temperatures annealed for 2 hrs under ammonia, 600 °C (bottom), 700 °C, 800 °C, 900 °C and 1000 °C (top)

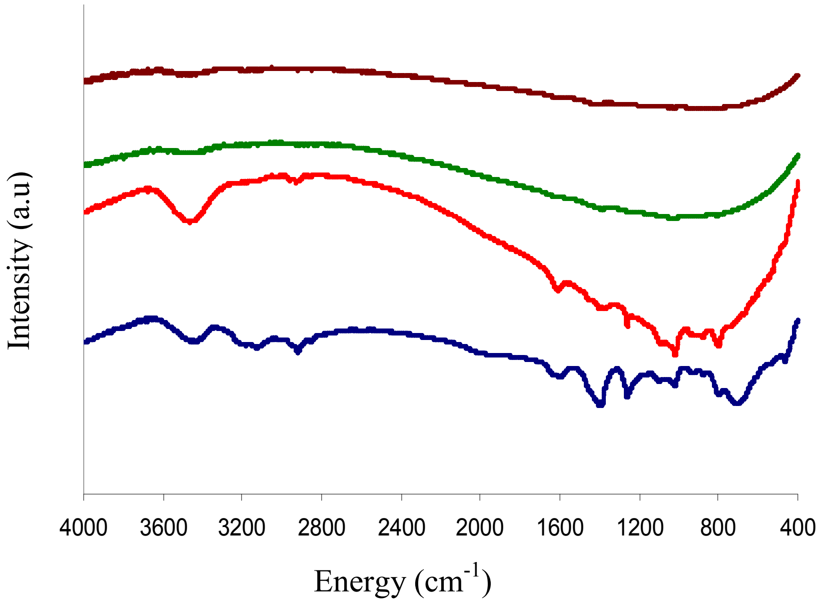

Fig. 4.9 IR spectrum for the MoN$_x$ samples at 500 °C annealed under ammonia for, 2 hrs (bottom) 12 hrs, 24 hrs and 48 hrs (top)

All the pyrolysed metal nitride samples were also studied by TGA (Fig. 4.10 and 4.11). The analysis showed two step mass losses. During the first step at lower temperature (0-400 °C) the mass loss corresponds to amide group elimination as ammonia leaves the system. Above 700 °C nitrogen is lost.[40] The mass loss at lower temperature was greater in the samples obtained at 500 °C due to presence of amide groups in the samples; however the samples heated at the same temperature for longer duration showed reduced loss of amide groups. As the sample anneals and crystallises the NH_2 and NH groups are lost, so more of the sample is present as metal nitride.

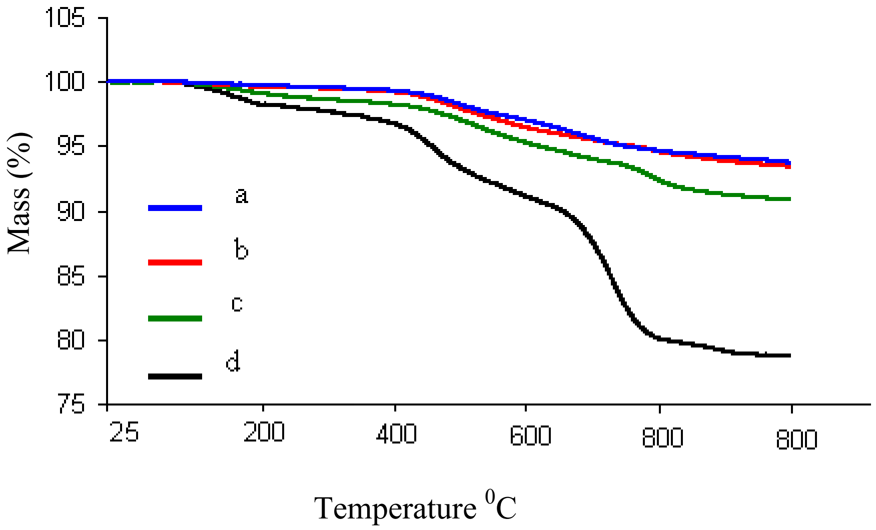

Fig. 4.10 TGA curves for the samples of MoN_x produced at 500 °C for 48 hrs (a), 24 hrs (b), 12 hrs (c) and 2 hrs (d)

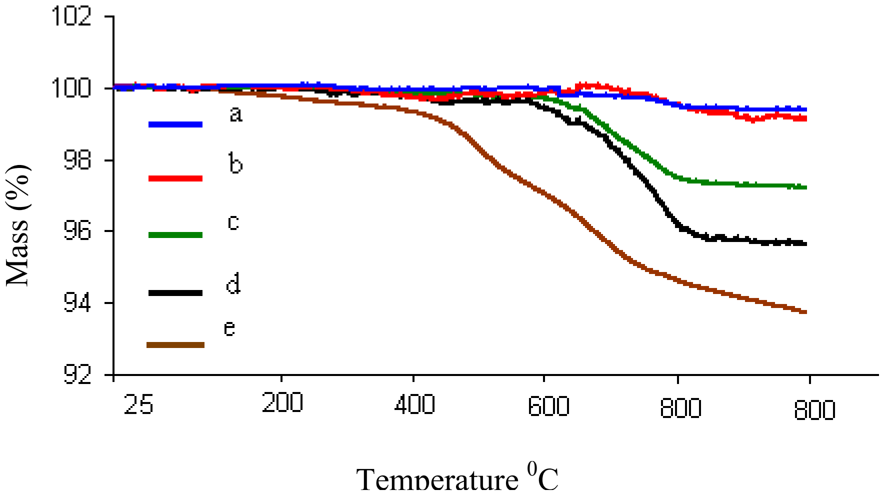

Fig. 4.11 TGA curves for the samples of MoN_x produced at, 1000 °C (a), 900 °C (b), c (800 °C), 700 °C (d) and 600 °C (e)

TEM images show spherical particles with size of ~10 to 50 nm, which is consistent with values obtained using the Scherrer equation[39] based on refined PXD patterns. The agglomeration of particles was observed in most of the samples heated at high temperature.

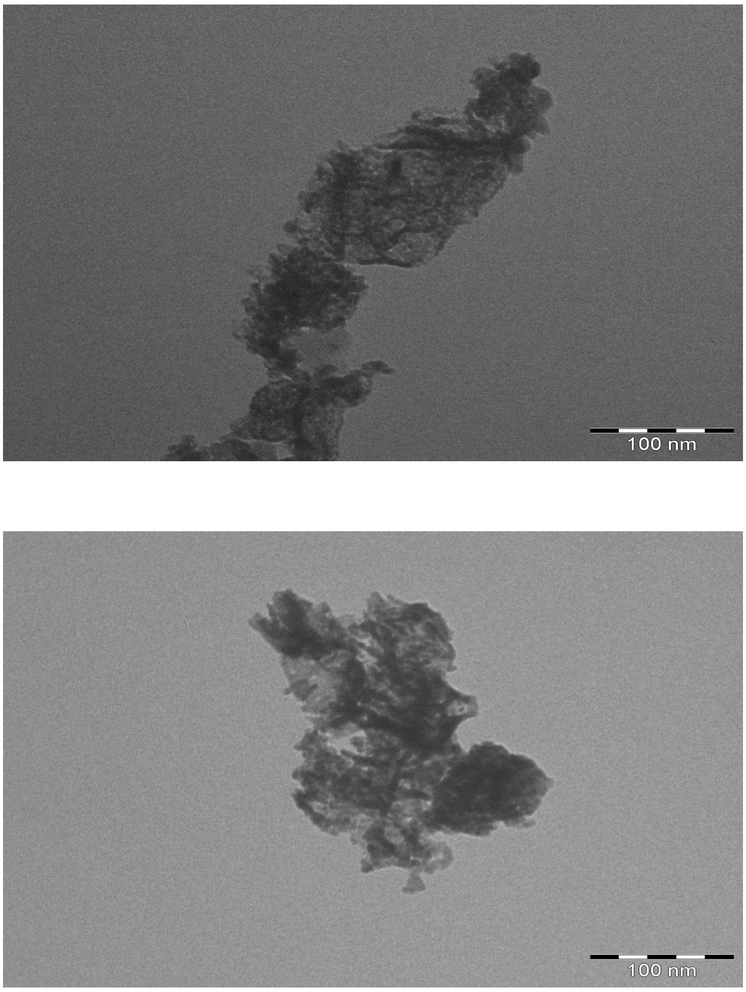

Fig.4.12 TEM images for MoN_x samples heated at 500 °C (for 2 hrs) (top) and 600°C (for 2 hrs) (bottom)

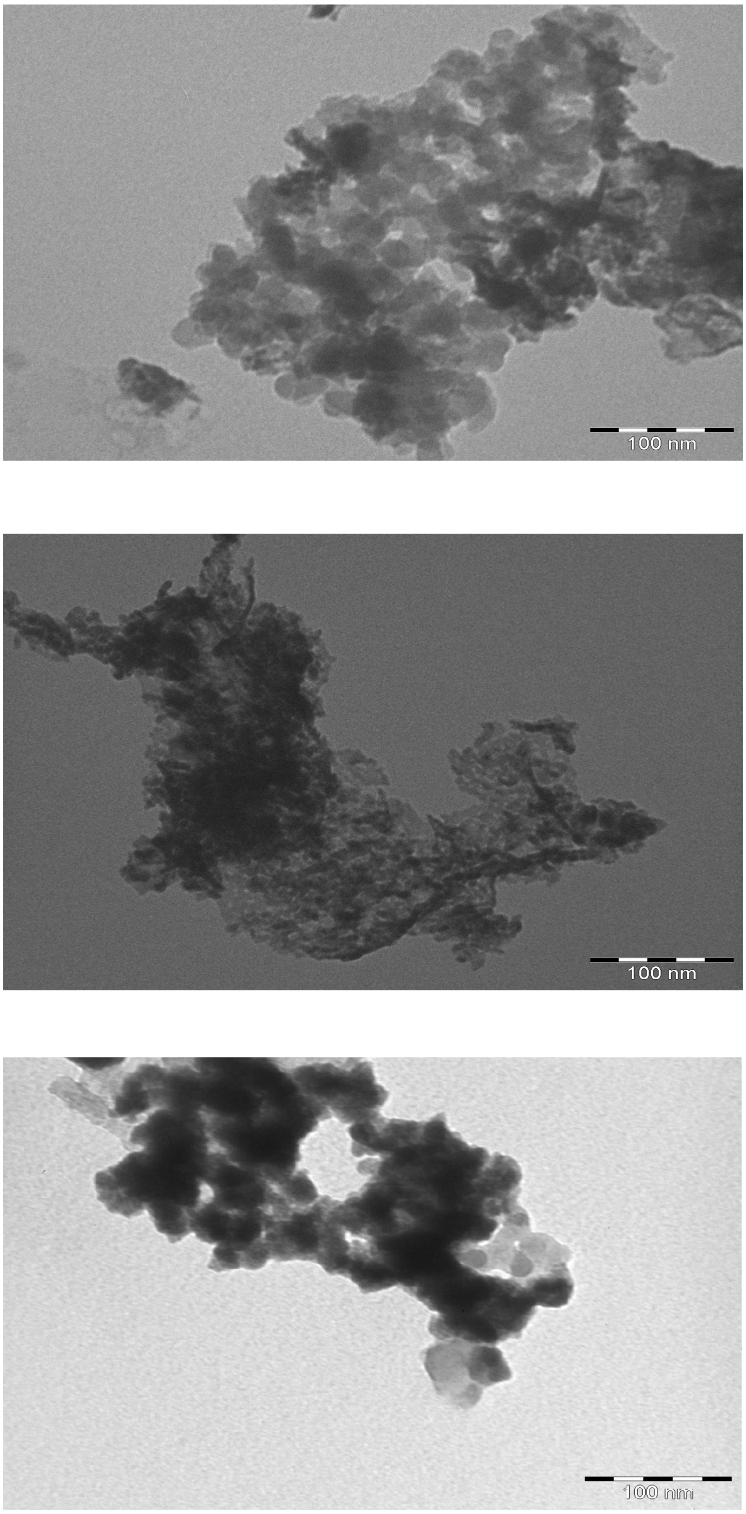

Fig.4.13 TEM images for MoN_x samples heated for 2 hrs at 700 °C (top), 800 °C and 900 °C (bottom)

SEM images of MoN_x samples obtained at higher temperatures revealed porous structure which indicates likely high surface areas in these MoN_x samples.

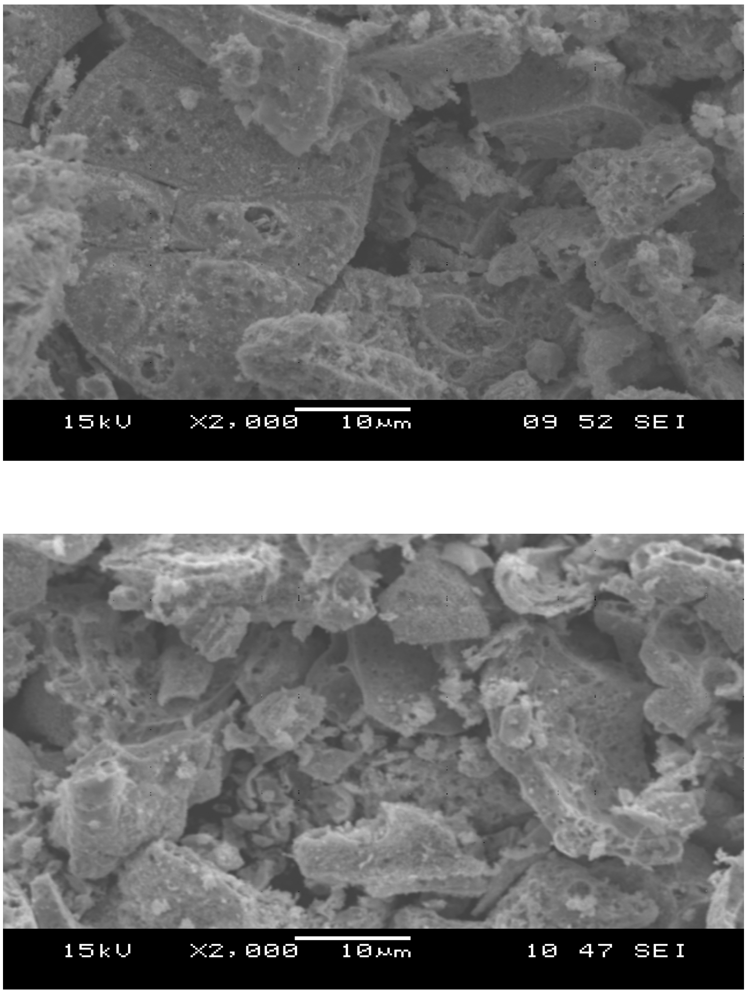

Fig. 4.14 SEM images of the sample obtained by heating at 500 °C for 48 hrs (top) and at 800 °C for 2 hrs (bottom) showing the porous material.

4.4 Conclusions

The polymer obtained from the ammonolysis of $MoCl_5$ at -78°C was annealed at various temperatures under flowing NH_3. Phase pure cubic (rocksalt) MoN was obtained at 700-1000 °C after 2 hrs annealing. Hexagonal (WC-type) MoN samples were obtained at 500 °C after 12, 24 and 48 hrs with amorphous MoN found after 2 hrs annealing of the polymer. A mixture of cubic and hexagonal MoN was obtained after heating at 600 °C ammonia nitrogen for 2 hrs. Molybdenum impurity was observed in the samples obtained at 900 and 1000 °C, while chlorine was observed in the samples obtained at 500 °C for shorter time.

4.5 References

1. A. G. Cairns, J. G. Gallagher, J. S. J. Hargreaves, D. Mckay, E. Morrison, J. L. Rico and K. Wilson, *J. Alloys Cmpds.*, 2009, **479**, 851.
2. H. Wang, W. Li and M. Zhang, *Chem. Mater.*, 2005, **17**, 3262.
3. W. E. Pickett, B. M. Klen and D. A. Papaconstantopoulos, *Physica*, 1981, **B 107**, 667.
4. Z. You-Xiang and H. Shou-An., *Solid State Commun.*, 1983, **45**, 281.
5. R. Fix, R. G. Gordon and D. M. Hoffman, *Thin Solid Films*, 1996, **288**, 116.
6. M. Nagae, T. Yoshio, Y. Takemoto and J. Takada, *J. Amer. Ceram. Soc.*, 2001, **84**, 1175.
7. P. Hones, R. Sanjines and F. Levy, *Surf. Coat. Technol.*, 1997, **94-95**, 398.
8. C. Wiemer, R. Sanjines and F. Levy, *Surf. Coat. Technol.*, 1996, **86-87**, 372.
9. S. Gong, H. Chen, W. Li and B. Li, *Catal. Comm.*, 2004, **5**, 621.
10. M. Nagai, T. Miyao and T. Tsuboi, *Catal. lett.*, 1993, **18**, 9.
11. J. Trawczy´nski, *Catal. Today*, 2001, **65**, 343.
12. E. J. Markel, S. E. Burdick, M. E. Leaphart-II and K. L. Roberts, *Catalysis*, 1999, **182** 136.
13. T. Kadono, T. Kubota and Y. Okamoto, *Catal. Today*, 2003, **87**, 107.
14. S. Ramanathan and S. T. Oyama, *Phys. Chem.*, 1995, **99**, 16365.
15. M. Nagai and T. Miyao, *Catal. Lett.*, 1992, **15**, 105.
16. S. Z. LI, J. S. Lee, T. Hyeon and K. S. Suslick, *App. Catal.*, 1999, **184**, 1.
17. M. Nagai, Y. Goto, A. Miyata, M. Kiyoshi, K. Hada, K. Oshikawa and S. Omi, *Catalysis*, 1999, **182**, 292.
18. H. He, H. X. Dai, K. Y. Ngan and C. T. Au, *Catal. Lett.*, 2001, **71**, 147.
19. H. Jehn and P. Ettmayer, *J. Less Common Metals*, 1978, **58**, 85.
20. T. Kawashima, E. T. Muromachi and P. F. McMillan, *Physica C*, 2007, **460**, 651.
21. L. C. Bull, T. Kawashima, P. F. McMillan, D. Machon, O. Shebanova, D. Daisenberger, E. Soignard, E. T. Muromachi and L. C. Chapon, *J. Solid State Chem.*, 2006, **179**, 1762.
22. P. Ettmayer, *Monatcsh Chem.*, 1970, **101**, 127.
23. D. A. Evans and K. H. Jack, *Acta. Cryst.*, 1957, **10**, 833.
24. H. Hehn and P. Ettmayer, *J. Less Common Metals*, 1978, **58**, 85.

25. M. B. Kanoun, S. Goumri-Said and M. Jaouen, *Phys. Rev.* , 2007, **76**, 134109.

26. G. Hagg, *Z. Phys. Chem.*, 1930, **B 7**, 339.

27. B. Cendlewska, A. Morawski and A.Misiuk, *J. Phys. F: Met. Phys.*, 1987, **17**, L71.

28. S. L. Roberson, D. Finello and R. F. Davis, *Thin Solid Films*, 1998, **324**, 30.

29. A. Wang, F. Capitain, v. Monnier, S. Matar and G. Demazeau, *J. Mater. Synth. Proces.*, 1997, **3**, 235.

30. M. Maoujoud, M. J. Offergeld and F. Bouillon, *App. Surf. Sci.*, 1993, **64**, 81.

31. K. Inumaru, K. Baba and S. Yamanaka, *App. Surf. Sci.*, 2006, **253**, 2863.

32. L. Hiltunen, M. Leskelä, M. Mäkelä, L. Niinistö, E. Nykänen and P. Soininen, *Thin Solid Films*, 1988, **166**, 149.

33. V. Miikkulainen, M. Suvanto and T. A. Pakkanen, *Thin Solid Films*, 2008, **516**, 6041.

34. V. Miikkulainen, M. Suvanto and T. A. Pakkanen, *Chem. Mater.*, 2006, **19**, 263.

35. Y. Wang and R. Y. Lin, *J. Mater. Sci. Eng.*, 2004, **112**, 42.

36. P. Chirico, A. L. Hector and B. Mazumder, *Dalton Trans.*, 2010, **39**, 1.

37. W. Lengauer, *J. Crystal Growth*, 1988, **87**, 295.

38. R. B. Von-Dreele and A. C. Larson, Generallized structure analysis system, Los Alamos National Laboratory, NM87545, USA, December 2002 release.

39. R. B. Von-Dreele and A. C. Larson, GSAS Manual, LANSCE MS-H805, Los Alamos National Laboratory, Los Alamos NM, NM 87545, 2000.

40. M. H. Chisholm, V. Baxter, J. Gama, F. Distasi, A. L. Hector and I. P. Parkin, *Chem. Mater.*, 1996, **8**, 1222.

41. K. Nakamoto, *Infrared and Raman Spectra of Inorganic and Organic Coumpunds* 3rd ed.; J. Wiley: New York, 1978.

42. J-G. Choi, D. Choi and L. T. Thompson, *J. Mater. Res.*, 1991, **7**, 374.

43. D. M. Hoffman, *Polyhedron*, 1994, **13**, 1169.

5. Molybdenum nitrides from ammonolysis of $Mo(NMe_2)_4$

5.1 Introduction

Molybdenum nitrides have been introduced in detail in Chapter 4. Synthesis of molybdenum nitride from amides has been less well studied. The element Mo displays a very rich chemistry in low, intermediate and high oxidation states. Research with this metal is intense in the organometallic/catalysis, co-ordination, bioinorganic, cluster, and solid state materials fields. However, all this activity mainly stems from a limited number of commercially available Mo-containing starting materials such as $Mo(CO)_6$, MoS_2, MoO_3 and $MoCl_5$.[1]

Chisholm[2] reported synthesis of transition metal nitrides from ammonolysis of metal amides $M(NR_2)_n$ where M = a group of 4, 5, or 6 transition metal, $M_2(NMe_2)_6$ where M = Mo, W, and metal hexsamethyldisilylazides, $M(N(SiMe_3)_2)_n$ where M = Ti, V, Cr, Mn, Co, Cu, La, Y, Sn. Molybdenum nitride was formed via ammonolysis of $Mo_2(NMe_2)_6$ with ammonia in a modified Fischer-Porter bottle. To ensure a sufficient amount of NH_3 was present, a 100 – 250% excess of NH_3 was added. The reaction was carried out at -196 °C and was allowed to warm to room temperature. The ammonolysis of $M_2(NMe_2)_6$, where M = Mo, W required a few days at room temperature to go to completion. Other amides, rapidly produced precipitates, with reaction rates being significant at -30 °C. The dark brown polymeric precursor so obtained was dried under vacuum at 40 to 55 °C for 2 hrs. The product upon heating was MoN. Upon further heating to 450 °C the MoN was converted to Mo_2N by further loss of N_2.

Routes to metal amides include transamination, alkane or hydrogen elimination, disproportionation, redistribution and transmetallation. Transmetallation remains the most commonly used, in which a metal halide is treated with an alkali metal amide.[3] The general reaction is given below:

$$L_mMX_n + nLiNRR^* \longrightarrow L_mM(NRR^*)_n + nLiX$$

Careful fractional sublimation of the crude product from the reaction of $MoCl_5$ and $LiNR_2$ (5 equiv) was found to contain a mixture of $Mo(NMe_2)_4$ and $Mo_2(NMe_2)_6$, plus other non-volatile species of lower-valent molybdenum.[4]

The high Lewis acidity of $MoCl_5$ and powerful oxidant character makes this compound incompatible with THF. Its reduction in THF is accompained by the acid-catalysed ring opening polymerization of THF. Non-cyclic ethers do not suffer from this decomposition pathway.[5] Hence Wolczanski and co-workers[5] treated $MoCl_4(Et_2O)_2$ with 5 equ $LiNMe_2$ in Et_2O as an alternative route to $Mo(NMe_2)_5$.

5.2 Synthesis of $Mo(NMe_2)_4$

The purple tetrakis(dimethylamido) molybdenum is highly oxygen and moisture sensitive and decomposes vigorously.[1] The sublimation temperature of $Mo(NMe_2)_4$ is 40-70 °C under vacuum. The sublimation of the product starts at 40 °C and becomes slower when it reaches to 70 °C. Due to this low sublimation temperature the desired product starts subliming from the crude material during solvent removal under vacuum even at room temperature and could be wasted if the reaction flask is not kept cold at 0 °C.

The chemicals used for the synthesis are highly moisture sensitive therefore the whole procedure was carried out in nitrogen atmosphere. All the glassware used for the reaction needs careful washing and overnight drying. Synthesis of $Mo(NMe_2)_4$ was tried using three different methods.

5.2.1 Method 1

Following a literature report,[6] a solution of $MoCl_5$ (16.2 g, 0.059 mol) was made in 200 ml hexane and was transferred to an ice cold slurry of $LiNMe_2$ (15.3g, 0.298 mol) in 120 ml THF. The solution was allowed to warm to room temperature and then stirred for 12 hr followed by heating under reflux for 1 hr. Lithium salts were filtered off and the solution was evaporated under vacuum. The solid obtained was then heated to 70 °C under vacuum with the aim of collecting the product by sublimation. The expected purple solid was never obtained using this method. The reasons for the failure could be reaction of $MoCl_5$ with the THF solvent as stated above.

5.2.2 *Method 2*

$MoCl_4(Et_2O)_2$ (tetrachlorobis(diethylether)molybdenum(IV)) was prepared and then used for the synthesis of $Mo(NMe_2)_4$ via the procedures given in literature.[1, 5] An ice cold slurry of $LiNMe_2$ (1.02 g, 0.02 mol, 5eq) in 10 ml of Et_2O was vacuum transferred to solution of $MoCl_4\ (Et_2O)_2$ (1.36g, 0.004 mol) in 10 ml of THF. The reaction mixture was stirred at 0 °C for 4 hrs then was allowed to come at room temperature and stirred for a further 48 hr. The brown solid was collected by filtration and then heated at 70 °C under vacuum. The sublimation tube was cooled with dry ice and acetone. A few particles of purple solid, believed to be $Mo(NMe_2)_4$, were collected but the yield was very low and the product decomposed to a brown material in the sublimation tube under vacuum.

5.2.3 *Method 3*

Synthesis of $Mo(NMe_2)_4$ was carried out following the procedure given by Chisholm.[5] The procedure was modified in terms of amount of reactant and solvent used, and the sublimation was carried by heating the reaction flask in an oil bath, connected to a "U" shape tube cooled using dry ice. Solid $MoCl_5$ (10.95 g, 40 mmol) was added in portions to an ice cold slurry of $LiNMe_2$ (10.2 g, 200 mmol, 5 eq) in hexane (80 ml) and ether (100 ml). The reaction was exothermic. The reaction mixture was then allowed to warm to room temperature and was stirred overnight, after which time the solvent was removed under vacuum. Hexane (80 ml) and pentane (25 ml) was added. The dark brown solution was then filtered to remove LiCl by a standard Schlenk tube filtration technique. The filtrate was evaporated to dryness under vacuum to yield a sticky black solid. The flask was kept cooled at 0 °C during solvent removal. The black solid was sublimed under vacuum at 40-70 °C, resulting in the highly volatile purple $Mo(NMe_2)_4$. The solid $Mo(NMe_2)_4$ was collected directly from the sublimation tube without washing it with pentane as was carried out by Chisholm and co-workers. The remaining residues (containing $Mo(NMe_2)_4$, $Mo_2(NMe_2)_6$ and other products) were re-dissolved in 50 ml hexane and 15 ml of pentane. Filtration and drying was repeated in the same way as before and a second crop of $Mo(NMe_2)_4$ was collected in the sublimation tube. The process was repeated for the 3rd time but yielded little product which could be collected. The whole process produced 1.3 g of purple crystalline $Mo(NMe_2)_4$ with 12 % yield. No attempt was made to sublime at a higher temperature to collect $Mo_2(NMe_2)_6$.

The chemical reaction could be given as:

$$MoCl_5 + LiNMe_2 \longrightarrow {}_xMo(NMe_2)_4 + {}_yMo_2(NMe_2)_6 + 5\,LiCl$$

+

other non-volatile material

The final purple crystalline product was characterised using NMR spectroscopy (Fig. 5.1) and elemental analysis. ^1H NMR (C_6D_6) singlet δ (ppm): 3.273. The result was compared with the literature data δ (ppm): 3.273.[4, 5]

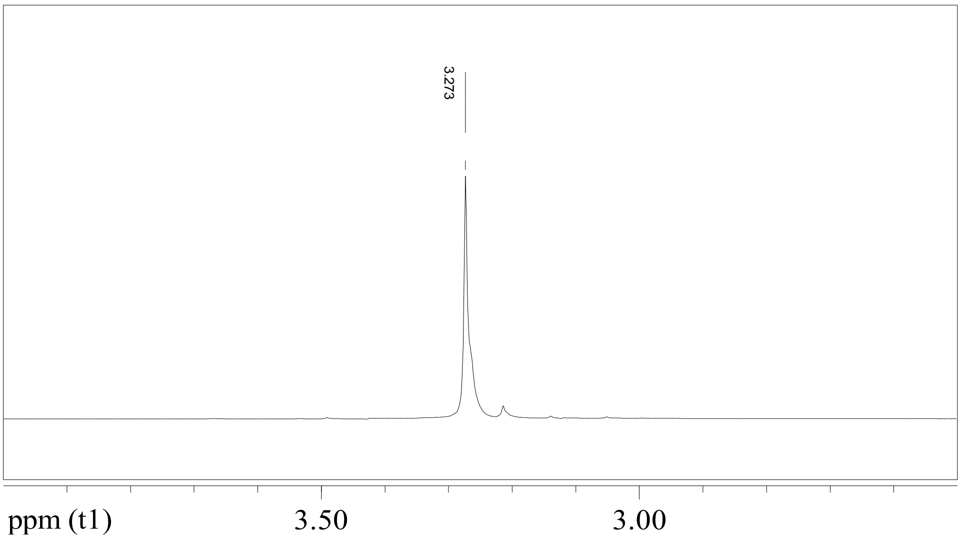

Figure 5.1 NMR spectrum obtained for $Mo(NMe_2)_4$

Elemental analysis of the sublimed $Mo(NMe_2)_4$ was very close to the theoretical values.

Table 5.1 Elemental analysis of $Mo(NMe_2)_4$

	Elemental Analysis (%)		
Elements	C	H	N
Sublimed product	34.73	8.74	20.23
Theoretical for $Mo(NMe_2)_4$	35.35	8.83	20.62

5.2.4 Ammonolysis of $Mo(NMe_2)_4$

The reaction was carried out using a Schlenk line. ~10 ml of liquid ammonia was added to a solution of 0.5g $Mo(NMe_2)_4$ in THF under nitrogen with continuous stirring. The reaction mixture was left to come to room temperature until the excess ammonia was evaporated. The black precipitate of molybdenum amide polymer ~ 0.280g was then filtered and dried under vacuum. The likely reaction is given below:

$$Mo(NMe_2)_4 + (y+z)NH_3 \longrightarrow Mo(NMe_2)_x(NH_2)_y(NH)_z + (4-x)\,HNMe_2$$

5.2.5 Pyrolysis of polymeric precursor

The polymer was then transferred to a ceramic crucible (boat shape) inside a silica tube, which was loaded inside the glove box. The silica tube was provided with an arrangement of taps to allow flushing of the hoses before the sample was exposed to the gas flow. The sample was then heated under flowing ammonia to 600 °C, or 1000 °C for a period of 2 hrs. A column of molecular sieves (synthetic zeolite) was used to dry the ammonia.

5.2.6 Measurements

TGA was carried out with a Mettler Toledo TGA/SDTA85le instrument under flowing nitrogen with flow rate of 50 ml/min and temperature ramp rate of 10 °C/min. The temperature was raised from 25 to 800 °C, and was held at maximum temperature for 20 minutes. PXD patterns were collected with a Siemens D5000 diffractometer using a sample holder for air sensitive material. Data obtained through PXD was compared with the JCPDS and ICSD databases. TEM was performed on a Hitachi H7000 with accelerating voltage of 75 kV. Samples for TEM were made by ultrasound dispersal using toluene as the solvent and were deposited on carbon coated Cu grids. Samples were sent for combustion analysis (C, H and N) to Medac Ltd (Egham, Surrey). Infrared spectroscopy was performed on CsI disks using a Perkin Elmer Spectrum One FT-IR spectrometer.

5.3 Results and discussion

5.3.1 Analysis of the polymeric molybdenum amide precursor

The IR spectrum of the polymeric precursor (Fig.5.2) shows an intense absorption peak at 3245 cm^{-1}, and a less intense one at 1605 cm^{-1}, attributed to ν (NH)[7] and δ (NH_2)[2, 7] respectively. Low intensity absorption peaks at 1452 and 1250 cm^{-1} could be due to ν (C≡N). Less intense peaks in the range of 2930 to 2760 cm^{-1} could be attributed to ν (CH). An intense peak at ~850 cm^{-1} could be attributed to ν (M-N), which is shifted to ~1000 cm^{-1} in the final product.

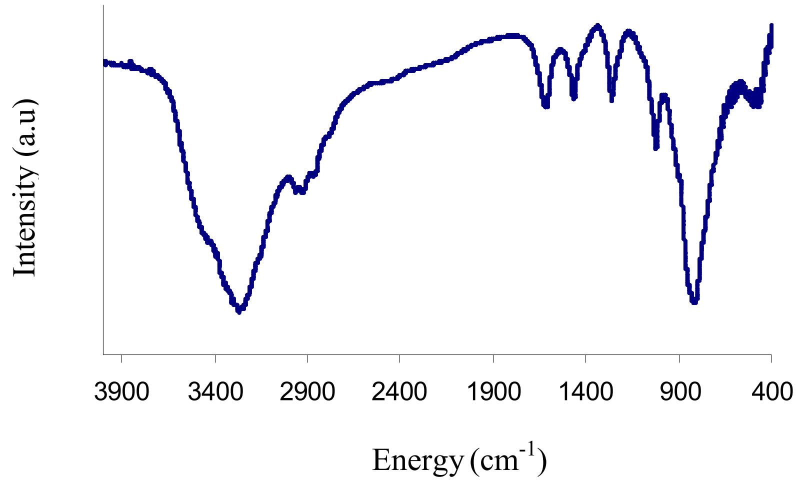

Fig.5.2 IR spectrum of the polymeric molybdenum amide precursor.

The TGA curve for the polymer precursor (Fig. 5.3) shows mass losses at lower temperature due to amide decomposition and some ammonia leaves below 600 °C, while the mass loss at 700 °C and above is due to NH_3 and N_2.[2]

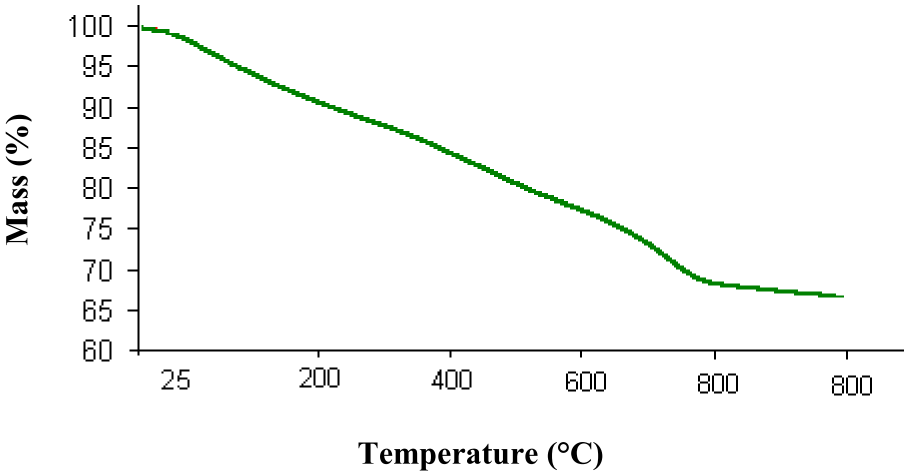

Fig.5.3 TGA curve showing the mass loss when the polymer precursor is heated in N_2.

5.3.2 Analysis of MoN_x samples obtained by annealing the polymeric amide precursor under ammonia

PXD patterns obtained for the sample annealed at 600 °C showed phase pure hexagonal δ-MoN_x. A mixture of the cubic phase with hexagonal MoN_x was obtained when the same temperature was applied to an $MoCl_5$-derived precursor (Chapter 4). The patterns obtained for the sample annealed at 1000 °C showed the hexagonal δ-MoN and cubic δ-MoN phases. Some Mo was observed via a peak at 40° 2θ, similarly to the sample prepared from $MoCl_5$. Particle sizes of these samples were found to be around ~ 35 nm using the Scherrer equation.[8] TEM images show similar particle sizes in the final products.

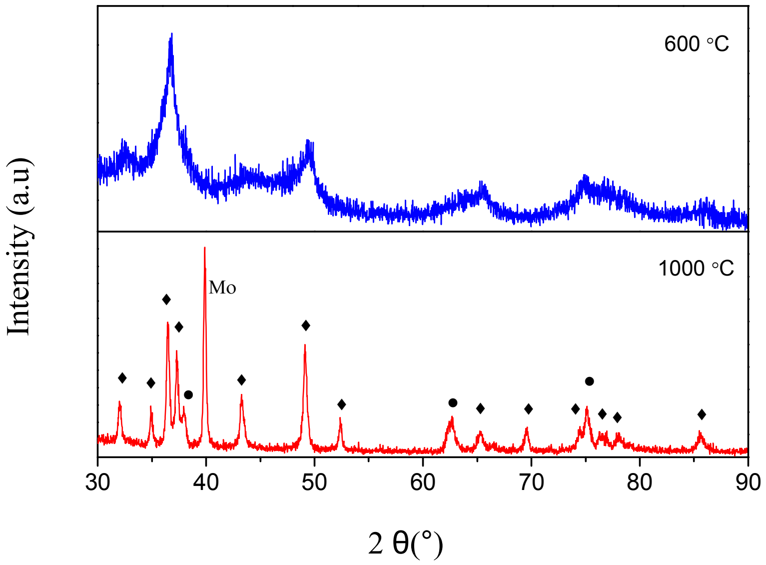

Fig. 5.4 PXD patterns for MoN_x samples obtained at the temperatures shown. Diamond symbols mark peak positions for hexagonal phase reflections, circles the cubic phase and Mo = molybdenum. All the peaks at 600 °C are hexagonal MoN_x.

Elemental analysis (Table 5.2) showed hydrogen-free (< 0.1% H) MoN_x samples at both temperatures. Carbon was found in both the samples. Carbon contents in transition metal nitrides increase the hardness of the material.[9] The sample obtained at 1000 °C was low in carbon compared with the sample obtained at 600 °C, and was N_2 deficient as N leaves at 700 °C and above. The MoN_x samples obtained from chloride based precursor at respective temperature didn't show any carbon and had slightly higher for N contents (Chapter 4).

Table 5.2 Elemental analysis for MoN_x samples

Sample	Sample temperature	%C	%N	Elemental composition
MoN_x	600 °C	1.57	10.86	$MoN_{0.85}C_{0.14}$
MoN_x	1000 °C	0.86	7.86	$MoN_{0.59}C_{0.07}$

%H <0.10 throughout; MoN contains 12.78 %N

IR spectra (Fig. 5.5) for both the samples showed similar composition. The weak absorption peak at ~ 3420 cm^{-1} and ~1625 cm^{-1} in both the samples could be attributed to ν (NH)[7] and δ (NH_2)[2, 7] respectively. A weak ν (CH) band at ~2920 cm^{-1} is also observed in the pattern even after heating to 1000 °C. A broad absorption band centred ~ 1000 cm^{-1} could be attributed to ν (Mo-N).

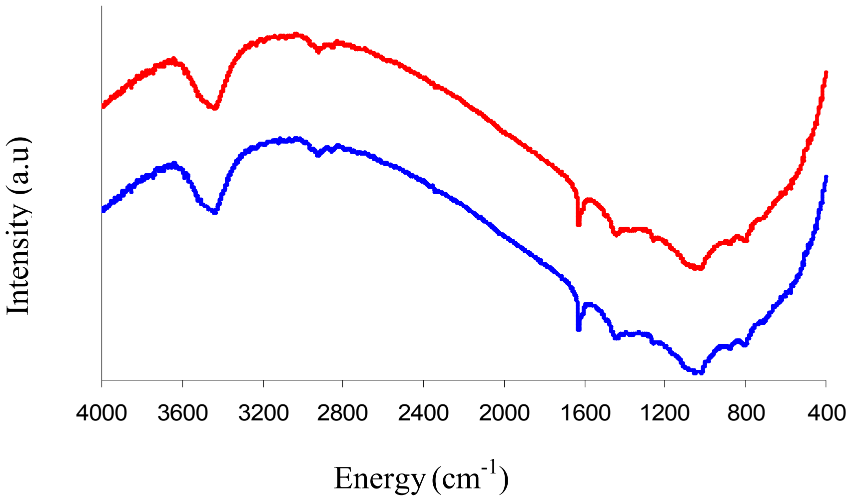

Fig 5.5 IR spectra obtained for the MoN_x samples top (1000 °C) and bottom (600 °C)

A small mass loss was observed at lower temperature in the TGA of the sample obtained at 600 °C, which shows most of the amide precursor has been decomposed. The total mass loss of 0.01% was observed when annealing the sample obtained at 1000 °C in the TGA at 800 °C (Fig 5.6).

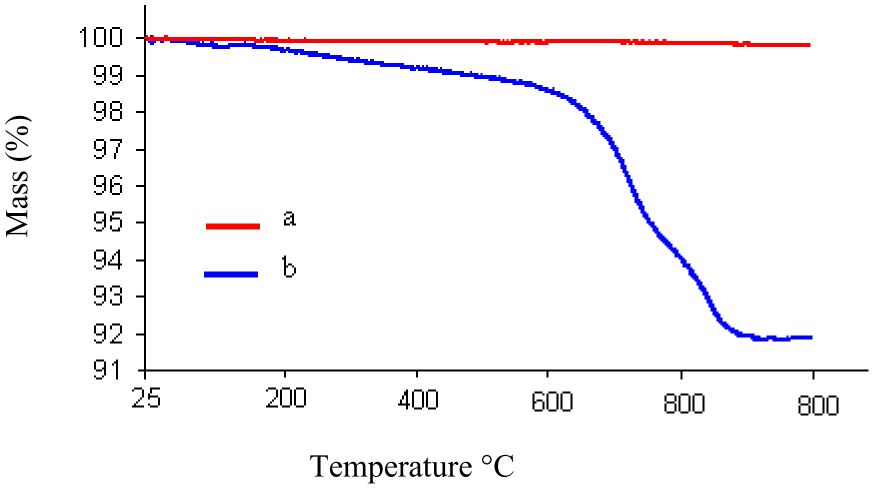

Fig. 5.6 TGA curves showing the %mass loss for the MoN_x samples 1000 °C (a), and 600 °C(b)

TEM images of the samples obtained at 600 °C showed a mixture of nanotubes and approximately spherical particles. Nanotubes increase the surface area of the material which is a useful characteristic for catalysis.[10] Samples obtained at 1000 °C were mainly composed of spherical particles which were mostly agglomerated. Particles of both the samples were found to be ~30 to 60 nm in size. No nanotubes were found in the MoN_x samples obtained by annealing the $MoCl_5$ based precursor (Chapter 4). The reason could be the presence of NH_4Cl, which sublimes[11] out at ~ 340 °C causing the agglomeration of the product. Nano-rods of early transition metal nitrides have been reported through solid state synthesis e.g. by ammonolysis of Nb_2O_5 ($Nb_{3.49}N_{4.56}O_{0.44}$), MoO_3 (δ -MoN or γ-MoN) or molybdenum polysulfide (MoN).[12-14] Ta_3N_5 nanorods have been reported from the reaction of $TaCl_5$ with $LiNH_2$ in refluxing mesitylene, followed by annealing.[15]

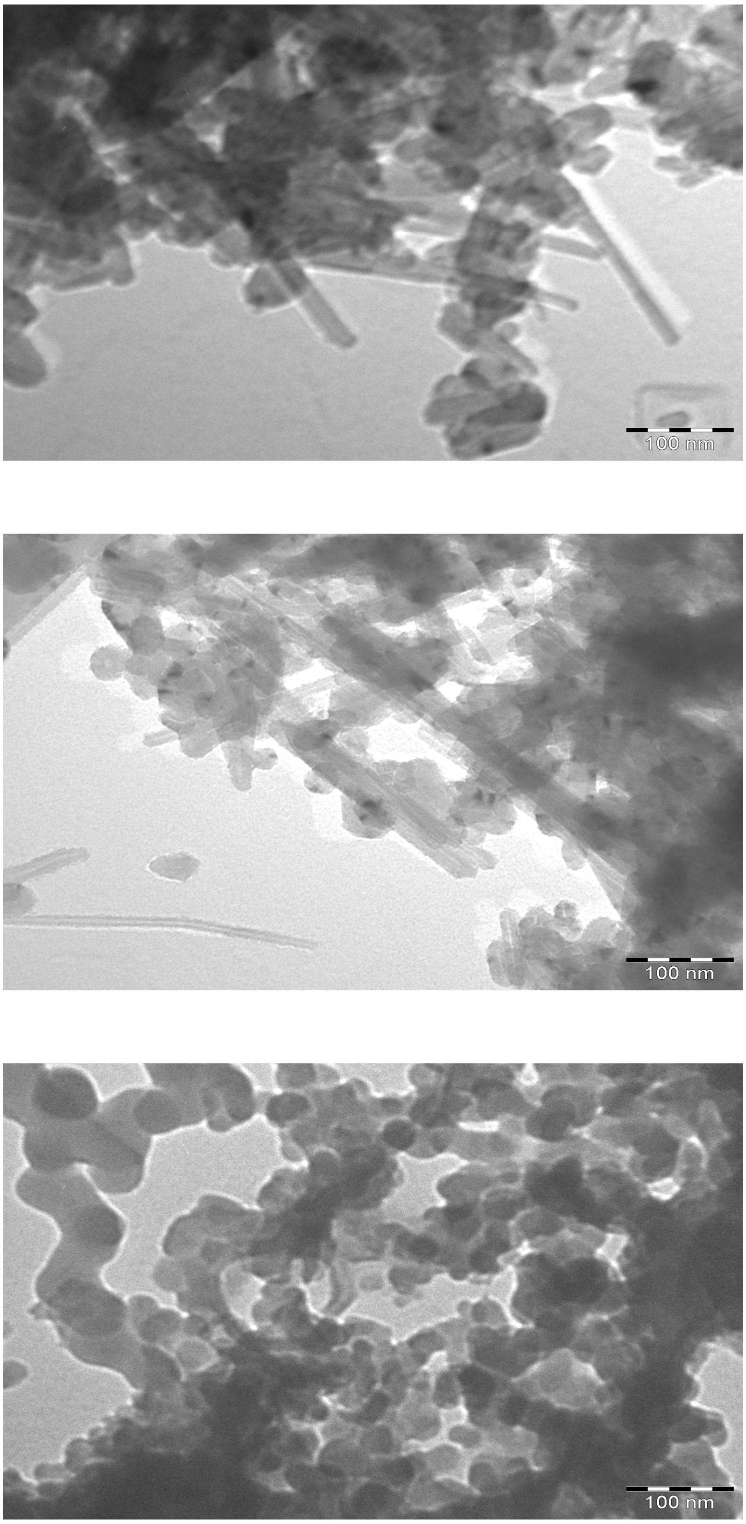

Fig. 5.7 TEM images for the MoN_x samples obtained at 600 °C (top and middle) and 1000 °C (bottom)

5.4 Conclusions

Solution phase ammonolysis of $Mo(NMe_2)_4$ and further annealing at 600 °C under ammonia produced nanotubes of phase pure hexagonal δ-MoN_x. Heating the polymeric precursor at 1000 °C produced hexagonal δ-MoN mixed with rock salt MoN_x phase. MoN_x samples obtained at 600 °C via the chloride precursor (Chapter 4) showed δ-MoN mixed with rock salt MoN_x sample, while at 1000 °C cubic MoN_x and Mo metal was obtained. Reduction of the molybdenum metal appears to be less facile when obtained from the amide and this may be due to the presence of carbide in the lattice.

5.5 References

1. S. Francois, S. Dirk and P. Rinaldo, *Eur. J. Inorg. Chem.*, 2001, 2699.
2. M. H. Chishlom, D. V. Baxter, G. J. Gama, V. F. Distasi, A. L. Hector and I. P. Parkin, *Chem. Mater.*, 1996, **8**, 1222.
3. M. Lappert, A. Protchenko, P. Power and A. Seeber, *Metal Amide Chemistry, 2nd Eddition,* , 2008, 149.
4. M. Chisholm, F. A. Cotton, B. A. Frenz, W. W. Reichert, L. W. Shive and B. R. Stults, *J. Amer. Chem. Soc.*, 1976, **98**, 4469.
5. D. S. Kuiper, P. T. Wolczanski, E. B. Lobkovsky and T. R. Cundari, *Inorg. Chem.*, 2008, **47**, 10542.
6. D. C. Bradley and M. H. Chisholm, *J. Chem. Soc*, A, 1971, 2741-2744.
7. K. Nakamoto, *Infrared and Raman Spectra of Inorganic and Organic Coumpunds* 3rd ed.; J. Wiley: New York, 1978.
8. R. B. Von-Dreele and A. C. Larson, GSAS Manual, LANSCE MS-H805, Los Alamos National Laboratory, Los Alamos NM, NM 87545, 2000.
9. H. J. Holleck, *J. Vac. Sc. Tech.*, 1986, **A 4**, 1384.
10. B. Mazumder and A. L. Hector, *J. Mater. Chem.*, 2009, **19**, 4673.
11. A. Wang, F. Capitain, V. Monnier, S. Matar and G. Demazeau, *J. Mater. Synth. Proces.*, 1997, **3**, 235.
12. W. Hu, Y. Zhao, Z. Liu and Y. Zhu, *Nonotech.*, 2007, **18**, 095605.
13. D. Mckay, J. S. J. Hargreaves, J. L. Rico, J. L. Rivera and X.-L. Sun, *J. Solid State Chem.*, 2008, **181**, 325.
14. S. Wang, Z. Zhang and Y. Qian, *J. Solid State Chem.*, 2004, **177**, 2756.
15. B. Mazumder and A. L. Hector, *J. Mater. Chem.*, 2008, **18**, 1392.

6. Metal containing silicon nitrides

6.1 Introduction

Sol-gel-synthesis of ceramic materials has become a rich and rapidly growing field of modern materials research. It has been widely used for the synthesis of tailored oxide ceramics,[1] oxide/nitride composites,[2] and nitride ceramics.[3, 4] Sol-gel routes for non-oxide materials are poorly developed due to difficulties associated with the chemistry involved at each step of the process. The reagents and intermediates in these reactions are highly sensitive compounds such as amides, which are readily decomposed by water. Most reports to date are on the production of high surface area silicon nitrides for catalysis.[5-7]

Ammonolysis of dialkylamide groups results in an amide moiety that can act as a nucleophile toward another metal centre yielding a bridging imide group. A polymeric product containing amide, imide and unreacted dialkylamide groups results, the balance between these varying with reaction conditions. The resultant amide/imide gels can then be heated to produce nitrides with loss of ammonia.[8]

Virtually all elements other than silicon which would be of interest in nitride materials processed using sol-gel techniques are less electronegative than silicon. Most are also larger and hence will expand their coordination spheres more readily. Hence the reactivity of precursors will tend to be higher and their exposure to NH_3, or to other cross-linking agents such as $(Me_3Si)_2NCN$, often leads to precipitation.[9]

One approach to this problem has been to dope other elements into silicon precursors such that the chemistry of the sol-gel process is essentially silicon based. Others have produced mixed element nitrides by balancing reaction rates of a silicon amide and another element amide with ammonia. Either way, the aim is to produce materials in which the properties of the silicon nitride host are augmented.[9]

Cheng[6] has reported Si/B/N through lithiation of $Si(NMe_2)_3(NH_2)$ with BuLi, resulting in a precursor that can react with boron halide yielding Si-N-B bonds. This has been reacted with BCl_3 or cyclic borazines to make precursors containing a 3:1, 1:1 or 2:3 ratios of Si : B. These precursors have peripheral groups available for substitution with NH_3. Treatment of the precursors with ammonia in THF in the presence of a trifluoromethane sulfonic acid catalyst led to rigid or semirigid gels. Pyrolysis under N_2 at 1000 °C gave mesoporous solids with high surface areas and no free carbon.

In similar work, Cheng et al.[10] reported mesoporous palladium-loaded silicon nitride composites by a non-aqueous sol-gel chemical route. Nanocomposites of Pd-Si_3N_4 were prepared by pyrolysis of a silicon palladium imide-chloride complex which was synthesised by reaction of silicon diimide gel with palladium chloride. Pyrolysis was carried out at 1000 °C under NH_3. The procedure is shown in Fig. 6.1.

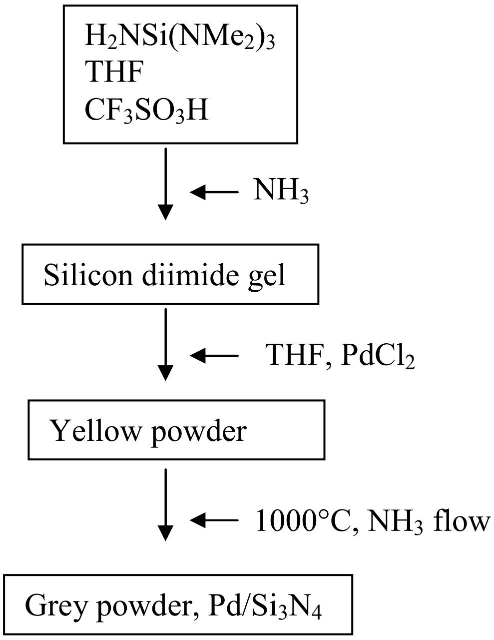

Fig. 6.1 Step wise scheme showing Pd/Si_3N_4 synthesis

There is also an interest in making aluminium-silicon nitrides to increase the basicity of silicon nitrides for use in catalysis. Kaskel[11] developed a single source precursor to Si/Al/N compositions from the reactions of $Si(NHEt)_4$ with trimethyl- or triethyl-aluminium. A highly Si depleted composition was obtained and $Si(NHEt)_4$ was detected in the gaseous by-product when atmospheric pressure conditions were used for the reactions. The higher reactivity of the Al centre was believed to have caused sequential reactions, with Al reacting first then Si. Ammonolysis in supercritical NH_3 was needed to achieve materials with close to a 1 : 1 Al : Si ratio and these were homogeneous on the length scale of an EDX experiment. The material was obtained as flakes as no attempt to control the gelation was made.

Jansen *et.al*[12] exposed mixed solutions of metal (Ti, Zr, Ta) and silicon amides to ammonia in solution and the resulting gels were pumped to dryness. These were heated to 1000 or 1500 °C under NH_3. At 1000 °C the Ti/Si and Zr/Si materials were amorphous, whereas TaN had begun to crystallise at this temperature in the Si/Ta material. At 1500 °C all the three were composites of MN nanocrystals and an amorphous M/Si/N matrix. The crystallisation of the metal nitride reflects the higher mobility of the metal ions in a nitride lattice compared with the small, covalently bound silicon atom. Such composites are of interest as hard materials since the movement and growth of dislocations in the hard, nanocrystalline phase are inhibited by the amorphous phase.[9]

The polymer obtained using two alkylamides with similar rates of ammonolysis, contains two different metals or semi-metals homogeneously distributed on a molecular scale. Like the hydrolysis properties of alkoxides in sol-gel chemistry, the ammonolysis properties of alkyl amides can be varied in a wide range by proper selection of the organic groups bonded to the nitrogen atoms, which act through steric and electronic effects.[13, 14]

This work examines synthesis of silicon based nitride ceramics through controlled coammonolysis of two different alkylamides,[15-18] specifically the incorporation of tantalum and molybdenum into silicon nitride are examined.

6.2 Synthesis of the $Si(NHMe)_4$

Tetra(methylamino)silane (TMAS) was synthesised by condensing methylamine (99%, 100 ml, 2.253 mol, 14 equiv) on to a stirred solution of silicon tetrachloride (99%, 18 ml, 0.157 mol) in dry n-pentane (140 ml) at -78 °C (acetone/dry ice). White solid was formed immediately and the reaction mixture was filtered through a sinter to remove the solid methylamine hydrochloride by-product. The solvent was removed from the filtrate under reduced pressure yielding on oily off-white solid. The reaction is given below:

$$SiCl_4 + 8H_2NCH_3 \xrightarrow{\text{n-pentane}} Si(NHCH_3)_4 + 4CH_3NH_2.HCl$$

Purification of TMAS was achieved by sublimation of the crude material at 450 °C under vacuum, from which a transparent, low-melting crystalline solid was formed.[19] The solid was characterized with ^1H and ^{13}C NMR. The NMR data showed that the sublimation successfully purified TMAS.[20] NMR of sublimed solid ^1H δ (ppm): 2.51 (d, 3*H,* $Si(NHCH_3)_4$), 0.27 (broad ^1H, $Si(NHCH_3)_4$), ^{13}C δ (ppm): 28
Elemental analysis of the sublimed material matches expected values (Table 6.1).

Table 6.1 Elemental analysis of TMAS

	Elemental Analysis (%)		
Elements	C	H	N
Sublimed product	32.03	11.35	37.90
Theoretical for $Si(NMe)_4$	32.40	10.88	37.77

6.2.1 Acid catalysed reaction of TMAS to produce silicon diimide gel

TMAS (0.5 g, 3.37 mmol) was dissolved in dry THF (6 ml) in a pressure tube (Fig. 6.2) then the sodium dried ammonia was condensed into the graduated capillary tube of the glassware at -78 °C. The Young's tap was closed, the pressure withstanding tap opened and the capillary tube was allowed to warm outside the bath in order to ammonia to be transferred. The mixture was allowed to warm to room temperature with the pressure withstanding tap closed overnight (18hrs) and then one drop of triflic acid was added. The sol was allowed to stand for 4 hrs over which time monolithic gel formed. Solid white gel (Fig. 6.3) formed occupying the whole volume of the original sol. The likely reaction sequence is;

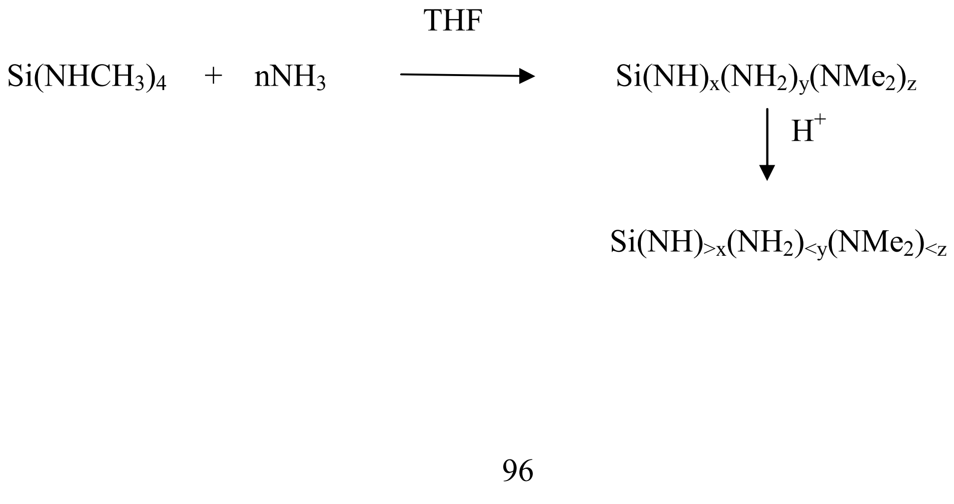

$$\begin{tikzcd} Si(NHCH_3)_4 + nNH_3 \arrow[r, "THF"] & Si(NH)_x(NH_2)_y(NMe_2)_z \arrow[d, "H^+"] \\ & Si(NH)_{>x}(NH_2)_{<y}(NMe_2)_{<z} \end{tikzcd}$$

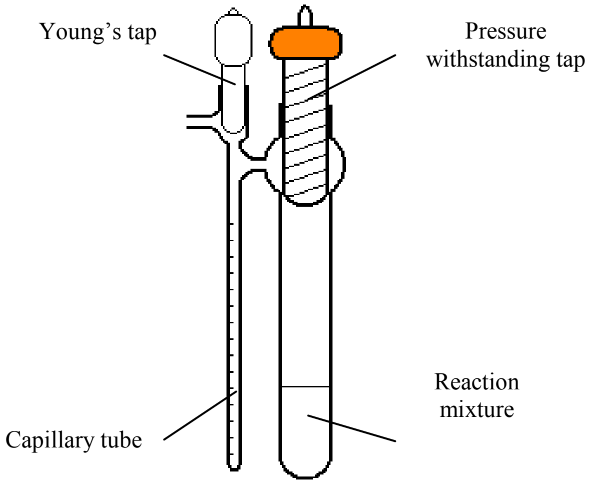

Fig. 6.2 Ammonia transfer and gel-forming apparatus

Fig. 6.3 Silicon diimide monolithic gel

6.2.2 Affect of acid with TMAS

The catalytic effect of triflic acid was discussed by Cheng *et. al,*[21] who suggested that the effect of the catalyst is displacement of amide groups as H_2NMe, resulting in precursor molecules containing triflate groups. The electron withdrawing effect of a triflate group would render the precursor more susceptible to nucleophic attack. Triflate is then a good leaving group. Figure 6.4 shows the triflic acid effect on TMAS. Here the effect seems to be to promote condensation.

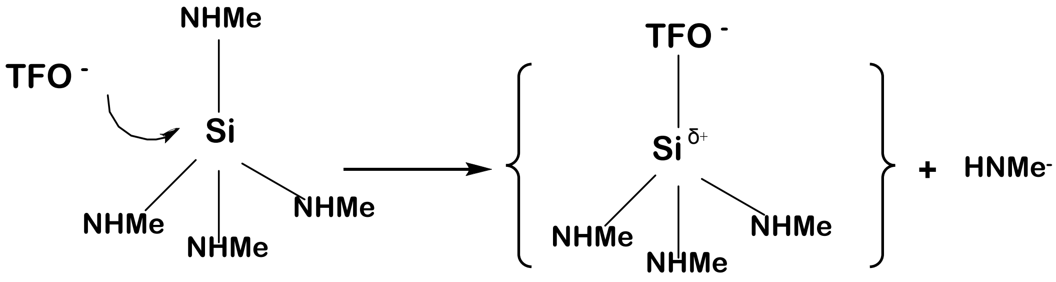

Fig. 6.4 Catalytic effect of triflic acid on ammonolysis/ condensation of TMAS precursor

6.3 Synthesis of metal containing silicon nitrides

6.3.1 Co-ammonolysis of metal and silicon amides

A pressure tube (Fig. 6.2) provided with a pressure withstanding tap and magnetic stirrer was used (Fig. 6.2). The pressure tube was charged with 0.5 g (3.37mmol) $Si(NHMe)_4$ and either 0.120g (0.337 mmol) of $Ta(NMe_2)_5$ or 0.05 g (0.337 mmol) of $Mo(NMe_2)_4$ inside the glove box. 6 ml of THF was added to the amide mixture and it was stirred to obtain a homogeneous solution. 0.06 ml dry NH_3 was condensed into the solutions at -78 °C. The pressure valve was sealed tightly. The solutions were left overnight to come to room temperature. The pressure was then released. A non-viscous suspension was obtained and a drop of triflic acid was added to each of the solutions and they were left to stir overnight. The viscosity increased and colloidal suspensions were obtained. Ta/Si was found to be more viscous than the Mo/Si amide suspension. The metal-silicon amide precursor was then dried under vacuum and powdered solids were collected. The reactions yielded 0.4 g of yellow Ta/Si and 0.3 g of dark brown Mo/Si polymeric amide precursor.

6.3.2 Pyrolysis of polymeric metal-silicon amide precursor

The polymer was transferred to a ceramic crucible (boat shape) inside a silica tube, which was loaded inside the glove box. The silica tube was provided with an arrangement of taps to connect to allow flushing of the hoses before the sample was exposed to the gas flow. They were then heated under flowing ammonia to two different temperatures, 600 °C or 1000 °C, for the duration of 2 hrs each.

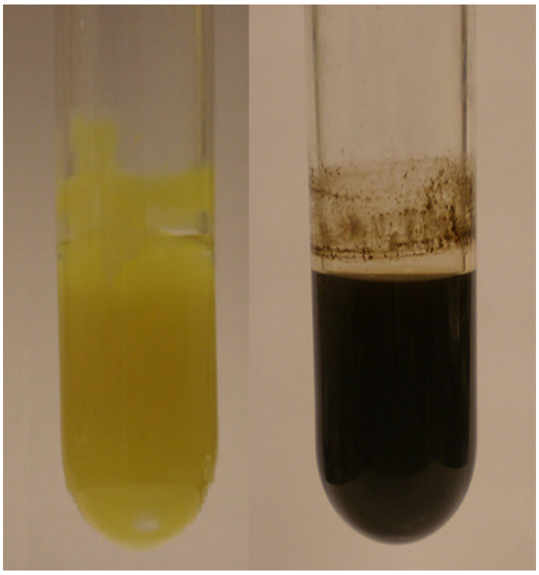

Fig. 6.5 The thick yellow Ta/Si amide gel and the dark brown Mo/Si amide gel before drying

6.3.3 *Measurements*

PXD patterns were collected using a Siemens D5000 diffractometer using a sample holder for air sensitive materials. TGA was carried out in a Mettler Toledo TGA/SDTA85le instrument under flowing nitrogen with flow rate of 50 ml/min. The temperature was raised from 25 °C to 800 °C with a ramp rate of 10 °C/min and was held at maximum temperature for 20 minutes for each sample. TEM was performed on a Hitachi H7000 with accelerating voltage of 75 kV. Samples were made by ultrasound dispersal using dry toluene as the solvent and were deposited on carbon coated Cu grids.

6.4 Results and discussion

6.4.1 Analysis of polymeric metal-silicon amide precursors

The IR spectrum for the polymeric precursors (Fig. 6.6) shows a strong absorption peak at ~3360 cm^{-1} ν (NH).[16, 22] The weak absorption peak at ca. 1609 cm^{-1} is consistent with δ (NH_2).[16] Two ν (CH) peaks were obtained in the range of 2960-2800 cm^{-1}, and a higher intensity peak at ~ 1350 cm^{-1} could be due to ν (CN).

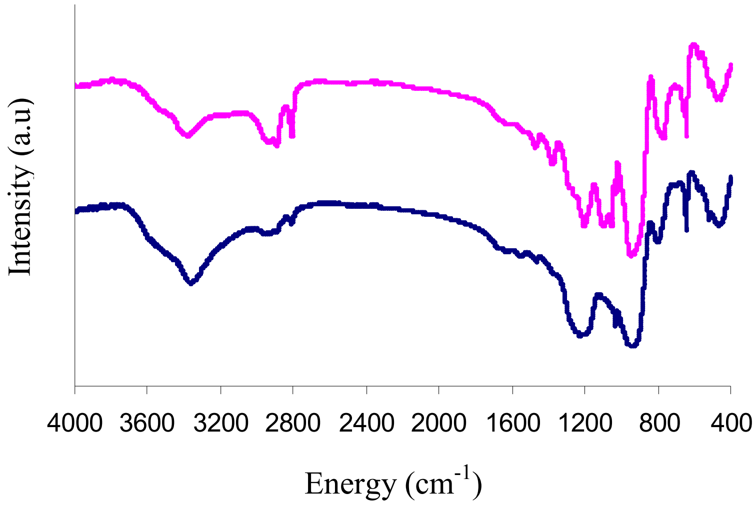

Fig. 6.6 IR spectra for the polymeric precursors, Mo/Si (bottom) and Ta/Si (top)

TGA curves obtained from the metal-silicon amide polymer precursors (Fig. 6.7), showing two step mass losses. The mass loss in the Ta/Si and Mo/Si polymers were ~38 and 26% respectively. The greater mass loss of the Ta/Si precursor shows more condensation and oligomer loss than in the Mo/Si polymer suggesting less condensation (and thus cross-linking) in the Ta/Si precursor during gel formation. The major mass losses in both the polymer precursors were observed below 500 °C as amide groups with some NH_3 and N_2 are lost. Mass loss at 700 °C and above is mainly due to N_2 loss[16] and as expected the Mo system shows a small step in this region.

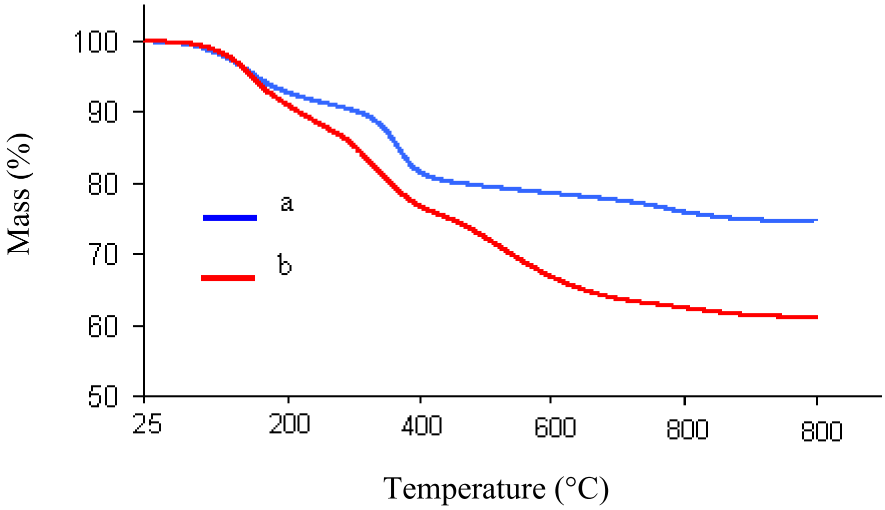

Fig. 6.7 TGA curves showing the mass losses of the polymeric amide precursors, Ta/Si (a) and Mo/Si (b)

6.4.2 Analysis of M/Si/N samples obtained after annealing the polymeric precursors under ammonia

PXD patterns of Ta/Si/N showed amorphous material even at high temperature (Fig. 6.9), no peak for tantalum nitride was observed in the pattern. In previous work using the same precursors at a 1:1 molar ratio pyrolysis of amorphous Ta/Si/N at 1000 °C yielded cubic TaN.[12] PXD patterns (Fig. 6.8) for the sample obtained at 600 °C showed the amorphous material, while crystalline nanocomposites containing hexagonal MoN were obtained at 1000 °C. A peak for molybdenum metal was observed in the MoN_x samples obtained through the pyrolysis of $MoCl_5$ or $Mo(NMe_2)_4$ based polymer precursors at 1000 °C (Chapter 4 and 5), but no metal peak was observed even at that temperature in the molybdenum/silicon materials.

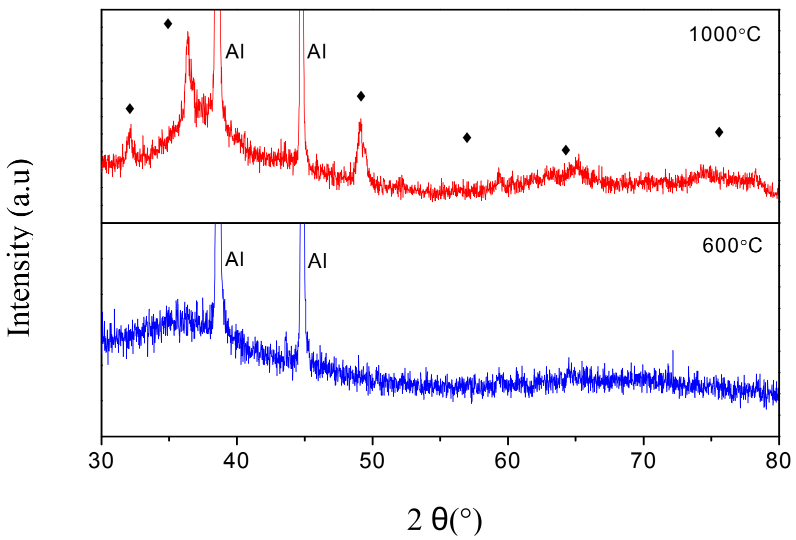

Fig. 6.8 PXD patterns obtained for the Mo/SiN samples obtained at 600 and 1000 °C. (◆)symbols show reflections for hexagonal MoN_x

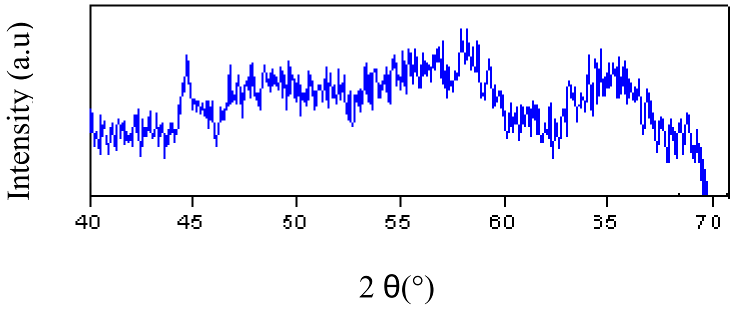

Fig. 6.9 PXD pattern for Ta/SiN samples obtained at 1000 °C

Elemental analysis of the samples showed slightly higher carbon contents in the M/Si samples obtained at 600 °C than in the samples obtained at 1000 °C. Hydrogen contents were found to be consistently in the range of 1.1 to 1.33% in all the samples obtained. It is known that silicon nitrides retain much more hydrogen than the metal nitrides as amide groups survive to higher temperature.[9] Nitrogen contents were lower in the samples obtained at 1000 °C as N_2 leaves the system at this elevated temperature.

Table 6.2 Elemental analysis of M/SiN$_x$ samples (M = Ta, Si)

Sample	Synthesis/ °C	%C	%H	%N
TaSiN$_x$	600	0.83	1.10	12.00
TaSiN$_x$	1000	0.36	1.26	10.59
MoSiN$_x$	600	0.77	1.21	15.13
MoSiN$_x$	1000	0.24	1.33	10.70

The IR spectra of the samples obtained at 600 °C show a weak absorption peak at ~3350 cm^{-1} ν (NH).[16] ν (C≡N) at 2188 cm^{-1} is observed in the Mo/Si/N sample obtained at 600 °C. A broad band at ~950 to ~1000 cm^{-1}, was observed in all the samples which is ν (Si-N).[23] The literature suggests that the (Si-N-Si) asymmetric stretch is typically centred at around 930 cm^{-1}.

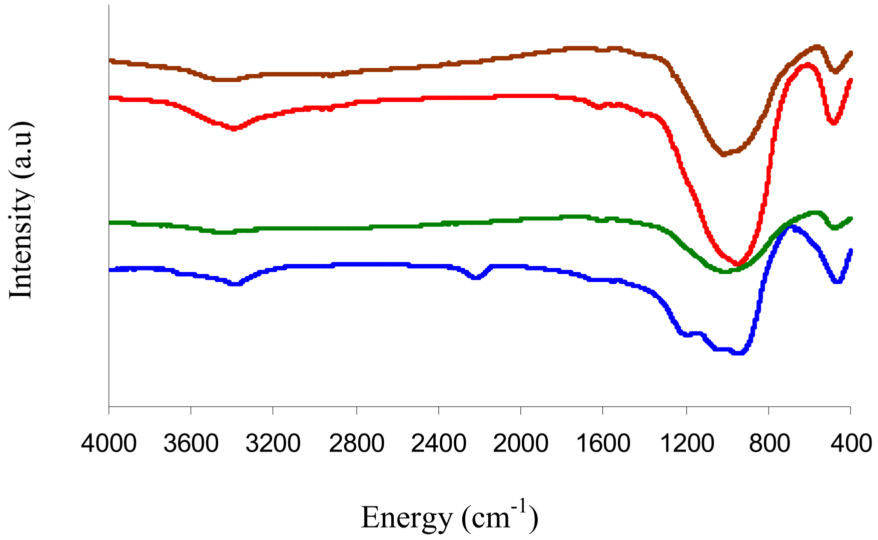

Fig. 6.10 IR spectra for the samples Ta/Si-600 °C (bottom), Ta/Si-1000 °C, Mo/Si-600 °C and Mo/Si-1000 °C (top)

TGA curves were obtained for all the metal-silicon samples heated at different temperatures (Fig. 6.11 and 6.12). In Ta/Si samples obtained at 600 °C no major mass loss was observed below 600 °C when annealing in the TGA, while above this temperature mass loss due to NH$_3$ and N$_2$ did occur. In the Mo/Si system the sample obtained at 600 °C showed mass loss due to amide and a small amount of mass loss was observed at high temperature. No major mass loss was observed at lower temperature in the sample obtained at 1000 °C, while a small amount of mass loss was observed due to NH_3 and N_2 loss from 600 to 800 °C.

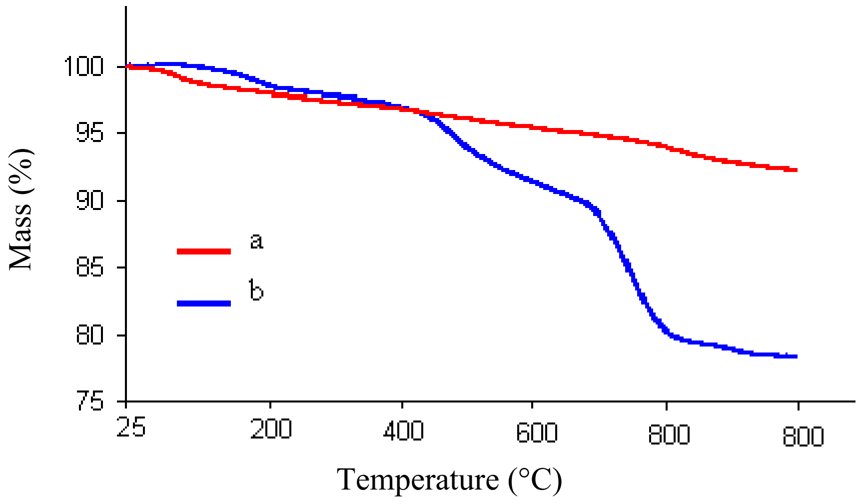

Fig. 6.11 TGA curves obtained for the Ta/SiN_x samples 1000 °C (a) and 600 °C (b)

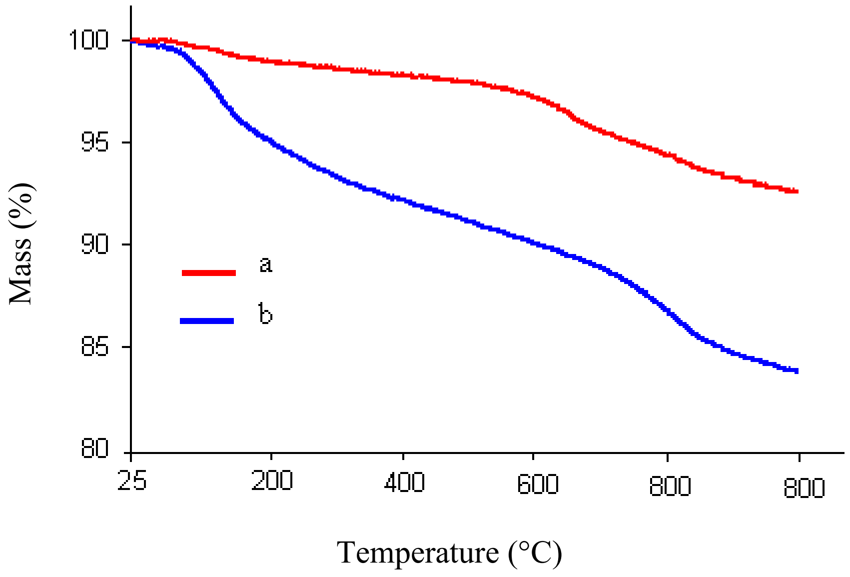

Fig. 6.12 TGA curves obtained for the Mo/SiN_x samples produced at 1000 °C (a), 600 °C (b)

The L_{III}-edge EXAFS data was refined in the same manner as for the amorphous TaN in Chapter 3. No crystalline material was observed in PXD patterns even at 1000 °C. This refinement was carried out using the amplitude reduction factor of 0.72 obtained from the fit for Ta_3N_5 sample (Chapter 3) as the data was collected during the same period of beam time.

The Fourier transformed EXAFS showed two shells at positions consistent with Ta-N and edge linked Ta-N-Ta. The fits shown in Fig. 6.13 use two shells from the Ta_3N_5 structure. The first shell has Ta-N distances consistent with octahedral Ta(V). The coordination number drops in the sample heated at 1000 °C, similarly to that in the binary nitride at 700 °C. The data seem to indicate similar Ta environments to the binary nitride, and hence some clustering of Ta sites, even though this is sufficient for phase segregation and crystallisation.

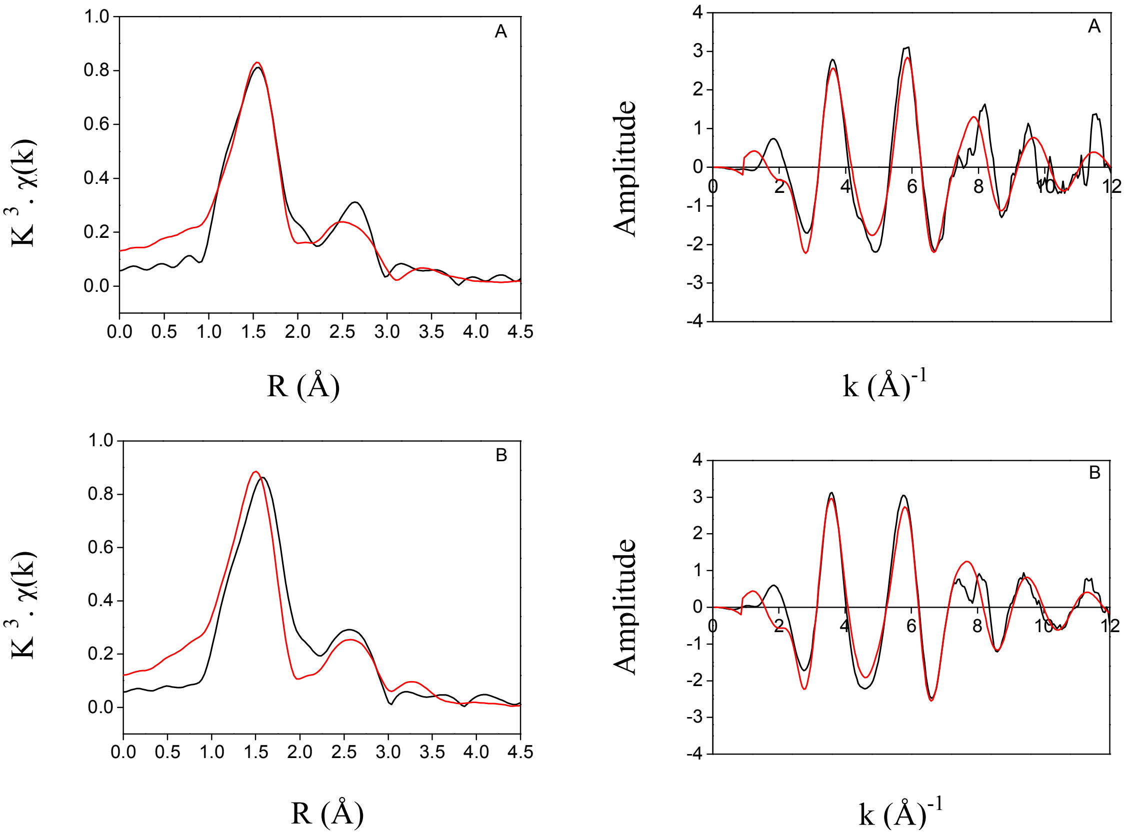

Fig. 6.13 Ta L_{III}-edge EXAFS and Fourier transformed EXAFS spectra of Ta/Si/N_x samples heated in ammonia at Ta/Si/ 1000 °C (A), and Ta/Si/ 600 °C (B)

Table 6.3 Analysis of Ta L_{III}-edge EXAFS of the Ta/Si/N_x using a structure model based one edge-linked TaN_6 units.

Temperature	**600**	**1000**
N Shell		
r/A **Ss/** **N**	2.041(11) 0.0097(17) 5.5(5)	2.017(19) 0.009(2) 2.4(3)
Ta shell		
r/A **ss/A** **N**	3.22(3) 0.0361(8) 6.83(23)	3.23(3) 0.033(8) 11(4)
Red Chi^2	1238	648
R	3.3	4.7
E_0	3.0(9)	3.2(11)

TEM images (Fig. 6.14 and 6.15) of the samples of Mo/SiN_x obtained at 600 °C showed nanotubes of molybdenum nitride supported on silicon nitride. Nanotubes of MoN were also observed after annealing an $Mo(NMe_2)_4$ based precursor at 600 °C under ammonia (Chapter 5). Nanocomposites of the crystallized molybdenum nitride with spherical shape were found with amorphous silicon nitride at 1000 °C. No evidence of phase segregation was observed in Ta/Si matrix.

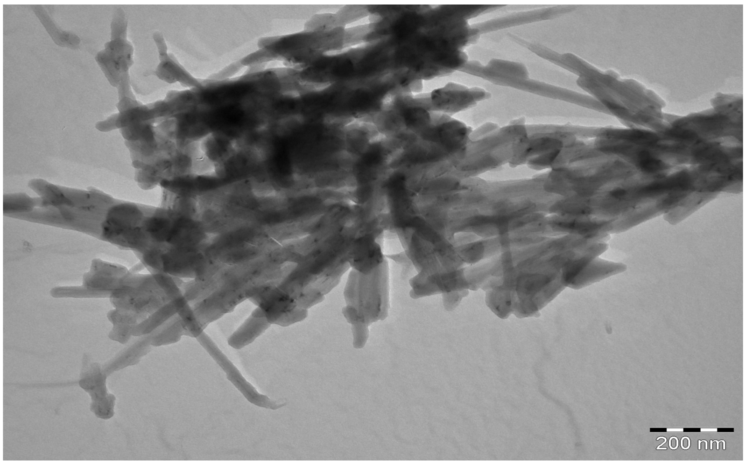

Fig. 6.14 TEM image of an Mo/SiN_x sample heated at 600 °C

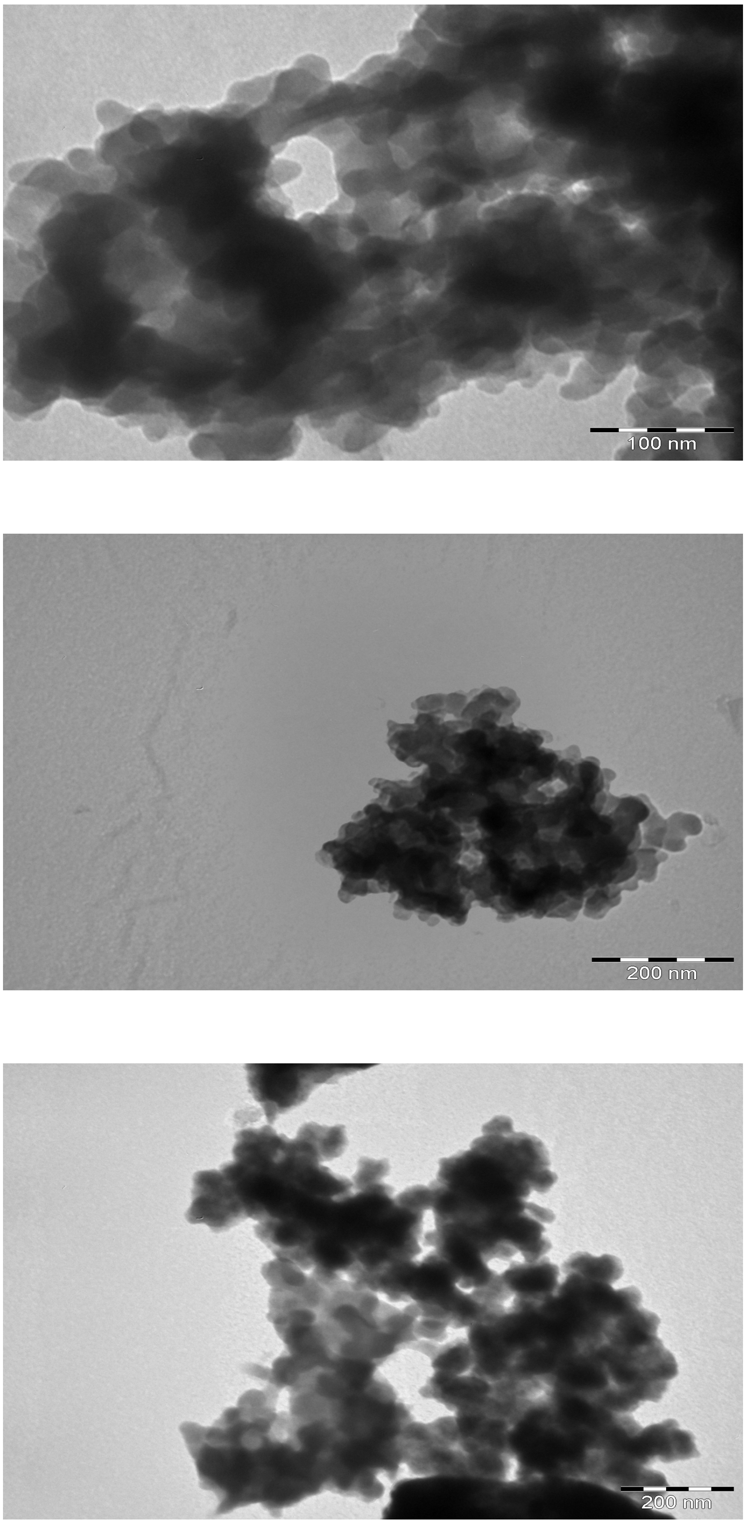

Fig. 6.15 TEM images of the samples Ta/Si 1000 °C (bottom), Ta/Si 600 °C, and Mo/Si 1000 °C (top)

6.5 Conclusions

The synthesis of ternary silicon based nitrides by coammonolysis of metaldialkylamides with a silicon alkylamide, followed by pyrolysis under ammonia was achieved. Heating the dried gels to 600 and 1000 °C produced nanocomposites of molybdenum nitride particles or nanotubes supported on a silicon nitride amorphous matrix. Tantalum/silicon nitride leads to an amorphous phase with Ta in the silicon nitride matrix, though some clustering is evidenced by a Ta…Ta peak in the EXAFS. The difference in behaviour, phase segregation with Mo incorporation into the matrix with Ta can probably be attributed to the higher reactivity of $Mo(NMe_2)_4$ compared with that of $Ta(NMe_2)_4$.

6.6 References

1. C. J. Brinker and G. W. Scherer, *Sol-Gel Science*, 1990, Academic Press, New York
2. Z. Jiang and W. E. Rhine, *Chem. Mater.*, 1994, **6**, 1080.
3. J. Löffelholz, J. Engering and M. Jansen, *Z. Anorg. Allg. Chem.*, 2000, **626**, 963.
4. J. Engering and M. Jansen, *Z. Anorg. Allg. Chem.*, 2003, **629**, 913.
5. R. Rovai, C. W. Lehman and J. S. Bradley, *Angew. Chem. Intl. Ed.*, 1999, **38**, 2036.
6. F. Cheng, S. J. Archibald, S. Clark, B. Toury, S. M. Kelly and J. S. Bradley, *Chem. Mater.*, 2003, **15**, 4651.
7. C. Balan, K. W. Volger, E. Kroke and R. Riedel, *Macromolecules*, 2000, **33**, 3404.
8. B. Mazumder and A. L. Hector, *Top. Catal.*, 2009, **52**, 1472.
9. A. L. Hector, *Chem. Soc. Rev.*, 2007, **36**, 1745.
10. F. Cheng, S. M. Kelly, N. A. Young, S. Clark, M. G. Francesconi, F. Lefebvre and J. S. Bradley, *Chem. Commun.*, 2005, 5662.
11. D. Farruseng, K. Schlichte, B. Zibrowius, J. S. Bradley and F. Schuth, *Angew. Chem. Int. Ed.*, 2001, **40**, 4204.
12. J. Loffelholz, J. Engering and M. Jansen, *Z. Anorg. Allg. Chem.*, 2000, **626**, 963.
13. D. C. Bradley, *Coord. Chem. Rev.* , 1967, **2**, 299.
14. D. C. Bradley, R. C. Mehrotra and D. P. Gaur, *Metal Alkoxides,* , Academic Press London, 1978.
15. G. M. Brown and L. Maya, *J. Amer. Ceram. Soc.*, 1998, **71**, 78.
16. M. H. Chisholm, D. V. Baxter, G. J. Gama, V. F. Distasi, A. L. Hector and I. P. Parkin, *Chem. Mater.*, 1996, **8**, 1222.
17. M. Karl, G. Seybert, W. Massa and K. Dehnicke, *Z. Anorg. Allg. Chem.*, 1999, **625**, 375.
18. K. J. Wynne and R. W. Rice, *Ann. Rev. Mater. Sci*, 1984, **14**, 297.
19. H. Andersch and M. Jansen, *Acta Cryst.*, 1990, **C46**, 1985.
20. N. P. C. Westwood and J. E. Drake, *Chem. Soc.*, 1971, **(A)22**, 3617.
21. F. Cheng, S. Clark, S. M. Kelly and J. S. Bradley, *J. Amer. Ceram. Soc*, 2004, **87**, 1413.

22. K. Nakamoto, *Infrared and Raman Spectra of Inorganic and Organic Compounds* 3rd ed.; J. Wiley: New York, 1978.

23. A. L. Smith, *Spectrochim. Acta,*, 1960, **16**, 87.

7. Conclusions

Reactions of chlorides or amides with ammonia offer an interesting way to control synthesis of metal nitride powders and potentially to target high surface area compositions or new particle morphologies. Ammonolysis of a chloride or dialkylamide group results in an amide moiety that can act as a nucleophile toward another metal centre yielding a bridging imide group. A polymeric product containing amide, imide and unreacted chloride or dialkylamide groups results, the balance between these varying with the reaction conditions. The resultant amide/imide powders or gels can then be heated to produce nitrides with loss of ammonia.[1] These reactions have been explored only superficially to date.

Sol-gel processes are useful in materials synthesis. They are relatively low in cost and often are low temperature processing routes, and are simple to follow with the ability to tailor parameters such as particle size or pore size by changing the reaction conditions.[2] Morphologies such as films, fibres, dense monoliths, mesoporous structures and nanostructured materials can be produced with large or small surface areas and homogeneous dispersion of dopant elements.[3]

In Chapter 3 solution phase ammonolysis of $Ta(NMe_2)_5$ was used to prepare a polymeric amide precursor to tantalum nitrides. $Ta(NMe_2)_5$ was dissolved in THF and ammonia was condensed into the solution at -78 °C. Heating the polymeric precursor in ammonia resulted in amorphous samples of TaN at 500, 600 and 700 °C, and crystalline Ta_3N_5 at 800 °C. TGA studies showed that the amorphous TaN obtained at 700 °C and below is transformed to Ta_3N_5 with some cubic TaN when re-annealed at 800 °C under nitrogen. Ta_3N_5 initially obtained at 800 °C was found to be stable even after re-annealing at 800 °C for 1 hr under nitrogen. All the Ta_3N_5 samples obtained had lattice parameters that were consistent with reported values,[4] though with a slight variation in the b axis length. TEM images showed nanocrystalline samples, with agglomerated particles due to high temperature annealing. Even TaN_x compositions with some carbon content are of interest, e.g. as hard materials or catalysts, since carbon incorporation into TMNs often increases the hardness of the material and carbides often have similar catalytic functions to those of nitrides.[1,5]

In Chapter 4, $MoCl_5$ was reacted with ammonia at -78 °C to produce a chloroamide precursor, and this was annealed at various temperatures under flowing NH_3.

Hexagonal MoN_x samples were obtained after heating at 500 °C for 12, 24 and 48 hrs, while amorphous MoN_x was obtained after 2 hrs annealing of the polymeric precursor. PXD patterns showed the crystallinity of the product increased when annealed at lower temperature for longer time periods. Phase pure cubic MoN was obtained at 700-1000 °C after 2 hrs annealing. A mixture of cubic and hexagonal MoN phases was obtained after heating at 600 °C under nitrogen for 2 hrs. Some molybdenum impurity was observed in the samples obtained at 900 and 1000 °C due to reduction of the metal at high temperature. Chlorine was observed in the samples obtained at 500 °C for shorter time periods, while no contamination due to carbon was found in any of the samples. TEM images showed the nanocrystalline material, while SEM suggests the material has high porosity.

In Chapter 5, $Mo(NMe_2)_4$ was prepared following three different literature procedures[6-8]. We could only recover the desired product via one of these methods[7]. $Mo(NMe_2)_4$ was then reacted with NH_3 to prepare a polymeric precursor. On further annealing the precursor at 600 °C under ammonia, nanotubes of phase pure hexagonal δ-MoN_x were obtained. Heating at 1000 °C produced the hexagonal δ-MoN mixed with cubic MoN_x phase. Synthesis of molybdenum nitride from the amide precursor resulted in the formation of large numbers of nanotubes. This was not observed when the chloride was used.

In Chapter 6, the synthesis of silicon nitride ceramics containing tantalum or molybdenum through controlled coammonolysis of two different alkylamides was investigated.[9-12] $Ta(NMe_2)_5$ or $Mo(NMe_2)_4$ was mixed with $Si(NMe)_4$ in THF and NH_3 was condensed over the solution at -78 °C, followed by pyrolysis under ammonia. Heating the dried gels to 600 or 1000 °C produced nanocomposites of molybdenum nitride particles supported on a silicon nitride amorphous matrix. In the tantalum/silicon reactions, an amorphous phase was obtained with Ta in the silicon nitride matrix, though some clustering is evidenced by a Ta…Ta peak in the EXAFS. The phase segregation with Mo but not with Ta is probably due to the higher reactivity of the $Mo(NMe_2)_4$ precursor. After firing at 600 °C, molybdenum nitride nanotubes were also observed in the molybdenum/silicon nitride nanocomposite.

7.1 References

1. B. Mazumder and A. L. Hector, *Top. Catal.*, 2009, **52**, 1472.
2. A. L. Hector, *Chem. Soc. Rev*, 2007, **36**, 1745.
3. B. Mazumder and A. L. Hector, *J. Mater. Chem*, 2009, **19**, 4673.
4. B. Fu and L. Gao, *J. Amer. Ceram. Soc.*, 2005, **88**, 3519.
5. H. J. Holleck, *Vac. Sci. Technol.*, 1986, **A 4**, 1384.
6. D. S. Kuiper, P. T. Wolczanski, E. B. Lobkovsky and T. R. Cundari, *Inorg. Chem.*, 2008, **47**, 10542.
7. M. Chisholm, F. A. Cotton, B. A. Frenz, W. W. Reichert, L. W. Shive and B. R. Stults, *J. Am. Chem. Soc.*, 1976, **98**, 4469.
8. D. C. Bradley and M. H. Chisholm, *J. Chem. Soc*, 1971, 2741.
9. M. Karl, G. Seybert, W. Massa and K. Dehnicke, *Z. Anorg. Allg. Chem.*, 1999, **625**, 375.
10. G. M. Brown and L. Maya, *J. Amer. Ceram. Soc.*, 1998, **71**, 78.
11. M. H. Chisholm, D. V. Baxter, G. J. Gama, V. F. Distasi, A. L. Hector and I. P. Parkin, *Chem. Mater.*, 1996, **8**, 1222.
12. K. J. Wynne and R. W. Rice, *Ann. Rev. Mater. Sci*, 1984, **14**, 297.

7. Conclusions

Reactions of chlorides or amides with ammonia offer an interesting way to control synthesis of metal nitride powders and potentially to target high surface area compositions or new particle morphologies. Ammonolysis of a chloride or dialkylamide group results in an amide moiety that can act as a nucleophile toward another metal centre yielding a bridging imide group. A polymeric product containing amide, imide and unreacted chloride or dialkylamide groups results, the balance between these varying with the reaction conditions. The resultant amide/imide powders or gels can then be heated to produce nitrides with loss of ammonia.[1] These reactions have been explored only superficially to date.

Sol-gel processes are useful in materials synthesis. They are relatively low in cost and often are low temperature processing routes, and are simple to follow with the ability to tailor parameters such as particle size or pore size by changing the reaction conditions.[2] Morphologies such as films, fibres, dense monoliths, mesoporous structures and nanostructured materials can be produced with large or small surface areas and homogeneous dispersion of dopant elements.[3]

In Chapter 3 solution phase ammonolysis of $Ta(NMe_2)_5$ was used to prepare a polymeric amide precursor to tantalum nitrides. $Ta(NMe_2)_5$ was dissolved in THF and ammonia was condensed into the solution at -78 °C. Heating the polymeric precursor in ammonia resulted in amorphous samples of TaN at 500, 600 and 700 °C, and crystalline Ta_3N_5 at 800 °C. TGA studies showed that the amorphous TaN obtained at 700 °C and below is transformed to Ta_3N_5 with some cubic TaN when re-annealed at 800 °C under nitrogen. Ta_3N_5 initially obtained at 800 °C was found to be stable even after re-annealing at 800 °C for 1 hr under nitrogen. All the Ta_3N_5 samples obtained had lattice parameters that were consistent with reported values,[4] though with a slight variation in the b axis length. TEM images showed nanocrystalline samples, with agglomerated particles due to high temperature annealing. Even TaN_x compositions with some carbon content are of interest, e.g. as hard materials or catalysts, since carbon incorporation into TMNs often increases the hardness of the material and carbides often have similar catalytic functions to those of nitrides.[1,5]

In Chapter 4, $MoCl_5$ was reacted with ammonia at -78 °C to produce a chloroamide precursor, and this was annealed at various temperatures under flowing NH_3.

Hexagonal MoN_x samples were obtained after heating at 500 °C for 12, 24 and 48 hrs, while amorphous MoN_x was obtained after 2 hrs annealing of the polymeric precursor. PXD patterns showed the crystallinity of the product increased when annealed at lower temperature for longer time periods. Phase pure cubic MoN was obtained at 700-1000 °C after 2 hrs annealing. A mixture of cubic and hexagonal MoN phases was obtained after heating at 600 °C under nitrogen for 2 hrs. Some molybdenum impurity was observed in the samples obtained at 900 and 1000 °C due to reduction of the metal at high temperature. Chlorine was observed in the samples obtained at 500 °C for shorter time periods, while no contamination due to carbon was found in any of the samples. TEM images showed the nanocrystalline material, while SEM suggests the material has high porosity.

In Chapter 5, $Mo(NMe_2)_4$ was prepared following three different literature procedures[6-8]. We could only recover the desired product via one of these methods[7]. $Mo(NMe_2)_4$ was then reacted with NH_3 to prepare a polymeric precursor. On further annealing the precursor at 600 °C under ammonia, nanotubes of phase pure hexagonal δ-MoN_x were obtained. Heating at 1000 °C produced the hexagonal δ-MoN mixed with cubic MoN_x phase. Synthesis of molybdenum nitride from the amide precursor resulted in the formation of large numbers of nanotubes. This was not observed when the chloride was used.

In Chapter 6, the synthesis of silicon nitride ceramics containing tantalum or molybdenum through controlled coammonolysis of two different alkylamides was investigated.[9-12] $Ta(NMe_2)_5$ or $Mo(NMe_2)_4$ was mixed with $Si(NMe)_4$ in THF and NH_3 was condensed over the solution at -78 °C, followed by pyrolysis under ammonia. Heating the dried gels to 600 or 1000 °C produced nanocomposites of molybdenum nitride particles supported on a silicon nitride amorphous matrix. In the tantalum/silicon reactions, an amorphous phase was obtained with Ta in the silicon nitride matrix, though some clustering is evidenced by a Ta…Ta peak in the EXAFS. The phase segregation with Mo but not with Ta is probably due to the higher reactivity of the $Mo(NMe_2)_4$ precursor. After firing at 600 °C, molybdenum nitride nanotubes were also observed in the molybdenum/silicon nitride nanocomposite.

7.1 References

1. B. Mazumder and A. L. Hector, *Top. Catal.*, 2009, **52**, 1472.
2. A. L. Hector, *Chem. Soc. Rev*, 2007, **36**, 1745.
3. B. Mazumder and A. L. Hector, *J. Mater. Chem*, 2009, **19**, 4673.
4. B. Fu and L. Gao, *J. Amer. Ceram. Soc.*, 2005, **88**, 3519.
5. H. J. Holleck, *Vac. Sci. Technol.*, 1986, **A 4**, 1384.
6. D. S. Kuiper, P. T. Wolczanski, E. B. Lobkovsky and T. R. Cundari, *Inorg. Chem.*, 2008, **47**, 10542.
7. M. Chisholm, F. A. Cotton, B. A. Frenz, W. W. Reichert, L. W. Shive and B. R. Stults, *J. Am. Chem. Soc.*, 1976, **98**, 4469.
8. D. C. Bradley and M. H. Chisholm, *J. Chem. Soc*, 1971, 2741.
9. M. Karl, G. Seybert, W. Massa and K. Dehnicke, *Z. Anorg. Allg. Chem.*, 1999, **625**, 375.
10. G. M. Brown and L. Maya, *J. Amer. Ceram. Soc.*, 1998, **71**, 78.
11. M. H. Chisholm, D. V. Baxter, G. J. Gama, V. F. Distasi, A. L. Hector and I. P. Parkin, *Chem. Mater.*, 1996, **8**, 1222.
12. K. J. Wynne and R. W. Rice, *Ann. Rev. Mater. Sci*, 1984, **14**, 297.